

Study of Hydrogen Sorption/Desorption Effect on Iron-Based Materials

Influence of Microstructure on the Hydrogen/Metal Interaction

Master Thesis

LAKSHMI SATISH NAIR

August 2022

Delft University of technology



Master Thesis

**Study of Hydrogen
Sorption/Desorption Effect on
Iron-Based Materials**

**Influence of Microstructure on the Hydrogen/Metal
Interaction**

Author: Lakshmi Satish Nair (4809246)

Supervisor: Dr. Y. Gonzalez-Garcia (Department of Materials Science
Committee Members: Dr. A.J. Böttger and Engineering (MSE), 3mE,
Dr. V. Popovich TU Delft)

*A thesis submitted in partial fulfillment of the requirements for
the Master of Science degree in Materials Science and Engineering, TU Delft*

August 2022

ACKNOWLEDGEMENTS

This project was initiated during a discussion with Prof. Yaiza Gonzalez Garcia, who then became the supervisor of my master thesis. I am sincerely and profoundly grateful to Prof. Yaiza, who allowed me to work on this topic. I appreciate her patient guidance and constant motivation during the difficult times of COVID-19. I'm so thankful that she stuck by me through thick and thin. It was a very trying journey, but her continuous support made it much more meaningful.

Additionally, I would like to thank all of the people who were involved in this project at the TU Delft materials science laboratories for their advice and assistance with the experimental setup and materials characterisation. I would like to thank; Agnieszka Kooijman from the Corrosion Technology and Electrochemistry Laboratory for her support and collaboration with the electrochemical experiments, Sander van Asperen and the Microscopy lab assistants for their support with sample preparation, Ruud Hendrikx for performing and providing analysis for the XRD measurements, and Prof. Amarante J. Böttger for providing valuable advice regarding the XRD experiments. I would also like to thank Can Özkan for helping me with the EIS fitting software.

Last but never least, I want to express my love and gratitude to my parents and sister for helping to make this journey possible. I will forever be grateful for their infinite support and advice throughout this process. Without them, I would not be where I am today.

ABSTRACT

Studies on the impact of Hydrogen on the electrochemical and mechanical behaviour of Iron-based materials have been increasingly conducted in the past few years. This is mainly due to the ever-growing demand for sustainable energy sources, which involve Hydrogen and to meet the high structural and economic demands from the automobile sector and other industrial demands for which high-strength steels like dual-phase steels have been developed. Steels may absorb hydrogen both throughout the production process and during different phases of use. High-strength steels (particularly dual phase steels) and martensitic stainless steels are highly susceptible to hydrogen embrittlement. Moreover, hydrogen embrittlement is already possible at quantities as low as 0.1 ppm[1]. Therefore, understanding Metal-hydrogen interactions is essential.

This thesis aims to study the effect of Hydrogen charging on three different iron-based materials and the possible effect on the electrochemical/corrosion performance. The Iron-based materials used in the study are Pure Iron, DP1000 and AISI 420. The methodology involves using an electrochemical procedure based on potentiostatic Hydrogen charging and Cyclic Voltammetry (CV), applied on these Iron-based materials having different phases to monitor H-uptake in the materials. The materials are charged with Hydrogen both on the active and passive surfaces. The electrochemical method is capable of measuring the diffusible H concentration (including mobile Hydrogen) for the steel alloys under H-charging conditions. Using X-Ray Diffraction (XRD) Technique, microstructural analysis is carried out on Pure Iron, DP1000 and AISI 420 stainless steel to identify the different phases interacting with Hydrogen. To gain additional insights relating to the electrochemical/corrosion performance of the investigated materials and into the H-related findings, potentiostatic polarization techniques, Electrochemical Impedance Spectroscopy (EIS) and Scanning Kelvin Probe (SKP) are carried out.

As a result, it was discovered that Pure Iron had the maximum amount of diffusible Hydrogen under the charging conditions tested, followed by DP1000 and then AISI 420 Steel with the lowest amount. EIS technique was useful in identifying a trend between the barrier properties of the passive layer and the H desorption values for the three materials. The results also revealed that materials charged with Hydrogen on active and passive surfaces behaved differently with respect to the amount of Hydrogen desorption. The microstructural features of the active surface and the passive oxide film that formed on the materials are further discussed in relation to this.

CONTENTS

1	INTRODUCTION	1
1.1	Research Approach and Thesis Focus	2
2	BACKGROUND AND LITERATURE	3
2.1	Materials of Interest	3
2.1.1	Phase Transformation of Steel	3
2.1.2	Different Types of Steel Microstructures	4
2.1.3	Alloy Properties	6
2.1.4	Stainless Steels	7
2.1.5	Advanced High Strength Steels	8
2.2	Basics of Corrosion and Corrosion Prevention	9
2.3	Passivation	11
2.3.1	Properties of the Passive Layer on Iron-based Alloys	12
2.3.2	Passive Layer Breakdown	15
2.4	Hydrogen in Steels	16
2.4.1	Hydrogen entry and evolution	16
2.4.2	Hydrogen Solubility - Iron and Steels	19
2.4.3	Hydrogen Diffusion and Trapping - Iron and Steels	20
2.4.4	Hydrogen and the Passive Oxide Layer on Steels	24
2.4.5	Impact of Hydrogen absorption on the properties of Iron-based alloys	25
2.5	Techniques to study Hydrogen/Material Interaction	26
2.5.1	Methods to Charge Hydrogen	26
2.5.2	Methods to Quantify Hydrogen in Steels	28
2.5.3	Cyclic Voltammetry (CV) to study H/material Interaction	28
2.5.4	Electrochemical Impedance Spectroscopy (EIS) to study H/material Interaction	29
2.5.5	Surface mapping of hydrogen	30
2.6	General Discussion of Literature	30
3	MATERIALS AND METHODOLOGY	33
3.1	Material Composition	33
3.2	Electrochemical and Corrosion Experiments	34
3.2.1	Experiment to study H/Material Interaction	34
3.2.2	Experiment to study the impact of Hydrogen charging and discharging on the corrosion properties of the materials	38
3.2.3	Scanning Kelvin Probe (SKP)	39
3.3	Microstructure Characterization	41
3.3.1	X-Ray Diffraction (XRD)	41
4	RESULTS	45
4.1	Microstructure Characterization - XRD	45
4.1.1	Before Hydrogen Charging	45
4.1.2	After Hydrogen Charging and After Hydrogen Discharging	47
4.2	H/material interaction - Electrochemical Experiments	49
4.2.1	Pourbaix Diagram	49
4.2.2	Determination of Operating Parameters	50
4.2.3	OCP Measurements	50
4.2.4	Hydrogen Charging and Discharging Curves	51
4.3	H/material interaction - Electrochemical Experiments - Cyclic Voltammetry	53
4.3.1	Active Behaviour (Pre-conditioning A) - Attribution of Peaks	53
4.3.2	Passive Behaviour (Pre-conditioning B) - Attribution of Peaks	58
4.3.3	Detection of Hydrogen and Data Processing	61

4.4	H/material interaction - Electrochemical Experiments - Electrochemical Impedance Spectroscopy (EIS)	62
4.4.1	Active Behaviour (Pre-conditioning A)	62
4.4.2	Passive Behaviour (Pre-conditioning B)	69
4.5	Electrochemical characterization in NaCl electrolyte	75
4.5.1	DP1000	75
4.5.2	Pure Iron	76
4.5.3	AISI 420	77
4.6	Scanning Kelvin Probe	78
5	DISCUSSION	81
5.1	Active Metal	81
5.2	Passive Oxide	83
5.2.1	H Charging and Discharging	83
5.3	Influence of Hydrogen Charging on the corrosion Properties of the investigated steels	86
6	CONCLUSIONS	87
7	RECOMMENDATIONS AND OUTLOOK	89
A	APPENDIX	101

LIST OF FIGURES

Figure 2.1	The Fe-C equilibrium diagram up to 6.67 wt.% C. Solid lines represent Fe-Fe ₃ C equilibrium; dashed lines represent Fe-graphite equilibrium; A ₁ - the upper limit of the ferrite-cementite phase field, A ₃ - The boundary between the austenite and austenite-ferrite fields, A _{cm} - boundary of the austenite and austenite-cementite phase field[2].	3
Figure 2.2	Austenite microstructure of the tested steel processed by recrystallization controlled rolling and ultra fast cooling [3]. . .	5
Figure 2.3	Microstructure of pearlite, a lamellar mixture of ferrite and cementite[4].	5
Figure 2.4	Main scenarios of phase transformations in steel[5].	6
Figure 2.5	Scanning Electron Microscopy (SEM) image showing a typical microstructure of a Dual Phase (DP) steel. The darker, smooth areas are ferrite. The light-colored, embossed islands are martensite[6].	7
Figure 2.6	Rust, the Result of Corrosion of Metallic Iron. Iron is oxidized to Fe ²⁺ (aq) at an anodic site on the surface of the iron, which is often an impurity or a lattice defect. Oxygen is reduced to water at a different site on the surface of the iron, which acts as the cathode. Electrons are transferred from the anode to the cathode through the electrically conductive metal. Water is a solvent for the Fe ²⁺ that is produced initially and acts as a salt bridge. Rust (Fe ₂ O ₃ · xH ₂ O) is formed by the subsequent oxidation of Fe ²⁺ by atmospheric oxygen [7].	9
Figure 2.7	Schematic representation of the corrosion mechanism for steel [8].	10
Figure 2.8	The release of electrons by the more active zinc layer causes the iron to be cathodic[9].	10
Figure 2.9	Anodic polarization and overvoltage curve for iron in 1 N H ₂ SO ₄ , [10].	11
Figure 2.10	Pourbaix diagram and anodic overvoltage curves for iron in water[10].	12
Figure 2.11	Equilibrium phase diagram for the iron-oxygen system. α, ferrite; γ, austenite[11].	13
Figure 2.12	Mott-Schottky plots of steels after film formation at the film formation potential(E_f) = 0.9 V (SHE) for 3600 s[12].	15
Figure 2.13	Schematic of passive film on dual-phase steel[12]. The thickness is in the order of nanometers.	15
Figure 2.14	Diagram of the potential energy vs. distance curves for the various Hydrogen states at the metal-gas interface; the two adsorption states (weakly bonded, on-top, sites and strongly bonded, chemisorbed, sites), the sub-surface state (H_{ss}) and the bulk dissolved (absorbed) state H_{diss} . [13]	17

Figure 2.15	Solid solubility data of hydrogen in stainless steels and the data was obtained through electrochemical permeation experiments [14]. The hydrogen solubility in grades of Austenitic Stainless Steels (ASS), such as AISI 304, 302, 321 and 347, seems to be in the range of $25 - 90 \text{ mol/m}^3 \cdot \text{MPa}^{0.5}$. The Hydrogen solubility in 13Cr and 16Cr, which are martensitic stainless steels, seems to be in the range of 3 to $60 \text{ mol/m}^3 \cdot \text{MPa}^{0.5}$. In alpha ferrite, the hydrogen solubility seems to be in the range of 1 to $10 \text{ mol/m}^3 \cdot \text{MPa}^{0.5}$. These solubility ranges are taken with respect to different temperature ranges.	20
Figure 2.16	Hydrogen diffusion coefficients in austenitic stainless steels[14].	21
Figure 2.17	Representation of hydrogen at interstitial lattice site and trapped location at (a) atomic scale and (b) microscopic scale[15]. . . .	22
Figure 2.18	Various location where hydrogen atoms are presented in microstructure are (a) solid solution; (b) solute hydrogen pair; (c) dislocation atmosphere; (d) grain boundary accumulation; (e) particle-matrix interface accumulation; (f) void containing recombined hydrogen[16].	23
Figure 2.19	H trapping sites and their corresponding trapping activation energies for iron and steels[17].	23
Figure 2.20	Oxide diffusion coefficients for various materials[18].	25
Figure 2.21	(I): Applied potential as a function of time for a generic cyclic voltammetry experiment, with the initial, switching, and end potentials represented (A, D, and G, respectively)[19].	29
Figure 2.22	Representative SKP potential maps of hydrogen charged surface of ferritic steel after 1, 5 and 10 h as well as uncharged surface with equipotential areas marked for contact potential difference (CPD) values of - 0.2, - 0.1 and 0.0 V (SHE)[20]. . . .	30
Figure 3.1	Right: A schematic of the cold-mounted sample, Left: Picture of the actual sample. The blue circle on the pictures is just an indication of where the exposed area is on the material. . . .	34
Figure 3.2	Right: A schematic of the three-electrode cell, Left: Picture of the actual set-up used in this experiment, the sample is bottom mounted and clamped between the two bottom plates with a circular area of 0.316 sq.cm diameter being exposed to the electrolyte.	35
Figure 3.3	When there is no electrical connection between the probe and the sample, each has a unique Fermi level E_{xp} and work function W_{xp} . Since the probe and sample are electrically linked during an SKP measurement (b), charge flows from the sample to the probe (c). As a result, a surface charge known as the contact potential difference V_{cp} is created between the probe and sample. In SKP, a backup potential V_b is provided between the probe and the sample (e) to null the surface charge and restore the Fermi levels to their initial positions. This potential is equal to the contact potential difference but has the opposite sign.[21]	40
Figure 3.4	A schematic of the SKP sample and the area of interest. . . .	41
Figure 4.1	X-Ray Diffraction peaks of Pure Iron Before Hydrogen charging (Peak fitting with the red lines - α -Fe).	45
Figure 4.2	X-Ray Diffraction peaks of DP1000 Before Hydrogen charging (Peak fitting with the red lines - α -Fe and Peak fitting with the blue lines - γ -Fe.	46
Figure 4.3	X-Ray Diffraction peaks of AISI 420 Before Hydrogen charging (Peak fitting with the red lines - α -Fe (BCT martensite). . . .	46

Figure 4.4	X-Ray Diffraction peaks of Pure Iron After Hydrogen (dis)charging (Peak fitting with the red lines - α -Fe (BCC Ferrite), Peak fitting with the blue lines - Feroxyhyte (FeO(OH))).	47
Figure 4.5	X-Ray Diffraction peaks of DP1000 After Hydrogen (dis)charging (Peak fitting with the red lines - α -Fe (BCC Ferrite/ BCT Martensite), Peak fitting with the blue lines - Feroxyhyte (FeO(OH), Peak fitting with the green lines - γ -Fe).	48
Figure 4.6	Pourbaix diagram of iron. The red rectangle marks the pH range of the electrolyte used in this study and the lower dashed orange line represent the stability region of water. The filled regions in the diagram indicate a solid phase whereas empty regions indicate dissolution of Fe ions.	49
Figure 4.7	Pourbaix diagram of Fe 87% Cr 13% system. The lower dashed orange line represent the stability region of water. The filled regions in the diagram indicate a solid phase whereas empty regions indicate dissolution of Fe and Cr ions.	50
Figure 4.8	OCP values for DP1000, Pure Iron and AISI 420 in 1 M NaOH + 8 g/L Thiourea	51
Figure 4.9	CA curve for H charging at a constant potential of -1.25 V vs SSCsat for DP1000 in 1 M NaOH + 8 g/L Thiourea	52
Figure 4.10	CA curve for H discharging at a constant potential of -0.90 V vs SSCsat for DP1000 in 1 M NaOH + 8 g/L Thiourea	52
Figure 4.11	Overview of the procedure for cyclic voltammetry, DP1000 (a) three CV scans before hydrogen charging, (b) six CV scans after 1 hour of hydrogen charging and (c) six CV scans after 30 mins of hydrogen discharging in 1 M NaOH solution containing 8 g/l thiourea solution (scan rate 10 mV/s).	53
Figure 4.12	Comparison of a1 peaks after hydrogen charging for DP1000 in 1 M NaOH solution and 1 M NaOH solution containing 8 g/l thiourea (scan rate 10 mV/s).	55
Figure 4.13	Overview of the procedure for cyclic voltammetry, Pure Iron (a) three CV scans before hydrogen charging, (b) six CV scans after 1 hour of hydrogen charging and (c) six CV scans after 30 mins of hydrogen discharging in 1 M NaOH solution containing 8 g/l thiourea solution (scan rate 10 mV/s).	56
Figure 4.14	Overview of the procedure for cyclic voltammetry, AISI 420 (a) three CV scans before hydrogen charging, (b) six CV scans after 1 hour of hydrogen charging and (c) six CV scans after 30 mins of hydrogen discharging in 1 M NaOH solution containing 8 g/l thiourea solution (scan rate 10 mV/s).	57
Figure 4.15	Comparison of the peak a1' for two CV curves after H charging for 1 hour and 3 hours, AISI 420 in 1 M NaOH solution containing 8 g/l thiourea solution (scan rate 10 mV/s).	58
Figure 4.16	Overview of the procedure for cyclic voltammetry, DP1000, Pre-conditioning B (a) three CV scans before hydrogen charging, (b) six CV scans after 1 hour of hydrogen charging and (c) six CV scans after 30 mins of hydrogen discharging in 1 M NaOH solution containing 8 g/l thiourea solution (scan rate 10 mV/s).	59
Figure 4.17	Overview of the procedure for cyclic voltammetry, Pure Iron, Pre-conditioning B (a) three CV scans before hydrogen charging, (b) six CV scans after 1 hour of hydrogen charging and (c) six CV scans after 30 mins of hydrogen discharging in 1 M NaOH solution containing 8 g/l thiourea solution (scan rate 10 mV/s).	60

Figure 4.18	Overview of the procedure for cyclic voltammetry, AISI 420, Pre-conditioning B (a) three CV scans before hydrogen charging, (b) six CV scans after 1 hour of hydrogen charging and (c) six CV scans after 30 mins of hydrogen discharging in 1 M NaOH solution containing 8 g/l thiourea solution (scan rate 10 mV/s).	60
Figure 4.19	A comparison of the hydrogen-related, after H charging, CV peak a1' for DP1000, Pure Iron and AISI 420 in both Active Behaviour (Pre-conditioning A) and Passive Behaviour (Pre-conditioning B).	61
Figure 4.20	A comparison of the surface charge density under the a1' peak for DP1000, Pure Iron and AISI 420 in both Active Behaviour (Pre-conditioning A) and Passive Behaviour (Pre-conditioning B).	62
Figure 4.21	(a) Bode plots of DP1000: Before H Charging, After H Discharging and After H Discharging in 1 M NaOH solution containing 8 g/l thiourea solution; (b)Nyquist plots of DP1000: Before H Charging, After H Discharging and After H Discharging in 1 M NaOH solution containing 8 g/l thiourea solution - Pre-conditioning A.	63
Figure 4.22	Equivalent circuit proposed for modelling the electrochemical response of DP1000 in 1 M NaOH solution containing 8 g/l thiourea solution - Pre-conditioning A[22].	64
Figure 4.23	Equivalent circuits considered for modelling the electrochemical response of DP1000 in 1 M NaOH solution containing 8 g/l thiourea solution - Pre-conditioning A[22].	64
Figure 4.24	(a) Bode plots of Pure Iron: Before H Charging, After H Discharging and After H Discharging in 1 M NaOH solution containing 8 g/l thiourea solution; (b)Nyquist plots of Pure Iron: Before H Charging, After H Discharging and After H Discharging in 1 M NaOH solution containing 8 g/l thiourea solution - Pre-conditioning A.	65
Figure 4.25	(a) Bode plots of AISI 420: Before H Charging, After H Discharging and After H Discharging in 1 M NaOH solution containing 8 g/l thiourea solution; (b)Nyquist plots of AISI 420: Before H Charging, After H Discharging and After H Discharging in 1 M NaOH solution containing 8 g/l thiourea solution - Pre-conditioning A.	66
Figure 4.26	(a) Bode plots of DP1000: Before H Charging, After H Discharging and After H Discharging in 1 M NaOH solution containing 8 g/l thiourea solution; (b)Nyquist plots of DP1000: Before H Charging, After H Discharging and After H Discharging in 1 M NaOH solution containing 8 g/l thiourea solution - Pre-conditioning B.	69
Figure 4.27	(a) Bode plots of Pure Iron: Before H Charging, After H Discharging and After H Discharging in 1 M NaOH solution containing 8 g/l thiourea solution; (b)Nyquist plots of Pure Iron: Before H Charging, After H Discharging and After H Discharging in 1 M NaOH solution containing 8 g/l thiourea solution - Pre-conditioning B.	71
Figure 4.28	(a) Bode plots of AISI 420: Before H Charging, After H Discharging and After H Discharging in 1 M NaOH solution containing 8 g/l thiourea solution; (b)Nyquist plots of AISI 420: Before H Charging, After H Discharging and After H Discharging in 1 M NaOH solution containing 8 g/l thiourea solution - Pre-conditioning B.	72

Figure 4.29	Potentiodynamic polarisation plots for DP1000 in 3.5 wt% NaCl before charging with H and after charging and discharging with H.	75
Figure 4.30	Potentiodynamic polarisation plots for Pure Iron in 3.5 wt% NaCl before charging with H and after charging and discharging with H.	76
Figure 4.31	Potentiodynamic polarisation plots for AISI 420 in 3.5 wt% NaCl before charging with H and after charging and discharging with H.	77
Figure 4.32	Map of Vcpd distribution on the surface of (a)DP1000, (b)Pure Iron and (c) AISI 420 sampleS that was locally charged with hydrogen, measured by SKP microscopy	78
Figure 4.33	Line scan of Vcpd distribution on the surface of DP1000, Pure Iron (PI) and AISI 420 samples Before H Charging (BC) and After H Charging (AC), measured by SKP microscopy.	79
Figure 5.1	Comparison of charge density(C/cm2) vs time(s) curves obtained after integrating current density vs time curves, for DP1000, Pure Iron and AISI 420 in 1 M NaOH + 8 g/L Thiourea.	81
Figure 5.2	Schematic representation of the oxide layer formation on the metal surface during HER, adapted from [23]. The light blue color corresponds to the electrolyte.	84

LIST OF TABLES

Table 2.1	Phase - Temperature relation from the phase diagram[24] (Figure 2.1)	4
Table 2.2	Effect of alloying elements on DP steels [25]	7
Table 2.3	Table on the cathodic hydrogen charging parameters from literature	27
Table 3.1	Chemical composition (wt%) of the pure iron samples.	33
Table 3.2	Chemical composition (wt%) of the DP1000 samples.	33
Table 3.3	Chemical composition (wt%) of the AISI 420 samples.	33
Table 3.4	Experimental Procedure for Pre-conditioning A	37
Table 3.5	Experimental Procedure for H Charging and Discharging on on the Passive Surface	38
Table 3.6	Experimental Procedure for part 1 - electrochemical characterization in NaCl electrolyte before Hydrogen charging . . .	39
Table 3.7	Experimental Procedure for part 2 - electrochemical characterization in NaCl electrolyte after Hydrogen charging and discharging	39
Table 3.8	Electrochemical sample preparation for SKP - After Hydrogen Charging	40
Table 3.9	SKP Parameters	41
Table 3.10	XRD Instrument specifications and parameters	42
Table 3.11	Electrochemical sample preparation for XRD - After Hydrogen Charging	43
Table 3.12	Electrochemical sample preparation for XRD - After Hydrogen Discharging	43
Table 4.1	The table shows the possibly present crystalline phases in the materials before H charging, using the ICDD pdf4 database. The color sticks mentioned correspond to the colored fitting lines in the XRDs.	47
Table 4.2	The table shows the possibly present crystalline phases after H charging and H discharging, using the ICDD pdf4 database.	48
Table 4.3	OCP values of the three materials under study in the 1 M NaOH + 8 g/L Thiourea electrolyte. The OCP measurement has been performed at least four times and the averages with the error are shown.	51
Table 4.4	Equivalent circuit parameters obtained by fitting the collected EIS data of DP1000, Pure Iron and AISI 420 samples in Active Behaviour (Pre-conditioning A). Parameters are the averaged values and standard deviation resulting from three measurement repetitions. The Chi Sqr. value is obtained from the ZView fitting software.	68
Table 4.5	Equivalent circuit parameters obtained by fitting the collected EIS data of DP1000, Pure Iron and AISI 420 samples in Passive Behaviour (Pre-conditioning B). Parameters are the averaged values and standard deviation resulting from three measurement repetitions. The Chi Sqr. value is obtained from the ZView fitting software.	74
Table 4.6	Potentiodynamic polarisation table for DP1000 in 3.5 wt% NaCl before charging with H and after charging and discharging with H	75

Table 4.7	Potentiodynamic polarisation table for Pure Iron in 3.5 wt% NaCl before charging with H and after charging and discharging with H	76
Table 4.8	Potentiodynamic polarisation table for AISI 420 in 3.5 wt% NaCl before charging with H and after charging and discharging with H	77
Table A.1	Peak potentials of the CV voltammograms for DP1000 - Pre-Conditioning A, the peaks a3 and c2 are not included in the table as it is beyond the scope of this study. Eo' is the formal standard potential and it equals half of the total sum of potentials of a redox couple.	101
Table A.2	Peak potentials of the CV voltammograms for Pure Iron - Pre-Conditioning A. Eo' is the formal standard potential and it equals half of the total sum of potentials of a redox couple.	101
Table A.3	Peak potentials of the CV voltammograms for AISI 420. Eo' is the formal standard potential and it equals half of the total sum of potentials of a redox couple.	101
Table A.4	Peak potentials of the CV voltammograms for DP1000 - Pre-conditioning B. Eo' is the formal standard potential and it equals half of the total sum of potentials of a redox couple.	102
Table A.5	Peak potentials of the CV voltammograms for Pure Iron - Pre-conditioning B. Eo' is the formal standard potential and it equals half of the total sum of potentials of a redox couple.	102
Table A.6	Peak potentials of the CV voltammograms for AISI 420 - Pre-conditioning B. Eo' is the formal standard potential and it equals half of the total sum of potentials of a redox couple.	102

ACRONYMS

HE	Hydrogen Embrittlement	1
DP	Dual Phase	ix
MSS	Martensitic Stainless Steels	2
CI	Cast Iron	3
CS	Carbon Steel	3
MP	Melting Point	4
SEM	Scanning Electron Microscopy	ix
BCC	Body-Centred Cubic	4
FCC	Face-Centred Cubic	4
BCT	Body-Centred Tetragonal	6
SAE	Substitutional Alloying Elements	6
IAE	Interstitial Alloying Elements	6
TS	Tensile Strength	8
AHSS	Advanced High Strength Steels	8
HSS	High Strength Steels	2
SS	Stainless steels	7
ASS	Austenitic Stainless Steels	x
FSS	Ferritic Stainless Steels	7
DSS	Duplex Stainless Steels	7
PHSS	Precipitation Hardening Stainless Steels	7
TRIP	Transformation Induced Plasticity	8
TDA	Thermal Desorption Analysis	28
SIMS	Secondary Ion Mass Spectrometry	28
SKP	Scanning Kelvin Probe	30
SKPFM	Scanning Kelvin Probe Force Microscopy	30
NRA	Nuclear Reaction Analysis	30
ESD	Electron Stimulated Desorption	30
TWIP	Twinning-induced plasticity	23
XRD	X-Ray Diffraction	2
EIS	Electrochemical Impedance Spectroscopy	33
OCP	Open Circuit Potential	33
CV	Cyclic Voltammetry	33

1

INTRODUCTION

The end of the nineteenth century saw emerging interest in research on the relationship between hydrogen and the mechanical properties of Iron-based alloys[26]. It was found that hydrogen had a damaging effect on the mechanical properties of many metallic materials such as the alloys of iron (Fe), nickel (Ni)[27, 28] and aluminium (Al)[29] among others[30]. For instance, the decrease in fracture toughness and breaking strain in certain iron-based alloys after immersion in hydrochloric (HCl) and sulphuric acids (H_2SO_4) was first reported by Johnson[26]. Since then, the subject has been widely researched and discussed, and all phenomena related to hydrogen-induced mechanical degradation and its detrimental effects have fallen under the umbrella of Hydrogen Embrittlement (HE). In addition to microstructural characteristics, the hydrogen diffusivity and the hydrogen absorption capacity play a significant role in how susceptible a metal is to hydrogen embrittlement. Although HE phenomena has been extensively studied, the complexity of the phenomena makes sure that its underlying mechanisms are still reviewed, and new theories are suggested and discussed.

Hydrogen is the lightest element in the periodic table and at low temperatures (-50 °C to 100 °C) can diffuse very strongly into steels through coatings, pore layers and cracks on its surface [31]. The form of H_2 that can bring about degradation in metals is usually present in the environment. Hydrogen can be physisorbed on the surface of the metal as H_2 molecules (thermal charging) and then undergo direct dissociation to atoms. Or in the absence of an active site, the H_2 molecules can undergo surface diffusion and then disassociation [32]. Surface absorption of hydrogen as H_3O^+ ions (electrochemical charging by proton or water reduction) is also possible and will follow a similar dissociation mechanism as in the case of the H_2 molecule [13]. Most of the diffused hydrogen then gets trapped in the interstitial sites of the regular lattice. Grain boundaries, phase boundaries, dislocations, vacancies, solute atoms and interfaces between particles or inclusions and the metal matrix are just some of the many microstructural trap sites for hydrogen[32]. The solubility of hydrogen in steel is largely dependent on its chemical composition, structure and temperature.

Hydrogen may interact with iron-based alloys in a variety of applications. Still, one that is attracting a lot of attention has to do with the energy industry. The international energy market is undergoing a massive transformation from the more conventional energy sources: coal, petroleum fuel, and natural gas, to more environmentally - friendly energy sources. One such environmentally-friendly energy route is the conversion of water to hydrogen and oxygen by electrolysis. The hydrogen generated can then function as an energy storage medium where the energy stored can be later converted to electricity through the use of a fuel cell or by some other means. Another area where a hydrogen related sustainable technology is replacing a traditionally unsustainable process is the recent plan from Tata Steel, IJmuiden to pursue the hydrogen route with respect to steel production. For this plan to be effectively adopted it is very important to fully understand the effect that hydrogen can have on every facet of the production process. Hydrogen likely will be an essential pillar in the clean-energy foundation and therefore, ensuring the safe and cost-effective storage and transportation of H_2 is of utmost importance. In the oil and gas industry, HE mainly occurs due to the exposure of steel to gaseous or liquid hydrogen sulphide (H_2S). Hydrogen embrittlement can also occur due to the cathodic reaction of hydrogen evolution; in a corrosion cell, during an electro-

plating process, during acid cleaning, during surface treatments like (degreasing, pickling, tumbling) and in cathodic protection systems[33, 31].

The interaction of H₂ with metals, in particular with Iron-based alloys such as High Strength Steels (HSS) and Martensitic Stainless Steels (MSS), is of key interest in this study. Steels may absorb hydrogen both throughout the production process and during different phases of use. High-strength steels (particularly dual phase steels) and martensitic stainless steels are highly susceptible to hydrogen embrittlement[34, 35, 36, 37]. Dual phase steels and martensitic stainless steels are exposed to heat treatments during the manufacturing process, and such heat treated steel microstructures can have several potential hydrogen trap sites. Certain dual phase (DP) steel alloys, for example, are composed of ferrite and martensite phases, where hydrogen can possibly be trapped at phase boundaries in addition to grain boundaries, dislocations, and lattice vacancies[38]. Several approaches (electrochemical permeation, hot extraction, etc.) can be utilized to gain quantitative information on the diffusible hydrogen in steel.

1.1 Research Approach and Thesis Focus

The present study aims to compare three Iron-based materials - Pure iron, dual-phase steel and martensitic stainless steel – containing different microstructural features and chemical compositions to evaluate the H/material-interaction and also understand the effect that this interaction has on the corrosion properties of the material. The main research questions for this thesis are therefore as follows:

- How does the H/material-interaction compare for pure iron, dual-phase steel and martensitic stainless steel based on their chemical composition and microstructural features?
- How is the passive oxide layer formed on pure iron, dual-phase steel and martensitic stainless steel affected by the H/material-interaction?
- What is the aftermath that the H/material-interaction has on the corrosion properties of pure iron, dual-phase steel and martensitic stainless steel?

These questions will be answered using a combination of different experiments, both to research the microstructure and corrosion properties. For this purpose, microstructural characterization using X-Ray Diffraction (XRD) and electrochemical analyses have been performed.

This thesis is divided into six main chapters.

- Chapter 2 provides an insight into steel microstructure, the corrosion behaviour of iron-based materials, the interaction of hydrogen with iron-based materials, and finally introduces the various methods to qualitatively and quantitatively analyse hydrogen/material-interaction.
- Chapter 3 will discuss the different materials and experimental methods used in the study.
- Chapter 4 will present the results obtained from the experimental methods.
- Chapter 5 will discuss the results and analyse what they mean with respect to the research questions.
- Chapter 6 and 7 will present the conclusions and recommendations for future research related to this study.

2

BACKGROUND AND LITERATURE

2.1 Materials of Interest

2.1.1 Phase Transformation of Steel

Ferrous alloys have significant technological importance due to their tremendous versatility of use and their abundance in the earth's crust (4.2%). Steel is primarily an alloy of iron, small amounts of carbon and other elements the quantities which, when fine-tuned based on chemical composition can generate a multitude of materials, all different types of steels, that can cater to various applications. Heat treatment of steel can produce a wide range of microstructures and properties. The iron-carbon phase diagram is the basis for all the studies on the heat treatment of steel(Figure 2.1).

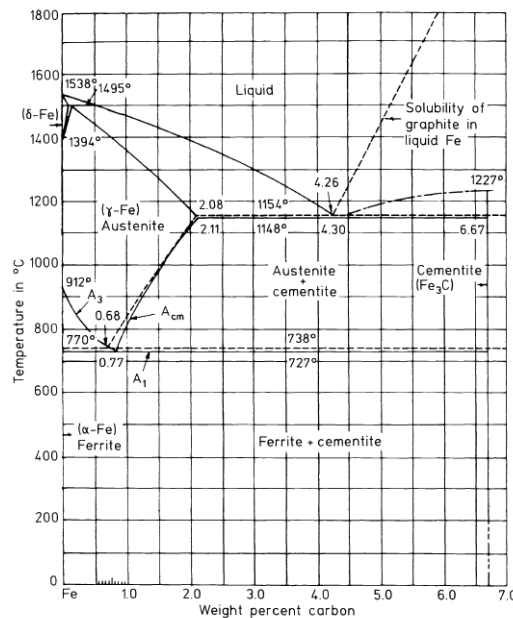


Figure 2.1: The Fe-C equilibrium diagram up to 6.67 wt.% C. Solid lines represent Fe-Fe₃C equilibrium; dashed lines represent Fe-graphite equilibrium; A₁ - the upper limit of the ferrite-cementite phase field, A₃ - The boundary between the austenite and austenite-ferrite fields, A_{cm} - boundary of the austenite and austenite-cementite phase field[2].

The Fe-C phase diagram shows the stable temperature-composition regions of different phases of steel and the equilibrium boundaries between the phases. The X-axis of the Fe-C phase diagram goes from 0 wt% up to 6.67 wt% of carbon, and the Y-axis is a temperature scale. At percentages of carbon less than 0.008%, the metal is assumed to be pure iron. The phase diagram assumes that the system has attained equilibrium. However, the effect of alloying elements is not observed in the diagram. Therefore the diagram mostly functions as a guide. Iron alloys that contain less than 2.14wt% of carbon are known as Carbon Steel (CS), and alloys that have more than 2.14wt% of carbon are known as cast irons Cast Iron (CI)[2]. Depending on the temperature and at atmospheric pressure, Iron (Fe) which is an allotropic

element, can have more than one stable crystal form. The table Table 2.1 shows the stable temperature ranges for the different phases. When the solid solubility of carbon in ferrite or austenite, exceeds the limit a new phase called cementite or iron carbide (Fe_3C) is formed. In figure Figure 2.1, along the lines A_1 , A_3 and A_{cm} , the temperature change is arrested, and phase change occurs. The temperature remains constant until the phase change is completed (thermal arrest). The effect of alloying elements on the properties and behaviour of steel will be looked into later.

Table 2.1: Phase - Temperature relation from the phase diagram[24] (Figure 2.1)

Stable alloy phase	Temperature range (°C)
Alpha Iron (ferrite)*	0 - 912
Gamma Iron (austenite)*	912 - 1394
Delta iron (delta ferrite)*	1394 - 1538 (Melting Point (MP) of pure iron)
δ -ferrite + Liquid = γ -iron (austenite), peritectic reaction ^a	1495
Liquid = Fe_3C + γ -iron, eutectic reaction ^a	1148
γ -iron = α ferrite + Fe_3C , eutectoid reaction ^a	727

* - They constitute the pure iron end of the Fe-C phase diagram
a - Invariant three-phase equilibria, Fe_3C is the stable high carbon phase

2.1.2 Different Types of Steel Microstructures

Steel microstructures are complex and diverse. Mainly influenced by various factors such as the section size, composition, homogeneity and processing, steels can generate a multitude of microstructures. To illustrate the microstructures that will be discussed, SEM and optical microscopy images are shown in Figure 2.2, Figure 2.3 and Figure 2.4.

2.1.2.1 α - Iron and Ferrite

Alpha iron is a Body-Centred Cubic (BCC) form of iron that is stable in the temperature range mentioned in table Table 2.1 while ferrite is a solid solution in BCC iron. At room temperature, ferrite is stable in pure iron until 912°C, after which the Face-Centred Cubic (FCC) austenite phase is stable. Still, then it reverts to ferrite (high-temperature ferrite, also known as delta ferrite) at 1394°C. Atomic volume expansion of approximately 1-3% accompanies the change from austenite to alpha ferrite[39]. It is essential to understand their geometry since that provides an understanding of the solubility of non-metallic elements such as carbon, nitrogen and hydrogen. The solubility of carbon in ferrite that is in equilibrium with cementite is very low for low temperatures[39]. The maximum solubility of carbon in ferrite is about 0.02 wt.% carbon at 727 °C[24]. The morphology of ferrite can change drastically based on the cooling rate and chemical composition.

2.1.2.2 Austenite or γ - Iron

Austenite is a FCC form of iron that is stable in the temperature range mentioned in table Table 2.1. It is possible to retain austenite to room temperature by the addition of alloying elements like Ni and Mn. Carbon has a much higher solubility in austenite, which is stable in higher temperatures, compared to ferrite, which is stable at lower temperatures[24]. At 1148°C, austenite can dissolve up to 2.11% of carbon. The cooling down of austenite to the ferrite phase comes with the associated reject of carbon by diffusion.

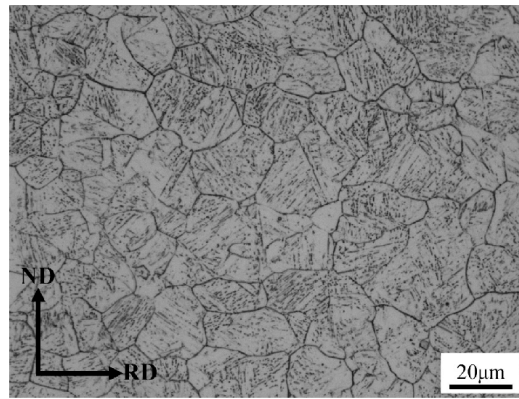


Figure 2.2: Austenite microstructure of the tested steel processed by recrystallization controlled rolling and ultra fast cooling [3].

2.1.2.3 Cementite

Cementite, also known as iron carbide (Fe_3C), is a metastable phase and has an orthorhombic crystal structure. The equilibrium state of cementite is graphite. There are plenty of carbide phases present in steels; among them, cementite is the phase that is most commonly found. Cementite is formed as a new carbide phase to accommodate the substitutional alloying elements, including carbon that gets rejected when the solid solubility of the ferrite or austenite phase is exceeded[40, 41].

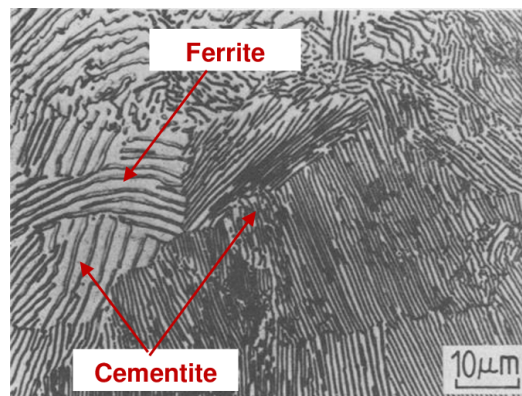


Figure 2.3: Microstructure of pearlite, a lamellar mixture of ferrite and cementite[4].

2.1.2.4 Pearlite

Pearlite is a mixture of ferrite and cementite that is formed below a temperature range of 1150°C to 723°C and due to the eutectoid decomposition of austenite upon slow cooling. The diffusion of carbon atoms during the cooling lets the ferrite and cementite grow contiguously. The transformation of austenite to pearlite usually takes place in the grain boundaries of austenite as they are regions of high energy and have a greater atomic disorder than inside the grain. The carbon precipitates as Fe_3C between ferrite laths, and forms parallel laths of Fe and Fe_3C . This unique lamellar morphology is usually noticed in pearlite[4].

2.1.2.5 Bainite

Bainite, like pearlite, has a two-phase microstructure that usually includes ferrite and cementite. It is formed by the cooling transformation of austenite with a cooling rate higher than that of pearlite but lower than that of martensite. There are two

forms of bainite, upper bainite and lower bainite. Bainite has one of the most complex solid-state phase transformations to understand because of its formation in a temperature range that is neither so high that the atoms are very mobile nor so low that the atoms cannot diffuse quickly. In this intermediate range, it may or may not be possible for the carbon to diffuse. Upper bainite forms at temperatures between 550°C and 400°C and lower bainite forms at temperatures between 400°C and 250°C[42]. Unlike pearlite, bainite has a non-lamellar carbide distribution and grain structure that is finer. Nucleation during transformation starts due to partial shear.

2.1.2.6 Martensite

Martensite is a Body-Centred Tetragonal (BCT) form of iron that is formed due to the rapid cooling of the austenite phase. It is a tough and brittle phase mainly due to the microstructure being supersaturated with interstitial carbon. There is no diffusion carbon but a sudden diffusionless shear process that occurs during martensite formation. Based on the composition of steel, a temperature range can be set to define the martensite start and finish temperatures (M_s and M_f)[42].

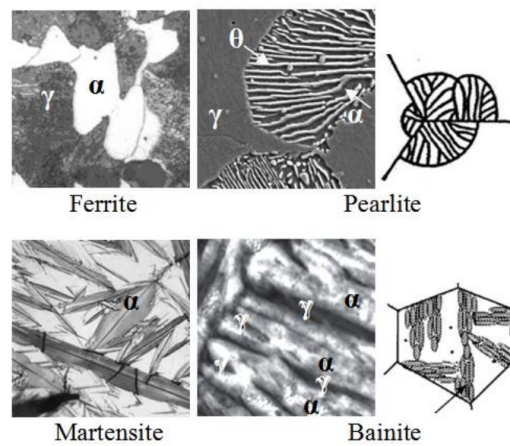


Figure 2.4: Main scenarios of phase transformations in steel[5].

2.1.3 Alloy Properties

The choice of alloying elements in stainless steel is crucial for its properties. In multicomponent steels, the starting structures are the basic allotropes of iron. Some alloying elements may replace the iron atoms in the FCC or BCC structures due to their similarity in size and electronic structure. These elements are called Substitutional Alloying Elements (SAE) as they form substitutional solid solutions with iron. Ni and Mn (stabilize the FCC iron), Cr and Mo (stabilize the BCC iron) are examples of SAE. Interstitial Alloying Elements (IAE) as the name suggests are elements that are substantially smaller in size than the iron atoms and therefore take positions in the interstices between the Fe atoms. Carbon and nitrogen are examples of IAE. Hydrogen, the smallest atom that can be found in steel can diffuse large distances instantaneously even at room temperature. The capability of the iron allotropes to dissolve the IAE is one of the main reasons for the variety of steel microstructures. Alloying elements such as Cr, Mo, Ti, V, and Nb are added to steel to improve their mechanical properties since they are strong carbide forming elements[24]. Alloying elements can also be divided based on their effect on the equilibrium diagram. They can be γ -stabilizers that expand the γ -field by encouraging the formation of

the austenite phase or be α -stabilizers that contract the γ -field and encourage the formation of ferrite over a wider compositional limit.

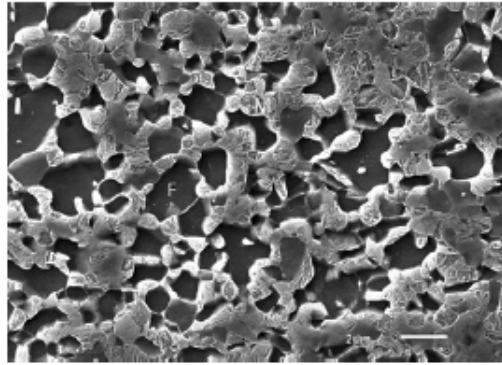


Figure 2.5: SEM image showing a typical microstructure of a DP steel. The darker, smooth areas are ferrite. The light-colored, embossed islands are martensite[6].

Table 2.2: Effect of alloying elements on DP steels [25]

Alloying element	Effect on the material
C	Strengthens the martensite Stabilize the austenite
Mn	Solid solution strengthening in ferrite Stabilize the austenite
Cr	Retards pearlite or bainite formation
Mo	Retards pearlite or bainite formation
Si	Promotes ferrite formation
V	Precipitation strengthening and microstructure refinement
Nb	Precipitation strengthening and microstructure refinement

2.1.4 Stainless Steels

Stainless steels (SS) is a type of ferrous alloy that distinguishes itself from other ferrous alloys due its corrosion resistant properties. The corrosion resistance of SS is mainly in part due to the presence of Cr, in quantities ranging from 10.5% to 30%, and other alloying elements such as Ni[43]. The presence of an appreciable amount of Cr in SS leads to the instantaneous formation of chromium oxide, on the surface of the steel, which acts as a protective layer. There are five major varieties of SS on the basis of their crystal structure: ASS, Ferritic Stainless Steels (FSS), MSS, Duplex Stainless Steels (DSS) and Precipitation Hardening Stainless Steels (PHSS).

2.1.4.1 Austenitic Stainless Steel (ASS)

ASS is the most commonly used type of SS with a primarily austenitic crystal structure. These iron based alloys have greater corrosion resistance than FSS and MSS, and exceptional mechanical properties over a wide range of temperatures. Most grades of ASS are paramagnetic in nature. Ni, Mn and N can be used as austenite phase stabilizers, Cr is used to improve corrosion resistance and Mo can be used to generate resistance against pitting corrosion.

2.1.4.2 Ferritic Stainless Steel (FSS)

FSS is a type of SS with a primarily Ferritic (BCC) crystal structure. It differentiates itself from other SS by the presence of higher quantities of Cr. FSS also has very low or no Ni in it, which is also the case for MSS. FSS IS not hardenable by heat treatment and is magnetic. They also have carbon percentages below 0.2%[\[44\]](#).

2.1.4.3 Martensite Stainless Steel (MSS)

Martensitic grades have high strength, wear resistance, fair corrosion resistance and are magnetic. Their compositions are close to the composition of ferritic stainless steels. Addition of nickel, copper and molybdenum to the steel improves its toughness and corrosion resistance. Light water reactors (LWRs) and other industries use martensitic stainless steels (MSSs) such as Type 403, 410, and 420 as components of pumps, valve seats, stem rods, nuts, and bolts[\[34\]](#).

2.1.4.4 Duplex Stainless Steel (DSS)

DSS are iron based alloys with two crystal phases, an austenite phase and a ferrite phase. Their design focuses on providing greater corrosion resistance and higher strength compared to most standard grades of ASS. With respect to its composition, DSS has higher quantities of Cr (20 - 28%) and Mo, and lower amounts of Ni with respect to ASS[\[45\]](#).

2.1.4.5 Precipitation Hardening Stainless Steel (PHSS)

PHSS are steels such as martensitic, austenitic or semi-austenitic steel that can be precipitation hardened to yield a material that has exceptionally high strength and has a corrosion resistance equivalent to that of ASS. Alloying elements such as aluminum, copper and niobium can be added to increase the strength of the alloy.

2.1.5 Advanced High Strength Steels

Advanced High Strength Steels (AHSS) are multiphase steels which have a minimum tensile strength of at least 440 MPa[\[46\]](#). They are lightweight and have high tensile strength. The impressive formability of AHSS is what makes it appealing to the automobile industry. AHSS usually has a ferrite phase in combination with another constituent or phase such as martensite, bainite, austenite or retained austenite. Depending on the phase combinations present, steels with unique properties can be designed. Dual Phase steel is a highly popular type of AHSS that is used predominantly in the automobile industry. Transformation Induced Plasticity (TRIP) steel is another example of an AHSS and they have multiple crystal phases such as ferrite, martensite, bainite, austenite and/or retained austenite.

2.1.5.1 Dual-Phase Steel (DP Steel)

DP steels are high strength automotive sheet steels that have a mixed microstructure that is formed as a result of its chemical composition and the application of mechanical and thermal treatment. DP steels have high strain hardening, High uniform elongation and low yield strength to tensile strength ratio. Tensile Strength (TS) of DP steels usually range from 450 to 1200 MPa[\[47\]](#). With respect to its microstructure, when low or medium carbon steels are cold rolled followed by continuous annealing and quenching from a temperature between the A₁ - A₃ range, they result in the formation of a ductile ferrite matrix that is interspersed with high strength "hard" martensite islands[\[47\]](#). Figure 2.5 shows a typical microstructure of DP steel. While the ductile ferrite phase offers good formability, the martensite phase offers

substantial strengthening. DP steels are generally prone to hydrogen embrittlement due to the presence of high carbon martensite (Carbon percentage in martensite, C_M 0.6%)[47]. The effect of alloying elements on DP steels can be seen in table Table 2.2.

2.2 Basics of Corrosion and Corrosion Prevention

Corrosion is defined as ‘an irreversible interfacial reaction of a material (metal, ceramic, polymer) with its environment which results in consumption of the material or in dissolution into the material of a component of the environment[48].’ The deterioration of the metal to its more stable form (such as its oxide, hydroxide or sulphide state) is a result of corrosion. Corrosion processes occur on the surface, and the type and rate of corrosion are hugely dependent on the metal and the environmental conditions around the metal. It is essential to understand the chemical and physical conditions of the interface between the metal and the surrounding environment. The chemical composition, microstructure and stress of the bulk-solid phase of the metal are important parameters that define the corrosion process and influence the electrochemical properties of the metal. The electrolytic medium and its properties are also essential in understanding corrosion phenomena.

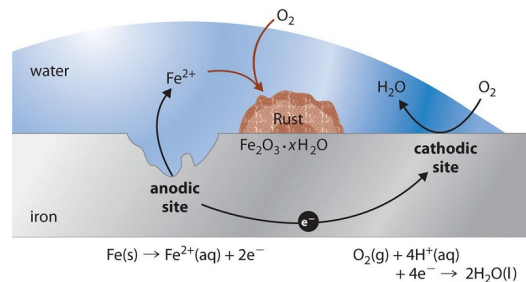


Figure 2.6: Rust, the Result of Corrosion of Metallic Iron. Iron is oxidized to $\text{Fe}^{2+}(\text{aq})$ at an anodic site on the surface of the iron, which is often an impurity or a lattice defect. Oxygen is reduced to water at a different site on the surface of the iron, which acts as the cathode. Electrons are transferred from the anode to the cathode through the electrically conductive metal. Water is a solvent for the Fe^{2+} that is produced initially and acts as a salt bridge. Rust ($\text{Fe}_2\text{O}_3 \cdot x\text{H}_2\text{O}$) is formed by the subsequent oxidation of Fe^{2+} by atmospheric oxygen [7].

For instance, in the electrochemical process of corrosion of steel in an aerated neutral/alkaline solution which can be thought to occur in stages, the anodic site releases ferrous ions into the solution first. The electrons from the oxidation of the anode travel through the metal to the adjacent cathodic site in the material where reduction to hydroxyl takes place (see Figure 2.7). In the case of an acidic medium or an aerated acidic medium, H_2 gas or H_2O is generated. Steels and iron are used in various applications both structurally and otherwise; making sure that these engineering systems do not fail due to corrosion is critical. Many researchers have investigated the influence of microstructure on the corrosion behaviour of different steels. The primary reaction involved in steel corrosion is the conversion of steel to its oxide form in the presence of oxygen and moisture (see Figure 2.6). Due to the presence alloying elements in steel such as Cr, at certain environmental conditions, a passive oxide layer forms on the surface of the steel. This passive film is both chemically and physically stable and acts as a protective layer. Studying the passive film properties of steels leads to a better understanding of its corrosion resistance and mechanical behaviour.

There are a couple of ways to combat the corrosion of steels. One way to prevent the corrosion of steel is by using the method of cathodic protection. Cathodic pro-

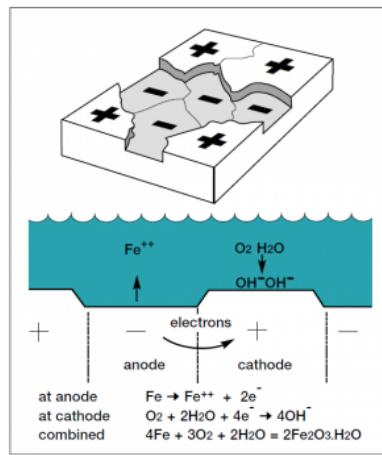


Figure 2.7: Schematic representation of the corrosion mechanism for steel [8].

tection prevents corrosion by shifting the electrode potential to a lower value so that the surface to be protected is negatively polarised. The anodic (active) sites on the metal surface get converted to cathodic (passive) sites by providing free electrons from an external source. One way this can be achieved is by using sacrificial anodes, which is a less noble metal than the metal to be protected. Galvanized steel is an example of a sacrificial anode, where steel is dipped into a bath of molten zinc. The zinc undergoes the anodic reaction instead of the steel, thereby protecting it (see figure 2.8).

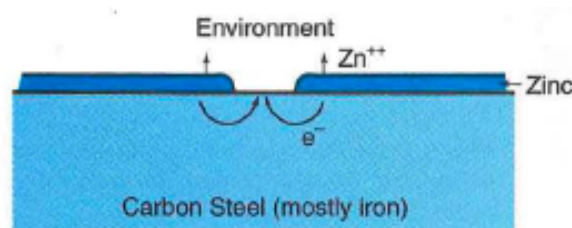


Figure 2.8: The release of electrons by the more active zinc layer causes the iron to be cathodic[9].

Anodic protection is another method, by which the rate of corrosion can be significantly reduced. This method involves shifting the electrode potential to a higher value so that the surface protected is positively polarized. Anodic protection converts the active state of the metal to the passive state. Passivation happens when there is a sudden reduction in the corrosion resistance of an active metal due to positive polarization of the metal surface, which thereby increases the oxidizing power of the environment. In the case of stainless steels, the presence of Cr leads to the formation of a thin film of chromium oxide on the steel surface when exposed to oxygen. Passivity can be best explained using polarization curves. Starting from the corrosion potential (E_{corr}), if the potential is increased until the passivation potential (E_{pass}), a critical current density (i_{cr}) is reached. A substantial reduction in the current density follows this, which is caused by passivation.

In the passive region, the current density remains more or less constant. Increasing the potential further, a point is reached, beyond a certain value called E_b , where the current density increases again, indicating movement into the transpassive region (see figure 2.9). The sharp increase in current can be due to the breakdown of the passive layer or the onset of another reaction[49]. E_b can be called the breakdown potential when it corresponds to the breakdown potential.

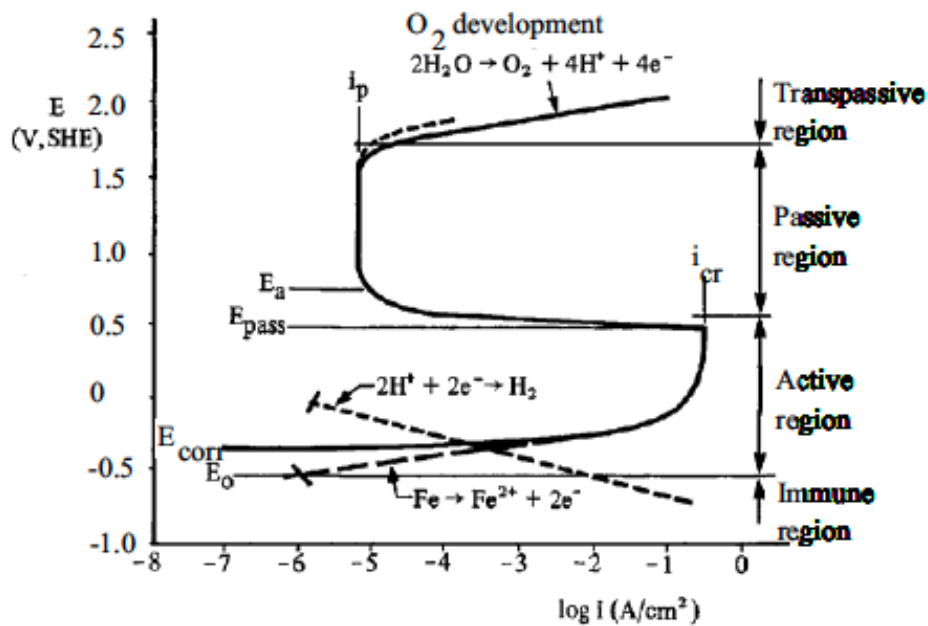


Figure 2.9: Anodic polarization and overvoltage curve for iron in 1 N H_2SO_4 [10].

The presence of dispersed chromium in the crystal lattice of stainless steel makes the steel resistant, to a large extent, to corrosion degradation. Chromium, by passivation, can rapidly form a thin oxide layer (Cr_2O_3) on the surface of the metal. This oxide layer prevents the further oxidation of the original metal layer underneath the chromium oxide layer. The Cr_2O_3 layer formed is and must be highly stable, well bonded to the metal, thin, and free of pores and other defects. Another way of preventing or reducing the effects of corrosion is by using corrosion inhibitors. Corrosion inhibitors are substances that can be added to the metal environment in small amounts to reduce, slow down or prevent the corrosion of the metal. Corrosion inhibitors can be anodic, cathodic, or mixed. The use of paint coatings and chemical conversion coatings on metal is also a suitable method of corrosion prevention, but it is out of the scope of this work.

2.3 Passivation

Passivity is primarily the loss of chemical reactivity experienced by metals when in certain environmental conditions. There are two competing theories for the cause of passivity in metals. One is the oxide film theory, which assumes that passivity is due to the formation of an oxide layer on the metal's surface. The other theory is that passivation is a process in which oxygen is adsorbed onto the metal surface. Since oxide films can be formed via stages of oxygen adsorption, the two theories do not conflict too much. To prevent the anodic dissolution of the metal, the oxide layer has to have low ionic conductivity and low solubility[10]. These characteristics of the passivating oxide layer will prevent considerably the transportation of the metal ions in the crystal lattice of the metal to the liquid environment. But the slow dissolution through the oxide layer is still possible, and it corresponds to the passive current density (i_p). The i_p is usually much lesser than the current on an active surface at the same potential. Three major kinds of surface oxide layers can be grouped to study the practical effects of corrosion[10].

- Surface films that can impede the anodic dissolution effectively while allowing cathodic reactions (electron transfer) to take place across the external surface

of the film. Fe, Ni, Cr, and their alloys are examples of this type of surface layer formation.

- Surface films that can impede both anodic dissolution and cathodic reactions. Oxide film layers formed on aluminium are an example of such a surface layer.
- The deposition of corrosion products like rust and salts can reduce the anodic and cathodic reaction, but not adequately enough to give effective passivity. The surface layer thus formed will be porous.

In certain pH ranges, when the potential is changed some metals can change from an active state to a passive state. These metals are called active-passive metals and Fe, Ni, Ti, and their alloys are some typical examples. Pourbaix diagrams can be used to understand the passivation behaviour of these metals with respect to pH levels close to the metal surface. In fig. 2.10 a side by side view of the Pourbaix diagram of iron in water with the anodic overvoltage diagrams of the same is shown. The figure shows corresponding regions of immunity, activity and passivity. It can be seen that the passive state illustrated in the overvoltage curve indicates a thermodynamically stable Fe_2O_3 .

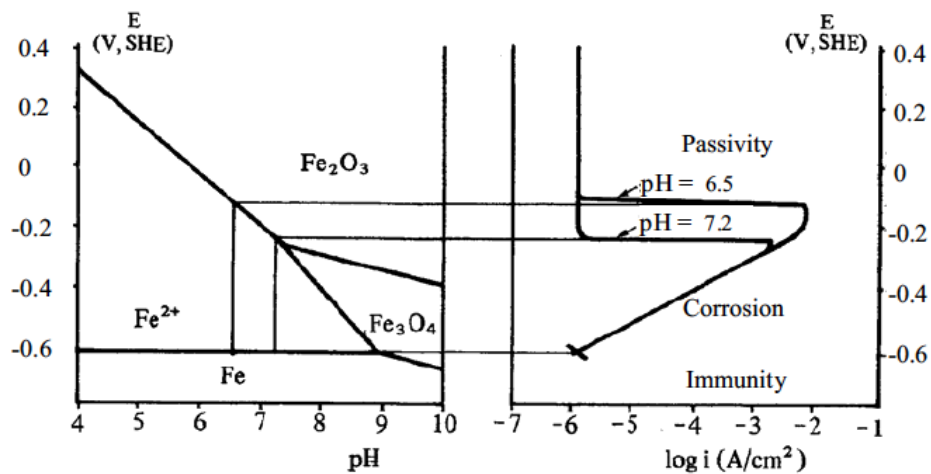


Figure 2.10: Pourbaix diagram and anodic overvoltage curves for iron in water[10].

Passive films on the surface of steels can be either formed naturally or can be artificially induced by immersing the steel in an electrolyte or by applying anodic polarization in the E_{pass} region. Corrosion resistance gained from artificial passivation would be much more superior when compared to corrosion resistance gained from passivating naturally[50]. An alternative for anodization of alloys to gain high quality passive films would be cyclic potentiodynamic anodization (CPA)[51].

The stability of the passive layer is essentially denotes the ability of the passive layer to maintain its state of passivation. It can be characterised by the E_{flade} , E_{pass} , the potential at which passivation ends and the i_p in the passive region. Generally, having a higher E_b means the passive layer is more stable.

2.3.1 Properties of the Passive Layer on Iron-based Alloys

The degree of passivation is determined by the stability, compactness, and continuity of the surface film formed, which in turn is governed by the kinetics of the system. Meanwhile, the stability of the oxide layer formed on steel is dependent on the composition of the alloy and the environment, the passivation temperature and the passivation time. The oxide layer thus formed mainly consists of iron oxide

and if chromium and molybdenum are present, chromium oxide and molybdenum oxide.

To better understand the properties of the passive layer on steels it is important to understand the passive layer formed on pure iron. From the equilibrium Fe-O₂ phase diagram in fig 2.11, it can be predicted that a eutectoid mixture of O₂ and Fe₃O₄ will be formed at standard conditions. The oxide layer thus formed is very thin (20–100 Å) and very difficult to unambiguously characterize. This ambiguity arises due to the thinness of the film and its similarity in electron density to the metal substrate underneath[52].

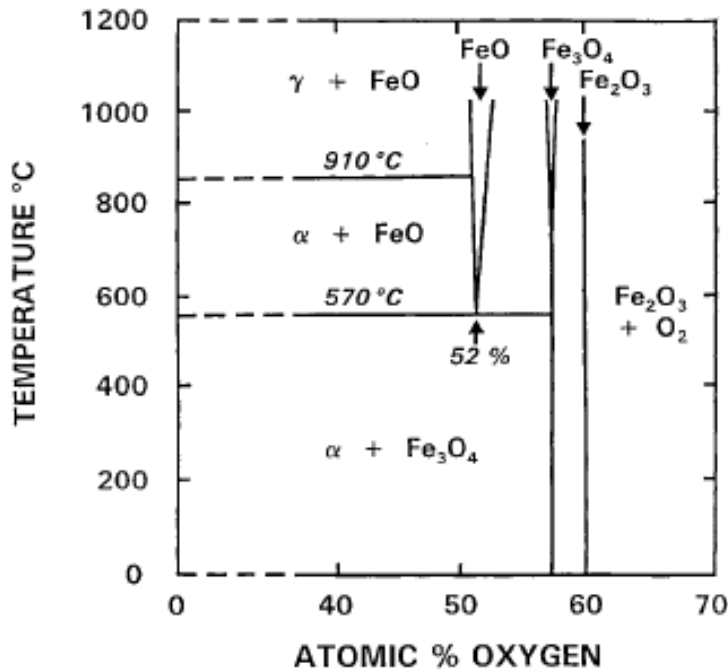


Figure 2.11: Equilibrium phase diagram for the iron-oxygen system. α , ferrite; γ , austenite[11].

Since the formation of the passive film is essentially the result of dynamic equilibrium of the system, the thickness of the film depends on the favorability of the oxidation reaction. If the rate of oxidation is more than the rate of diffusion of metal ions, then the thickness of the film increases and vice versa. In austenitic stainless steels exposed to an acidic environment, increasing the potential of the system toward more positive values can result in increasing the thickness of the passive film. The range of potential when increased from the Flade Potential ("The flade potential is an indication of the change in gibbs free energy of a metal immediately before the final transition step from the passive to the active region[53].") to the potential at the transpassive region, the passive layer showed an increase in thickness from 0.8 to 2.5 nm[54].

Passive layers can be imagined as semiconductors as they show semiconductor like behaviour, which in turn can be used to improve the corrosion resistance of the material. Depending on the dominant imperfections in the passive layer, n-type and p-type semiconductor behaviour can be determined. If there is insufficient metal ions or extra cation vacancies in the passive layer, then the layer is said to show p-type behaviour. Similarly, the presence of extra cations in the interstitial sites or anion vacancies in the passive layer, can be attributed to the passive layer showing n-type behaviour[55]. Mott-Schottky analysis is widely utilized to understand the electronic behaviour of the passive layer by estimating the point defect concentrations in the crystal structure of the passive layer. The Mott-Schottky plot is a representation of the reciprocal square interfacial capacitance as a linear

function of the applied potential. In a study[55] on the semiconductor properties of the passive layers of ferritic stainless steels, it was observed that the inner Cr-rich film showed p-type semiconductor behaviour, while the Fe-rich outer layer showed n-type semiconductor behaviour. This behavior of Fe and Cr can be generalised for most stainless steels.

It is the general idea that the passive layer formed on stainless steels is a bilayer structure comprised of an inner iron-chromium-rich oxide and a precipitated outer hydroxide layer. Stainless steels rich in Cr usually have oxide layers that describe a bilayer model. An anhydrous inner layer which is Cr-rich, mainly Cr_2O_3 and $\text{Cr}(\text{OH})_3$ and outer Fe-rich hydrated layer, mainly Fe_2O_3 and $\text{Fe}(\text{OH})_2/\text{Fe}(\text{OH})_3$.

Qiang Guo et al.[56] studied the passive film formed on the martensitic stainless steel in neutral 3.5 wt% NaCl solution at different potentials. The study found that the passive layer formed at passivity potential is composed of iron oxides-rich outer layer (FeO , Fe_2O_3) and an inner layer rich in chromium oxides (Cr_2O_3 , $\text{Cr}(\text{OH})_3$) while the passive film formed at open circuit potential(OCP) shows a single layer rich in chromium oxides(Cr_2O_3 , $\text{Cr}(\text{OH})_3$ and Fe).

During the passive layer formation on dual phase steel, the diffusion stage, which involves the diffusion of oxygen ions through the metal oxide layer to the metal substrate, controls the layer formation process. The electrochemical reaction process is faster than the diffusion process and gets activated at the metal-metal oxide layer interface. This results in the passive oxide layer being an n-type semiconductor, as the layer predominates in oxygen vacancies or metal ions[57]. Some studies show that the Dual phase steels can be assumed to have a passive layer with a bilayer structure composed of an inner magnetite (Fe_3O_4) layer and an outer maghemite ($\gamma\text{-Fe}_2\text{O}_3$) layer[58, 59]. Due to the composition of dual phase steels, it is possible to exclude the effects of alloy elements and focus on the effects of the two different crystal phases.

Kei Yanagisawa et al.[12] studied the passive layer formed on dual phase carbon steel (50F50M - 50% Martensite and 50% Ferrite) by comparing it with the passive layers formed on carbon steel sheets of pure ferrite phase (100F - 100% Ferrite) and pure martensite phase(100M - 100% Martensite). The study showed that the reactivity of the pure martensite sample surface was higher than the pure ferrite sample surface. The dynamic polarization curves of the three samples show that the E_{corr} for the dual phase sample lies in between the 100M and 100F samples, with the 100M sample having lower E_{corr} values. The higher reactivity of the martensite phase surface was attributed to the high surface energy of the martensite phase. From the Mott-Schottky plots of steel specimens after film formation (see figure 2.12), it can be seen that the passive layers on all the specimens show n-type behavior with a positive slope for all the curves. The Mott-Schottky equation for n-type semiconductors was used,

$$C^{-2} = \left(\frac{2}{eN_D\epsilon\epsilon_0}\right)\left(E - E_{fb} - \frac{kT}{e}\right), \quad (2.1)$$

where C^{-2} ($10^9\text{cm}^4\text{F}^{-2}$), is the reciprocal square interfacial capacitance of the passive layer, e is the elementary charge, N_D is donor density, ϵ_0 and ϵ are permittivity in vacuum and the relative permittivity, respectively, E_{fb} is flatband potential, k is Boltzmann constant and T is absolute temperature. Mott-Schottky plots of the three samples showed that the donor density (N_D) values, obtained from the slope of the curves, indicated higher values for the 50F50M and 100M samples compared to the 100F sample. Since the number of defects in the passive film is related to the N_D , Yanagisawa ascribed the higher N_D of the samples with martensite, to the large number of lattice mismatches in the martensite phase compared to the ferrite phase. Additionally, the grain boundaries in the 50F50M phase was said to form a defective passive layer due to the different crystallographic orientations of the two phases involved. The passive film layer on dual phase steel is illustrated in figure

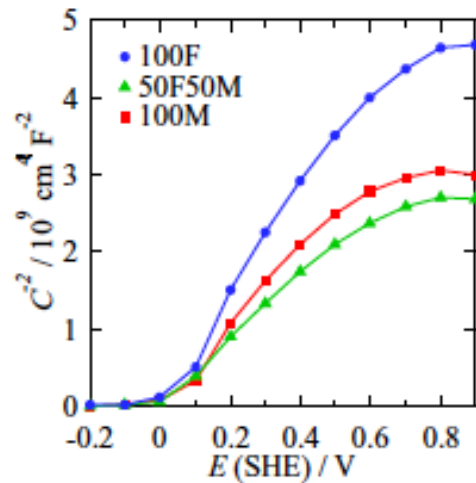


Figure 2.12: Mott-Schottky plots of steels after film formation at the film formation potential(E_f) = 0.9 V (SHE) for 3600 s[12].

2.13. It can be seen that the oxide layer on the martensite surface is thicker than that of the ferrite phase and has a larger fraction of Fe_3O_4 . The study concluded that the passivation behaviour of dual phase steels is limited by the partial passivity of the martensite phase.

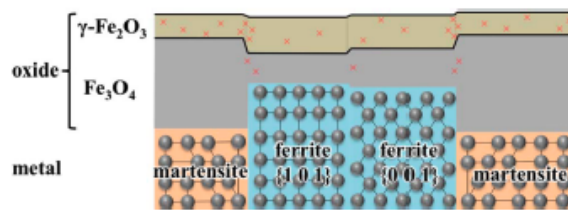


Figure 2.13: Schematic of passive film on dual-phase steel[12]. The thickness is in the order of nanometers.

2.3.2 Passive Layer Breakdown

Any factors that compromises the oxide formation on the metal surface are a cause for concern. Chlorine ions, which can be abundantly found in seawater and other saltwater environments, can inhibit oxide formation and compromise the integrity of the oxide layer formed, thereby posing a risk to metals that are protected by passivation. The formation of a defective oxide layer can also lead to corrosion degradation of the metal. Barbucci et al.[60] found that when the electrolytic medium has sulphate or chloride ions and the steel (304 stainless steel) has been cold worked, its increased susceptibility to pitting corrosion is due to dislocation pile-up. The presence of defects in the grains and at interfaces leads to the formation of a defective oxide layer. Austenization of a ferrite/perlite matrix to yield a ferrite/martensite matrix after quenching can lead to the release of chromium from carbides and the release of Carbon due to the austenite phase having higher solubility. Austenizing at high temperatures of up to 1100°C can increase the general corrosion resistance by the dissolution of carbides thus leading to the increase of chromium in the alloy matrix. But further increase in the austenizing temperature will be counterproduc-

tive as the release of additional carbon results in internal lattice stress. The presence of these internal stresses can cause the passive layer to be defective[61].

Exposing the passive layer to halide environments can cause the oxide layer to break down locally[62]. If repassivation does not occur, those areas may be susceptible to pitting or crevice corrosion. The next chapter will discuss the effect of Hydrogen on the passive layer of steels.

2.4 Hydrogen in Steels

It is a well-known fact that the presence of hydrogen (H) in metals, leads to a deterioration in the metals' mechanical and corrosion properties, which leads to a decline in its overall performance. Hence, it is crucial to understand the mechanisms of interaction between hydrogen and the metal. Over the last decade or so, the interest into hydrogen and its effects on the performance of steels has progressively increased. To satisfy the high structural and economic demands from the automobile sector and other industrial demands, high strength steels like dual phase steels have been developed. But, these steels have been reported to be susceptible to hydrogen induced degradation. Hydrogen can enter the steels in the production phase, during assembly and finishing, and while in service due to environmental factors. Hydrogen can also enter the steel during electrochemical processes such as pickling, electroplating and the the cathodic protection process to reduce corrosion degradation of the steel. Cathodic reduction reactions can take place on the surface of the steel, and generate H_2 . The decomposition of the electrolyte will also produce H^+ ions that can enter and get absorbed into the steel. The hydrogen that has entered the metal can accumulate at internal defects in the metal. Hydrogen absorption reactions can be studied using charging or permeation methods, see section 2.5.

Hydrogen transport behavior can be characterized by three points of interest,

- Absorption/desorption — How does the hydrogen enter and leave the material?
- Diffusion - How fast or slow does the hydrogen move within the material ?
- Solubility - How much of the hydrogen is there in the material?

In the upcoming sections, these mechanisms and properties will be discussed in detail.

2.4.1 Hydrogen entry and evolution

While some of the hydrogen formed in the reaction combines to release hydrogen gas, a portion of it stays in its monoatomic form and enters the metal surface. In the case of most metals, hydrogen can be physisorbed on the surface as H_2 molecules (thermal charging) and then undergo direct dissociation to atoms H^+ . Or in the absence of an active site, the H_2 molecules can undergo surface diffusion and then dissociation. A study by Besenbacher et al.[63] also notes that adsorption of hydrogen on the metal surface can induce surface reconstruction. Hydrogen evolution is a part of the cathodic reduction reaction in many electrochemical systems. The process usually takes the form,



The hydrogen cathodic reactions are governed by the surface reaction steps associated with chemisorbed H: hydrogen adsorption desorption, $H - H$ combination and surface — bulk diffusion. To predict the conditions for hydrogen uptake (entry

rate) into the metal with any accuracy requires knowledge of many variables, such as,

- nature of the metal,
- thermal–mechanical history of the metal,
- surface conditions of the metal,
- composition of the electrolyte,
- cathodic current density or electrode potential,
- temperature of the system[13].

The kinetics of the hydrogen reduction reaction at the cathode, on bare metal electrode surfaces, is determined by the cathodic overpotential, and surface conditions such as, density of sites in the metal for adsorption of hydrogen and the free energy of the hydrogen that has been adsorbed[13]. Figure 2.14 shows the energy potential vs distance (w.r.t the metal) curves for hydrogen in or near the metal. It shows the different hydrogen states such as the physisorbed and chemisorbed H in the initial few atomic layers, the H in the sub-surface of the metal and the dissolved H in the bulk[32].

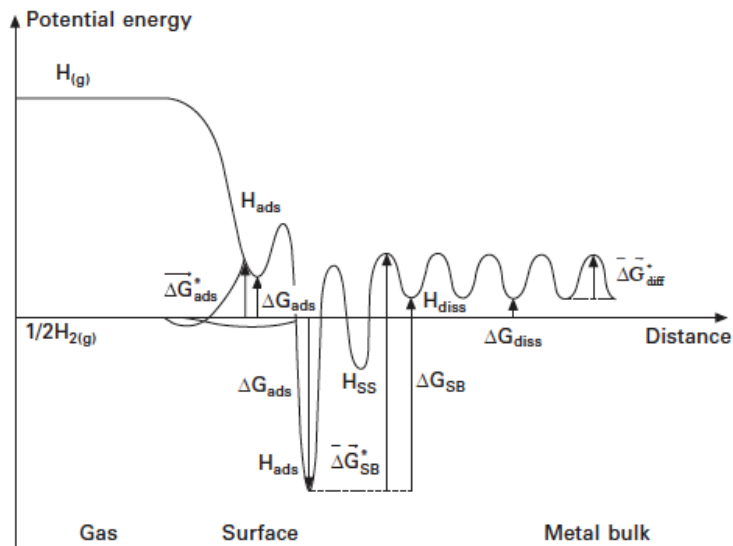


Figure 2.14: Diagram of the potential energy vs. distance curves for the various Hydrogen states at the metal–gas interface; the two adsorption states (weakly bonded, on-top, sites and strongly bonded, chemisorbed, sites), the sub-surface state (H_{ss}) and the bulk dissolved (absorbed) state H_{diss} . [13]

The hydrogen surface reactions in an aqueous electrolyte involve two different pathways for hydrogen uptake into the metal. Hydrogen adsorption in an aqueous medium can either occur chemically by the dissociation of dissolved hydrogen or electrochemically from H_3O^+ or H_2O depending on the pH of the electrolyte.

- Chemical pathway for H adsorption
 - First the dissolution of hydrogen gas in water takes place,
 $H_2(g) \rightleftharpoons H_2(aq)$
 - Then the dissolved hydrogen is transported to the surface of the metal electrode
 - Finally, direct dissociative adsorption takes place,
 $H_2(aq) + 2(M)aq \rightleftharpoons 2H(ads)(M)aq$, where (M)aq is a hydrated site where the H can be adsorbed and H(ads)(M)aq shows the H atom that is adsorbed in a site (M)aq and hydrated.

- Chemical pathway for H desorption
 - The reverse reactions of H adsorption is the combination desorption of hydrogen atoms. it is also known as the Tafel reaction.
- Electrochemical pathway for H adsorption (Volmer reaction)
 - In this pathway, hydrogen adsorption is assisted by the presence of a potential difference. Depending on the pH, reduction of H_3O^+ or H_2O takes place.
 - In an acidic electrolyte, after the rapid transportation of the hydrated proton from the solution to the double layer on the cathodic electrode surface, the hydrogen is adsorbed by electron transfer from the metal electrode to the H_3O^+ in the outer Helmholtz plane.

$$\text{H}_3\text{O}^+(\text{aq}) + e_{-(\text{M})} + (\text{M})\text{aq} \longrightarrow \text{H}(\text{ads})(\text{M})\text{aq}$$
 - In a neutral or basic electrolyte,

$$\text{H}_2\text{O}(\text{l}) + e_{-(\text{M})} + (\text{M})\text{aq} \longrightarrow \text{H}(\text{ads})(\text{M})\text{aq} + \text{OH}^-(\text{aq}),$$
 where $e_{-(\text{M})}$ is an electron from the metal M. This reaction is less dominant than the proton adsorption reaction and mostly only takes place when the proton concentration is low.
- Electrochemical pathway for H desorption

The recombination of H_3O^+ or the recombination of H_2O , depending on the pH can lead to electrodesorption of the hydrogen.

 - In an acidic electrolyte,

$$\text{H}(\text{ads})(\text{M})\text{aq} + \text{H}_3\text{O}^+(\text{aq}) + e_{-(\text{M})} \longrightarrow \text{H}_2(\text{aq}) + (\text{M})\text{aq}$$
 - In a neutral or basic electrolyte,

$$\text{H}(\text{ads})(\text{M})\text{aq} + \text{H}_2\text{O}(\text{l}) + e_{-(\text{M})} \longrightarrow \text{H}_2(\text{aq}) + \text{OH}(\text{aq}) + (\text{M})\text{aq}$$
- Surface - Bulk (of the metal electrode) transfer

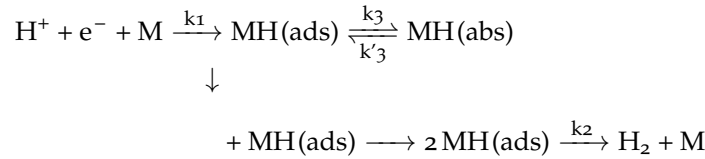
$$\text{H}(\text{ads})(\text{M})\text{aq} + [\text{M}] \longrightarrow \text{H}_{\text{diss}}[\text{M}] + (\text{M})\text{aq},$$
 where $[\text{M}]$ indicates a vacant interstitial site in the bulk metal matrix and $\text{H}_{\text{diss}}[\text{M}]$ indicates a hydrogen atom that is bonded to the $[\text{M}]$ site.

Surface modifiers on the metal such as a metal oxide layer or the presence of electronegative elements of columns 14–17 in the periodic table, that are chemisorbed can influence H entry into the metal. While pure metal oxide layers are immune to H gas adsorption by dissociation, they cannot completely withstand the adsorption of atomic hydrogen, which in certain stoichiometric oxides can diffuse relatively fast. At temperatures below 400°C , hydrogen adsorption is impeded by the oxide film layer on the metal substrate[13]. Likewise, passive layers formed of metal surfaces after anodization can impede hydrogen adsorption. On most transition metals, the presence of electronegative elements in the electrolyte is said to poison the surface hydrogen reactions that take place, since these elements are more strongly chemisorbed than H on the metal. The addition of elements from groups 15 and 16 of the periodic table in the electrolyte can promote the penetration of hydrogen into the bulk metal for metals such as iron and steels, Pd, and Pt[13].

The described model in Figure 2.14 for H adsorption and absorption does not take into account the passive oxide layer that is present in most corrosion resistant alloys, like stainless steels. Intuitively, it can be assumed that the presence of the oxide layer adds another hindrance to hydrogen absorption. The oxide film decreases the rate of hydrogen uptake into the metal[32].

Perng et al.[64] summarised the method of hydrogen evolution and entry in iron and nickel as shown below, where M denotes either iron or nickel, and k_1, k_2, k_3 and k'_3 are reaction rate constants. The reaction shows a combination of discharge-chemical absorption. This reaction follows the model of electroadsorption of hydrogen mentioned previously. From a review of literature done by Perng, it was

concluded that in the case of iron and nickel, for electrochemical means of hydrogen charging, the hydrogen solubility in the metal was proportional to the square root of the cathode charging current density (?? will give a better idea about hydrogen charging of metals).



Bockris et al.[65] on the issue of hydrogen entry and evolution in α -Iron (acid electrolyte) summarised that the presence of grain boundaries did to affect the hydrogen permeation rate or the hydrogen entry mechanism, since the permeation rate was found to be similar for both single crystal and polycrystalline iron.

2.4.2 Hydrogen Solubility - Iron and Steels

Thorough knowledge of the quantity of hydrogen in metals and its distribution in the metal lattice is important to better understand the effect of H on the metal. The lattice solubility of hydrogen in metals varies over a range of $10^{-10} - 10^{-1} \text{ mol cm}^{-3}$ [66]. The hydrogen solubility in a metal influences the concentration of H that can be found in the metal which thereby influences the mechanical properties of the metal. If the hydrogen dissociation enthalpy is greater than or less than zero, the hydrogen absorption in metals can be an exothermic or endothermic process. If $\Delta H_{Hdiss} < 0$, the process is exothermic and the concentration of H decreases with increasing temperature and if the $\Delta H_{Hdiss} > 0$, the process is endothermic and the concentration of H increases with temperature. Iron displays an endothermic behavior regarding hydrogen absorption.

Iron which has a BCC structure has a low hydrogen solubility of about $3 \times 10^{-9} \text{ mol cm}^{-3}$, $2 - 3 \times 10^{-8} \text{ H/Fe}$ at 25C and 1 atm. Apart from the hydrogen in the bulk solution of the metal, hydrogen can be trapped at lattice defects or interfaces. H can also be chemically combined with impurities in the metal. At ambient temperatures, in pure iron, the hydrogen can be found not in the crystal lattice but at trapping sites.

The solubility of Hydrogen in steels is largely dependent on the steels' crystal structure, alloy composition and temperature. The amount of hydrogen in steels usually does not exceed 1 mass ppm[67]. Compared to hydrogen solubility in pure iron at room temperature, the solubility in steel is higher mainly due to hydrogen being trapped at lattice defects. H is found to be more soluble in the austenitic phase than the ferrite or martensite phases. The solubility of hydrogen in duplex stainless steel with 50% austenite phase is determined by the solubility in the austenite phase.

Ferritic steels have solubility rates that are close to that of α - Iron, while austenitic stainless steels have solubility rates that are 3 - 20 order of magnitude larger. These higher solubilities are firstly due to the different crystal structure of austenite and secondly due to the presence of alloying elements such as Ni and Cr. Retained austenite phase is also known for its high hydrogen solubilities.

A study by Song et al.[68] explains exactly why H is more soluble in the austenite phase than the ferrite phase with respect to its crystal structure. Comparison of the hydrogen dissolution enthalpy for hydrogen at interstitial and octahedral sites in both austenite and ferrite phase was done. It was found that in the austenite phase, hydrogen favoured the octahedral sites while in the ferrite phase, hydrogen favoured the interstitial sites. The hydrogen dissolution energy for H at octahedral sites in the austenite phase was smaller than that for H at interstitial sites in the ferrite phase. This shows the favourability for the hydrogen being more soluble in the austenite phase than the ferrite phase.

Martensitic steels are said to have high solubility for hydrogen due to the large network of dislocations and interfaces present between the martensite laths[69]. On the other hand the solubility of hydrogen in austenite is still higher than that martensite. The Figure 2.15 shows the solubility of hydrogen in different steels.

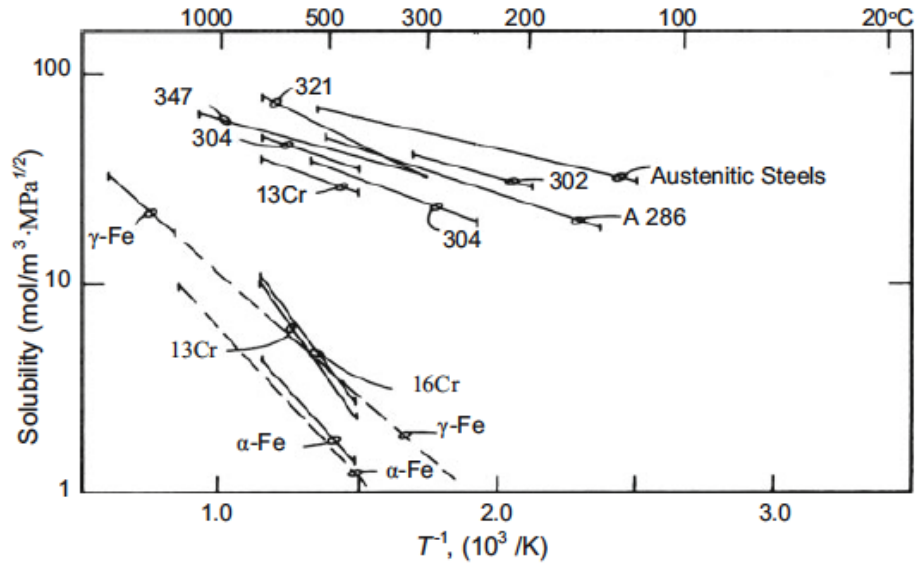


Figure 2.15: Solid solubility data of hydrogen in stainless steels and the data was obtained through electrochemical permeation experiments [14]. The hydrogen solubility in grades of ASS, such as AISI 304, 302, 321 and 347, seems to be in the range of $25 - 90 \text{ mol/m}^3 \cdot \text{MPa}^{0.5}$. The Hydrogen solubility in 13Cr and 16Cr, which are martensitic stainless steels, seems to be in the range of $3 \text{ to } 60 \text{ mol/m}^3 \cdot \text{MPa}^{0.5}$. In alpha ferrite, the hydrogen solubility seems to be in the range of $1 \text{ to } 10 \text{ mol/m}^3 \cdot \text{MPa}^{0.5}$. These solubility ranges are taken with respect to different temperature ranges.

2.4.3 Hydrogen Diffusion and Trapping - Iron and Steels

The understanding of H transportation and trapping mechanism is crucial when reviewing its effects on iron and steels. Hydrogen diffusion is the transportation of H from a region of high concentration to a region of low concentration. There are two types of H that can be found in a metal, diffusible hydrogen and trapped hydrogen, which is non diffusible. H gets trapped in various crystal imperfections that include vacancies/voids, dislocations, grain boundaries, phase boundaries, solutes, precipitates, inclusions, interfaces like carbide interfaces and crack tips to mention a few. Since diffusible H can move from one interstitial site to another, it is the trapped H that spends more time immobile. The trapping site distribution of H affects many aspects of the metal with respect to hydrogen, such as the diffusion coefficient, the solubility and the susceptibility of the metal to H embrittlement. The solubility of H in a metal increases by hydrogen trapping. The driving force for H diffusion is the chemical potential gradient that arises due to the concentration (C , mol cm^{-3}) gradient across the metal. The steady state diffusion flux (J_∞ , $\text{mol cm}^{-2} \text{ s}^{-1}$) of H permeating through the metal can be described by Fick's first law as,

$$J_\infty = -D \frac{\partial C}{\partial x}, \quad (2.2)$$

where D ($\text{cm}^2 \text{s}^{-1}$) is the diffusion coefficient. Microscopically, this value denotes the jumping frequency of the atoms in the crystal lattice.

$$D = D_0 \exp \frac{Q}{RT}, \quad (2.3)$$

where Q is the activation energy for the diffusion process, D_0 is the pre-exponential constant term, and R ($\text{J mol}^{-1} \text{K}^{-1}$) is the gas constant. Permeation experiments can be used to measure the values for D and the sub-surface hydrogen concentration (C_0). Fick's first law can also be used in the case of H entry by cathodic polarization.

$$C = \frac{\phi \sqrt{p_i}}{D}, \quad (2.4)$$

Where C_i is the input H concentration in equilibrium with the H_2 gas of pressure p_i and ϕ is the permeability coefficient. Both the lattice H and the weakly trapped reversible H are counted when the concentration of diffusive hydrogen is calculated. The range of hydrogen coefficients for iron and steels can be seen in Figure 2.16. section 2.5 looks at some of the ways to measure the hydrogen diffusion coefficient. The equations mentioned above do not account for discrete processes such as reversible and irreversible trapping of hydrogen, and therefore the Fick's laws have to be modified. The general formulation given below was made by McNabb and Foster[70].

$$\frac{\partial C_L}{\partial t} + \sum_i N_i \frac{\partial \theta_i}{\partial t} = D_L \nabla^2 C_L \text{ and } \frac{\partial \theta_i}{\partial t} = k_i C_L (1 - \theta_i) - p_i \theta_i, \quad (2.5)$$

where k and p are trapping and detrapping parameters, C_L is the concentration of H in the lattice sites per unit volume, N_L is the number of sites per unit volume and θ is the fractional occupancy.

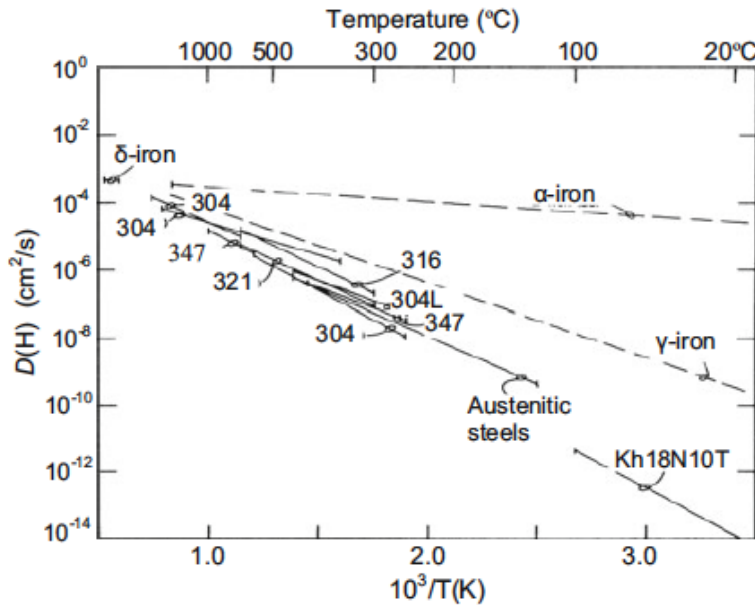


Figure 2.16: Hydrogen diffusion coefficients in austenitic stainless steels[14].

Concerning the structural aspects of H diffusion, in FCC metals like Pd, Ni and Pt, the H atom cannot jump directly from one octahedral site to another in the $\langle 110 \rangle$ directions, because of close-packed atomic rows. Instead the H atom has to make intermediate jumps from octahedral sites in the $\langle 111 \rangle$ directions, to the eight nearest neighbour tetrahedral sites and then back again to the octahedral sites.

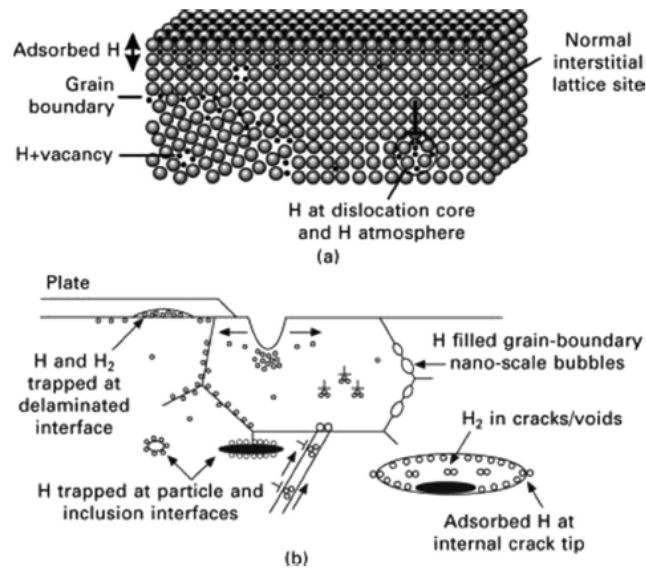


Figure 2.17: Representation of hydrogen at interstitial lattice site and trapped location at (a) atomic scale and (b) microscopic scale[15].

Meanwhile, for BCC metals like Fe, H atom can make direct jumps from one tetrahedral site to the four nearest neighbour tetrahedral sites in the $\langle 110 \rangle$ directions, or direct jumps from one octahedral site to the two nearest neighbour octahedral sites in the $\langle 100 \rangle$ directions. Now, the diffusion coefficient can also be described in terms of the number of jumps per time that the atom makes, which is essentially the jumping frequency of the atom. Therefore it would see that the hydrogen diffusion coefficient for BCC metals would be higher when compared to FCC metals, as the jumping frequency would be higher for lower activation energy involved in H diffusion.

When H gets trapped in lattice imperfections, there is a reduction in the effective diffusion coefficient. This thereby reduces the H transportation rate in the metal. The decrease is dependent on,

- Strength of the traps, indicated by the binding energy (E_b) of H in the trap,
- Density of trapping sites, N_T . N_T is the number of trapping sites per unit volume.

Traps can be reversible or irreversible in nature. Irreversible sites are characterized by high activation energies. The activation energy for an irreversible trap is high that of lattice diffusion. In fact the activation energy for an irreversible trap would be higher than the E_b for the trap[71]. Carbide interfaces, solutes, precipitates and inclusions are examples for irreversible traps, where a large potential barrier has to be surmounted for the H to escape. Reversible H traps, on the other hand, have shallow energy barriers and detrapping is much easier. The reversibility of trapping sites is dependent on the temperature. Dislocations, grain boundaries, and microvoids are examples for reversible H traps. Figure 2.17 and Figure 2.18 show the schematic for H atoms at trapped sites and in the lattice. And Figure 2.19 shows a table with the H trapping sites and their corresponding trapping activation energies for iron and steels.

Kiuchi et al.[72] found that in carbon and low alloy steels, if there were no H traps, the diffusivity was the same as that of pure iron, $D_L = 7.23 \times 10^{-8} \exp[-5.69 \times 10^3 / RT] \text{ m}^2/\text{s}$, at temperatures below 80 C and the H diffuses through tetrahedral sites. For temperatures way above 90C, the H diffuses through tetrahedral sites and octahedral sites, $D_L = (1 - 2.5) \times 10^{-7} \exp[-(6.7 - 7.12) \times 10^3 / RT] \text{ m}^2/\text{s}$. In these steels, the

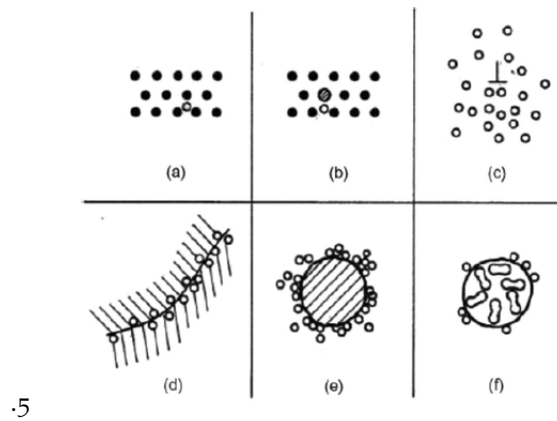


Figure 2.18: Various location where hydrogen atoms are presented in microstructure are (a) solid solution; (b) solute hydrogen pair; (c) dislocation atmosphere; (d) grain boundary accumulation; (e) particle-matrix interface accumulation; (f) void containing recombined hydrogen[16].

major trapping sites are dislocations, and interfaces between the crystal matrix and particulates such as carbides and nitrides[32].

S.N.	Trapping sites	Trapping activation energy (KJ/mol)
Reversible trapping sites		
1	Iron lattice	5.4–7.1
2	Grain boundary	17.2–18.6
3	Austenite/martensite interface	22
4	Dislocation	26.4–26.8
5	Austenite/dislocation boundary	37
6	Microvoid	35.2–40
7	Fe oxide interface	47
Irreversible trapping sites		
8	Ferrite/cementite interface	66.3–68.4
9	Cr carbide interface	67
10	Y ₂ O ₃ interface	70
11	MnS interface	72
12	Al ₂ O ₃ interface	79–86.2
13	Fe ₃ C interface	84
14	TiC interface	68–137

Figure 2.19: H trapping sites and their corresponding trapping activation energies for iron and steels[17].

Martensitic stainless steels were studied by various authors to understand H diffusion behaviour. AISI 410 AND 13Cr steels were taken into account. It was found that in AISI 410 steels, dislocations acted as reversible trapping sites and interface between the matrix and carbide particles acted as irreversible trapping sites. The effect of the irreversible traps were said to dominate over the reversible traps. On the other hand, in super 13Cr steel, irreversible H traps did not show any effect on the hydrogen diffusivities. The presence of 12% austenite phase in this steel lends a contribution to the H diffusivity as, the interface between the austenite and martensite phase is a factor that affects the diffusion coefficient[32].

In austenitic stainless steels, weak trapping takes place and the trapping is mainly dependent on the alloy composition[14]. According to a study by Ronevich[73] on the hydrogen embrittlement of advanced high strength steels, it was found that the Twinning-induced plasticity (TWIP) steel samples studied were not susceptible to hydrogen degradation. This was attributed to the low diffusivity of H in the austenite phase at room temperature. The diffusion coefficient of the austenite

phase is found to be eight orders of magnitude lower than that of the ferrite phase at the same temperature. Because of this low diffusivity of H, the H (introduced by the charging process) is limited to the surface atomic levels of the steel instead of the bulk. Dislocations, grain boundaries, and twins were also found to be the major H traps and had a significant effect on the H diffusion.

Mine et al.[74] showed in their study that, when austenite transforms to martensite, excess H is released from the austenite phase. This excess H can then quickly diffuse through the martensite phase. This is because hydrogen has a higher diffusivity in the martensite phase than in the austenite phase, but a higher solubility in the austenite phase. The austenite phase is almost said to behave as a reversible trapping site, since it lowers the trap binding energy, making hydrogen diffusion easier.

In Duplex stainless steels such as 22 Cr and 25 Cr, H trapping occurs mainly at the ferrite - austenite interface and at ambient temperatures. Compared to 13 Cr, which has 12% austenite phase, the H diffusivity in 22 Cr and 25 Cr is lower and they have more austenite phase (50%)[75].

Advanced high strength steels(AHSS) have complex microstructures, therefore studying their H diffusion and trapping properties is a complicated endeavour. In dual phase steels Winzer et al.[76] reported H trapping at the ferrite - martensite interface. Dislocation and the ferrite - martensite grain boundaries act as reversible trapping sites in DP steels[74]. The diffusion coefficient was also said to increase with increasing amount of the martensite phase in AHSSs due to the martensite phase having high dislocation density[77]. On the other hand the presence of Aluminium reduces the dislocation density in TWIP steels, this thereby eliminates hydrogen diffusion channels to an extent[71]. Researchers found that the major irreversible trapping sites were inclusions such as MnS.

Rudomilova et al.[78] reported that the hydrogen diffusion coefficient for martensite was five times lower than that for ferrite. The large network of dislocations and the interfaces between the martensite laths were said to be the cause for the lower D. Steels with higher quantities of bainite were reported to have lower D values, due to the large number of reversible traps such as dislocations and bainite lath boundaries. The presence of fine carbides in steels acts as hydrogen traps and thereby reduce H diffusivity through the metal. And since most working metals do not have perfect crystal lattices, it is important to do more study on them to avoid failure. The interactions of hydrogen with lattice defects, inclusions and impurities in the crystal matrix are still not fully understood. It is also difficult to compare diffusivity data, due to sensitivity towards the environment, surface effects, combined effects of traps and composition of the steels. Rudomilova et al.[79] also reported that, when H permeation transient curves were measured at different cathodic current densities for a DP1000 sample, the H diffusion coefficient was not affected by the smaller current densities. In contrast, the H diffusion rate increased for a current density of 100 mA/cm^2 . This behavior was probably due to the H being trapped in all the available trapping sites, leaving only the lattice diffusible H behind. This indicates increasing diffusivity with increasing negative cathodic polarization potentials.

2.4.4 Hydrogen and the Passive Oxide Layer on Steels

The absorption rate of hydrogen for metals is strongly decreased by oxide layers on the surface of the metal at ambient temperatures. The rate determining step in H absorption, which is the dissociation of H₂, is impeded by the quantity of oxygen absorbed. In more detail, the reaction coefficient of the dissociation reaction, changes by many orders of magnitude based on the amount of oxygen absorbed. The oxide layer usually acts as a protective layer against H permeation in metals. There is reduced H diffusion and solubility in the oxide layer for most metals[32].

Thin suboxide layers that do not have maximal valance cations, impede H adsorption to a much smaller extent. Different types of chemical compositions in steels tend to form surface oxides with varying properties.

Even though oxide layers are able to prevent H adsorption to a large extent, they can still fail if the steel undergoes deformation. Freshly created steel surfaces after elongation, are vulnerable to H - H dissociation on the surface[80].

Zeng et al.[81] studied the effect of hydrogen on the passive film on microalloyed steel (X70) by charging the steel with hydrogen before passivating it. They reported that the presence of H in the passive film, decreased the film's stability and retarded its formation. H increases the rate of interstitial cation and anion transport in the passive film. This thereby increases the amount of ferrous ions and oxygen vacancies in the film leading to a degradation in film integrity. Hydrogen was also reported to increase the capacitance and donor density of the passive film.

Luo et al. studied the effect of H in the passive film of a Cr-Ni-Mo-N duplex stainless steel by exposing the passive film to H charging with different charging times[82]. It was reported that H increased the conductivity of the passive film. With an increase in charging time from 30 to 360 mins, the amount of Cr_2O_3 decreased from 41.6 at. % - 32.4 at.% and the amount of $\text{Cr}(\text{OH})_3$ increased from 23.9 at. % - 27.1 at.%. This decrease in the amount of Cr_2O_3 can reduce the corrosion resistance of the steel. The presence of H was also found to decrease the thickness of the passive film. In this paper, H charging was found to degrade the passive film formed on 2205 Duplex stainless steel. Overall, hydrogen is found to increase the passive current in steels[82, 83, 84]. But there is not enough experiments done on steels with similar properties in similar environments to generate comparable results.

In an article by Legrand et al.[18], they studied the consequences of an oxide layer on the hydrogen permeation test in the exit side of a martensitic steel membrane sample. The oxide layer was reported to act as a global deterrent to hydrogen diffusion and the H accumulates within the martensite membrane. The diffusion coefficients for some protective layers and oxides is shown in Figure 2.20. The oxide layer in steels is usually about 3-5 nm thick and its hydrogen diffusion coefficient would land in between that of wustite and hematite. The passive layer on iron that is mentioned in Figure 2.20, is assumed to be a bilayer structure, with an inner Fe_3O_4 layer and an outer $\gamma\text{-Fe}_2\text{O}_3$ layer.

Material + Oxide	Diffusion coefficient (m^2/s)
Palladium	10^{-11}
Wustite on steel	10^{-14}
Passive film on iron	10^{-16}
Hematite on steel	10^{-21}

Figure 2.20: Oxide diffusion coefficients for various materials[18].

More details into the effect of Hydrogen on the mechanical behavior of iron and steels is out of the scope of this study.

2.4.5 Impact of Hydrogen absorption on the properties of Iron-based alloys

The presence of Hydrogen in Iron-based alloys can impact different aspects of the metal such as its mechanical properties, microstructure or corrosion behaviour. In particular, hydrogen can cause the following harm to metals and alloys: hydrogen-induced blistering, hydrogen embrittlement (HE), cracking brought on by the cre-

ation of hydrides, hydrogen attack, and cracking brought on by the precipitation of internal hydrogen[85]. Hydrogen embrittlement (HE) is known as the decrease in a metal's ductility brought on by hydrogen absorption, also known as hydrogen-assisted cracking or hydrogen-induced cracking (HIC). There is intense debate over the impact of hydrogen on the mechanical behavior of steel. On the other hand, the severe impacts of hydrogen on the mechanical integrity of engineering structures are well established, and the issue needs to be addressed head-on if society is to transition to a hydrogen economy in the future. Because of the presence of dissolved hydrogen at a level of a few atomic parts per million (appm) in steel, its fracture toughness can be drastically reduced. So far mainly the so-called diffusible hydrogen has been identified as the main factor leading to hydrogen embrittlement[86]. In a study by Dong et al. on the effects of hydrogen-charging on the susceptibility of X100 pipeline steel to hydrogen-induced cracking, it was found that the steel will be more susceptible to HIC after hydrogen charging. The inclusions in the steel, such as aluminum oxides, titanium oxides, and ferric carbides, are where cracks start to appear most frequently[87].

The corrosion impact on some metals is a further consequence of hydrogen-metal interaction. For instance, it has been demonstrated that hydrogen sorption on stainless steels has a detrimental impact on the corrosion behavior because it may decrease the durability of their distinctive passive protective coating. Although the exact mechanism is still unclear, experimental evidence has shown that hydrogen encourages the dissolution of the passive layer on type 304 stainless steel and hinders the process of re-passivation. Additionally, the time frames for pitting corrosion are shortened as a result of these circumstances[88].

2.5 Techniques to study Hydrogen/Material Interaction

2.5.1 Methods to Charge Hydrogen

Studying the effect of hydrogen in steels involves the use of a method that can charge hydrogen in such a way that there is a homogeneous distribution of H_2 across the sample. There are a variety of methods that can be used to charge samples with hydrogen. Some of the H-Charging methods are listed below:

- High-Pressure Hydrogen Gas and Autoclave Methods - This technique is used for H charging in dry conditions. The H_2 gas molecule dissociates to two hydrogen atoms that then get adsorbed on the steel surface. The steel[89] can then absorb the adsorbed hydrogen.
- Cathodic Charging Methods - Cathodic H_2 charging is sometimes preferred over the other methods because of simplified testing requirements. The metal sample acts as the cathode and the anode is usually platinum. Both the cathode and the anode is submerged in an electrolyte. On the application of an electrical potential across the electrodes, decomposition of the electrolyte takes place, and protons (H_3O^+ ions) are generated. Due to the applied potential, there is a flux of the electrons through the electrodes and protons through the electrolyte solution. The flux leads to a high concentration of hydronium ion on the surface of the cathode (the sample). The potential also acts as a driving force for hydrogen diffusion through the sample[90]. Table 2.3 lists the various cathodic hydrogen charging parameters for different materials that have been collected from literature.

Table 2.3: Table on the cathodic hydrogen charging parameters from literature

Material	Cathodic charging conditions				Hydrogen concentration		Reference
	Electrolyte	Temperature	Charging duration	Electric Current/Potential			
Inconel 718	NaHSO ₄ and KHSO ₄ at a composition ratio of 1:1 (mol/mol)	573 K	30 hours	Fixed current density of 0.5 mA/mm ²	20 wppm	[91]	
AISI 304 stainless steel	Melted salt bath of NaHSO ₄ and KHSO ₄	423 K	3, 6 and 12 hours	0.850 V Ag ₂ /Ag ⁺ fixed potential Fixed current of 20 mA/cm ²	25, 45 and 60 ppm (at 3, 6 and 12 hours respectively)	[92]	
Inconel 718	NaHSO ₄ and KHSO ₄ at a composition ratio of 1:1 (mol/mol)	573 K	25 hours	Fixed current density of 1 mA/mm ²	20 wppm	[93]	
Inconel 718	1 N H ₂ SO ₄ solution	Room Temperature	8 hours	Applied current density of -100 mA/cm ²	The tensile behaviour was studied	[94]	
DP600	Borax/glycerol	Room Temperature	2 hours	Applied current density of 10 mA/cm ²	0.35 wppm	[95]	
DP600	1 g/L of thiourea in a 0.5 M H ₂ SO ₄ solution	Room Temperature	2 hours	Applied current density of 0.8 mA/cm ²	6.3 wppm	[96]	
F22 and X65 Steels	0.4 mol/L of CH ₃ COOH + 0.2 mol/L of CH ₃ COONa, pH 4.3, 600 ppm hydrated NaS	Room Temperature	20 hours	Current density equal to 0.5 mA/cm ²	0.6 - 2 wppm	[97]	
X70 and 46Mn Steels	0.5 M H ₂ SO ₄ solution	Room Temperature	2 hours	Constant current density ranging from 0 mA/cm ² - 70 mA/cm ²	X70 - at 2 mA/cm ² , 0.43 x 10 ⁻⁶ mol/cm ³ and at 70 mA/cm ² , 3.57 x 10 ⁻⁶ mol/cm ³ 46Mn - at 2 mA/cm ² , 0.91 x 10 ⁻⁶ mol/cm ³ and at 70 mA/cm ² , 4.22 x 10 ⁻⁶ mol/cm ³	[98]	
Several types of austenitic stainless steels, duplex stainless steel and austenitic Ni based alloys	1. 3% NaCl solution 2. 3% NaCl solution containing 3g/L NH ₄ SCN 3. 1 N H ₂ SO ₄ solution containing 1.4 g/L (NH ₄) ₂ SC	Room Temperature	48 hours	A range of constant potentials or constant charge densities as can be seen in [99] were used	Average hydrogen concentration of 22 ppm	[99]	
SUS 316L	0.5 mol/l H ₂ SO ₄	50 C	168 hours	Current density of 1 mA/mm ²	20 - 60 ppm	[100]	

2.5.2 Methods to Quantify Hydrogen in Steels

The amount of absorbed hydrogen in steel can be measured using many technologies, like thermal conductivity method, fusion extraction method, vacuum extraction technique, hot-extraction thermal conductivity method, gas chromatography, Barnacle Electrode method, Secondary Ion Mass Spectrometry (SIMS) and electrochemical methods[98]. Some of the H-Quantification and detection methods are listed below:

- Thermal Desorption Analysis (Thermal Desorption Analysis (TDA) - Thermal desorption analysis is a powerful technique used to study the hydrogen diffusion process, gas-surface interactions and hydrogen trapping effects in the steel. Temperature variation (usually constant rate linear variation) using a temperature controller is used to study various phenomena. The gas evolved is detected using a mass spectrometer.
- Electrochemical Methods - The electrochemical method involves oxidizing the reduced hydrogen that has been absorbed in steel.
 - Devanathan et al.[101] developed the most commonly used electrochemical method to quantify adsorbed hydrogen, the electrochemical hydrogen permeation method. Permeation curves (i_{∞}) hydrogen flux vs time) can provide information such as the diffusion coefficient(D), the steady-state permeation rate, and the trapping behaviour of hydrogen in the steel, H charging concentration, etc.
 - Potential-based techniques like cyclic voltammetry and potentiostatic oxidation - These techniques can be used to measure the diffusible hydrogen concentration in materials that are charged with hydrogen. There is no delay between the steps of hydrogen intake (Electrochemical Charging) and measurement. A study by the Ozdirik et al. proposed an electrochemical procedure for monitoring hydrogen sorption/desorption in steels[102].

2.5.3 Cyclic Voltammetry (CV) to study H/material Interaction

Cyclic voltammetry is an electrochemical method often used to study oxidation and reduction reactions in an electrode/electrolyte system. A potential is applied to the working electrode during the experiment, and this potential fluctuates over time. The current passing through the working electrode is measured as a function of the electrode potential. To calculate the net amount of charge and, therefore, the number of electrons involved in the redox process, the area under the current versus potential plot can be integrated. The working electrode's voltage starts at an initial potential E_1 , often chosen to prevent the chemical species under investigation from being first oxidized or reduced. After following a linear sweep of the potential to a voltage, E_2 , the scan's direction is switched. The specified potential window ($E_2 - E_1$) is set such that the relevant oxidation or reduction process occurs inside it (refer figure 2.21).

The Nernst equation links the potential of an electrochemical cell (E) to the species' standard potential (E_0) and the relative activity of the oxidized (Ox) and reduced (Red) analytes in the system at equilibrium. F stands for the Faraday constant, R for the universal gas constant, n for the number of electrons, T for temperature and $[Ox]$ and $[Red]$ represent the concentrations of the oxidised and reduced species respectively in the equation below.

$$E = E^0 + \frac{RT}{nF} \ln \frac{[Ox]}{[Red]}$$

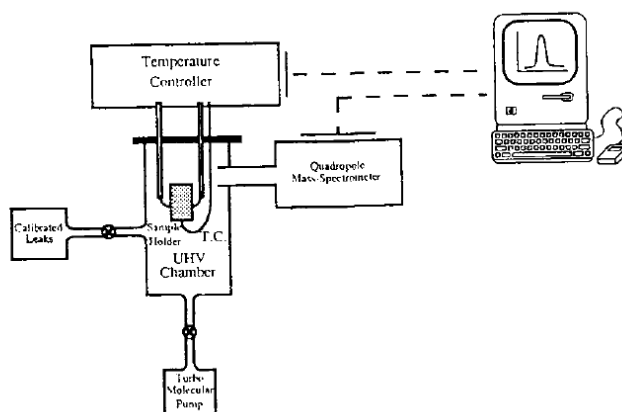


Figure 2.21: (I): Applied potential as a function of time for a generic cyclic voltammetry experiment, with the initial, switching, and end potentials represented (A, D, and G, respectively)[19].

When an external voltage is supplied to the electrochemical cell, the concentration of oxidized and reduced species fluctuates in accordance with the Nernst equation until equilibrium is reached. A current is produced in the cell as a result of the exchange of electrons that occurs during this process. A voltammogram is a graph of the resulting current against cell potential[19]. The evolution of hydrogen during cathodic charging is an oxidation process. Therefore, CV can be used to investigate the H/material interaction[103, 102, 37, 104]. Various methods have also been used to quantify the desorbed hydrogen from CV. The method that calculates the amount of hydrogen corresponding to the hydrogen peak found in the initial CV scan following hydrogen charging is the one that is most frequently utilized[103, 102, 37].

2.5.4 Electrochemical Impedance Spectroscopy (EIS) to study H/material Interaction

Despite the fact that there have been many studies on the iron-based alloys/hydrogen system, impedance measurements, a very effective technique for separating the many processes involved in complex reaction mechanisms, have only been used in a small number of studies. For example, in a study by C. Zheng and G. Yi on the stress corrosion cracking behaviour of 2205 DSS in 0.5 M H_2SO_4 under Hydrogen charging conditions, it was reported that the passive layer on 2205 DSS showed signs of degradation after the material was charged with Hydrogen. This phenomenon was reflected by the phase shift in the EIS which is closely related to the breakdown and repassivation of the passive film[105]. A study by Dan et al. also concluded a similar theory. After charging Alloy 690 with Hydrogen in a boric acid and sodium sulphate solution, the EIS results reported a decrease in the passive film resistance and the charge transfer resistance. This is an indicator of the decrease in the overall corrosion resistance of the material. XPS studies conducted in the same study after Hydrogen charging attributed the decrease in corrosion resistance to the increase in defects in the oxide layer, causing the oxide layer to be less compact[106]. This trend with respect to the decrease in corrosion resistance with hydrogen charging was reflected in multiple studies[105, 106, 107, 104].

2.5.5 Surface mapping of hydrogen

Detection of hydrogen in steels is one of the most problematic aspects involved in the study of hydrogen permeation phenomena and hydrogen embrittlement. Depth profiling can be carried out using Nuclear Reaction Analysis (NRA) and surface analysis (visualization of local hydrogen distributions on the surface) can be carried out using hydrogen micro-print technique, SIMS, Kelvin probe force microscopy, tritium autoradiography and Electron Stimulated Desorption (ESD) technique[108]. Scanning Kelvin Probe (SKP) can be used to determine the local H content as well as the permeation and release kinetics. For instance, SKP and Scanning Kelvin Probe Force Microscopy (SKPFM) can be combined together to yield quantitative H mapping with high spatial resolution. In a study by Schimo et al.[20] on the Rolling

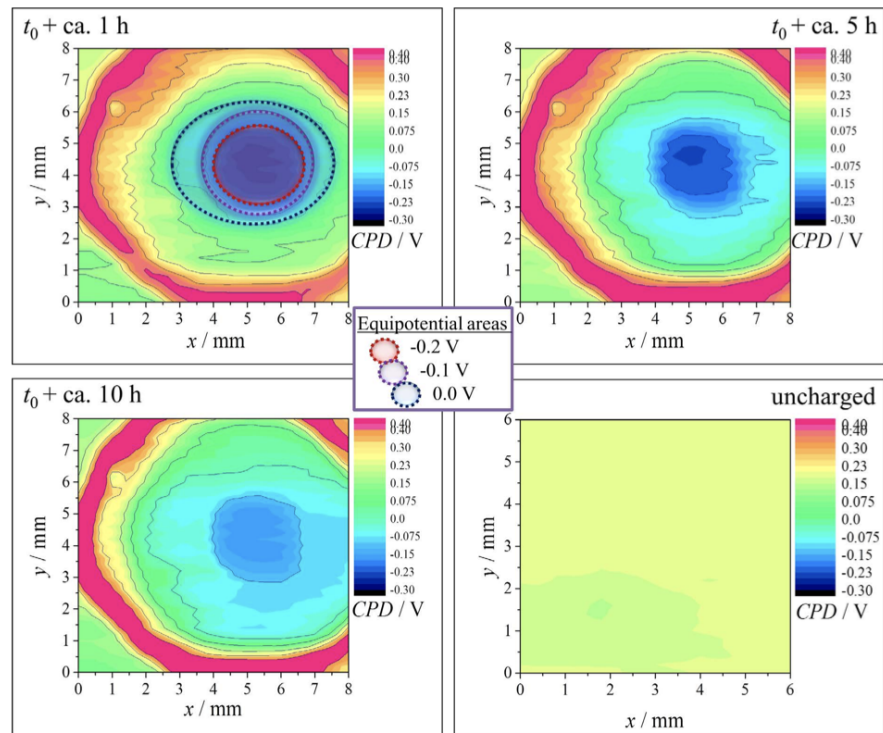


Figure 2.22: Representative SKP potential maps of hydrogen charged surface of ferritic steel after 1, 5 and 10 h as well as uncharged surface with equipotential areas marked for contact potential difference (CPD) values of - 0.2, - 0.1 and 0.0 V (SHE)[20]

Direction Dependent Diffusion Coefficients of Hydrogen in Ferritic Steel by SDCM Charging and SKP Probing, it was found that the SKP mapping indicated a sharp decrease in the Contact Potential Difference (CPD) values in the region where Hydrogen was charged, see figure 2.22. This drop has been reported to be associated to Hydrogen in multiple studies[20, 109, 110, 111, 112]. After electrochemical hydrogen loading and subsequent cathodic polarization of the steel sample, the initial surface oxides are totally converted to iron, influencing the Fermi level alignment. This causes changes in the band structure of the oxides on the metal surface, thereby reflecting as a decrease in the CPD.

2.6 General Discussion of Literature

- There are many factors that affect an electrochemical system involving iron and steels, such as the as the composition of alloying elements, combination

of different solid phases, grains and grain boundaries and defects in the metal matrix, and the electrolytic medium and its properties. The effect of each of these effects individually on the corrosion properties, was found to be difficult to isolate.

- Different growth models exist for the passive layer on steels. Stainless steels and most other steels were found to have oxide layers with a bilayer structure. In dual phase steel, the martensite phase was found to have a thicker oxide layer compared to the oxide layer on ferrite. This was attributed to the martensite having a more reactive surface. It was concluded that in dual phase steels, the passivation behaviour is limited by the partial passivity of the martensite phase.
- H is found to be more soluble in the austenitic phase when compared to the ferrite or martensite phases. The differences in crystal structure and the presence of alloying elements such as Cr and Ni also contribute to this result.
- H diffusion coefficient is higher for BCC metals compared to FCC. Dislocations are major reversible trapping sites in most steels, but have a lower influence on H diffusion compared to irreversible H traps. The diffusion coefficient of the austenite phase is found to be lower than that of the ferrite phase and the martensite phase even though it has higher H solubility than both. Moreover, it was reported that the hydrogen diffusion coefficient for ferrite was higher than martensite. Since the interactions of hydrogen with lattice defects, inclusions and impurities in the crystal matrix are still not fully understood, it is a path for more research to be done. A limited number of literature was compared to understand the effect of H on the passive layer of steels. The presence of an oxide layer is generally said to decrease H adsorption in most steels. Since, there is not much literature to be found on the influence of oxide layer characteristics on H absorption in different steels, there is a possibility for conducting more research.
- There is still a lack of studies done on H cathodic reactions with controlled surface coverage by hydrogen and oxygen. Particularly the influence of H on the microstructure of the surface sites in iron and steels. Such studies are necessary to fully understand the technical limitations of steel alloys.
- Different methods to charge H into metals was looked into, with a focus on cathodic charging methods. Cathodic charging experiments are widely used due to their ease of use compared to other methods of H charging. A limitation of this technique is the non-uniform distribution of H in the sample. A table comparing the different H charging parameters obtained from literature was made. A combination of Potentiostatic H charging and cyclic Voltammetry was found to be useful to detect and quantify H in steels. Different H mapping methods can be used to answer various questions pertaining to H behaviour in steels. These methods can be used alone or in combination with other methods to yield more results.

3

MATERIALS AND METHODOLOGY

This chapter details the materials and the experimental approach used in the study. First of all, the elemental composition of the materials used in the study will be mentioned. The H/material-interaction of Pure Iron, DP steel and MSS was investigated using various analytical techniques, including Open Circuit Potential (OCP), Cyclic Voltammetry (CV), Electrochemical Impedance Spectroscopy (EIS), SKP, and Potentiodynamic polarization. Finally, the microstructural characterization of the materials at different steps of the electrochemical procedure was done using XRD. Choosing the correct experimental methodologies for the thesis work was critical to providing the best evaluation of the research scope. Therefore, the experimental methodologies used in this section are based on the critical experimental approaches utilized by the authors highlighted throughout the literature review.

3.1 Material Composition

For this research, three different types of iron-based materials were used. A cold-rolled sheet of Armco iron was supplied by AK Steel, Netherlands. The sheet with a 2 mm thickness was cut into strips of dimensions approximately equal to 15mm x 15 mm, using the Struers Discotom. Commercial grade AISI 420 martensitic stainless steel was received in the form of a sheet of thickness 3mm, which was then cut into strips of dimensions approximately equal to 15mm x 15 mm, using the Struers Discotom. Dual Phase 1000 (DP1000) was supplied by TATA Steel IJmuiden. As received, 1 mm thick sample strips in 5mm x 10mm were used for the electrochemical experiments, while 15mm x 15mm sample strips were used for the XRD and SKP measurements. Henceforth, the Armco iron will be referred to as pure iron, the Dual-phase steel will be referred to as DP1000, and the martensitic stainless steel will be referred to as AISI 420. The chemical composition of the three materials is presented in tables 3.1, 3.2 and 3.3.

Table 3.1: Chemical composition (wt%) of the pure iron samples.

Chemical composition wt. % (Fe balanced)											
C	Si	Mn	Cr	Ni	Mo	P	N	Cu	S	Sn	Al
0.001	0.003	0.040	0.014	0.012	0.001	0.003	0.0027	0.007	0.0033	0.002	0.004

Table 3.2: Chemical composition (wt%) of the DP1000 samples.

Elemental composition wt. % (Fe balanced)													
C	Si	Mn	Cr	Ni	Mo	P	Cu	V	S	Sn	Ti	Al	Ca
0.141	0.051	2.149	0.576	0.021	0.004	0.013	0.012	0.007	0.014	0.001	0.032	0.041	0.022

Table 3.3: Chemical composition (wt%) of the AISI 420 samples.

Elemental composition wt. % (Fe balanced)																
C	Si	Mn	Cr	Ni	Mo	P	N	Cu	Co	V	S	Sn	Ti	Al	As	Nb
0.385	0.42	0.67	13.77	0.16	0.059	0.022	0.063	0.06	0.015	0.096	0.002	0.008	0.004	0.004	0.003	0.008

3.2 Electrochemical and Corrosion Experiments

Sample Preparation

A length of copper tape was applied to the back of each metal plate in order to link it to the potentiostat's working electrode alligator clip. After which, the samples with the Cu tape stuck to it, were immersed in a Struers ClaroCit epoxy resin and cured for 40 minutes within a pressure vessel at 2 bar pressure. After the epoxy had cured, the samples were ground using 80 to 4000 grit damp SiC sanding paper. The samples were then polished using a Struers DiaDuo-2 fine diamond suspension with particle sizes of 3 μm and 1 μm . After polishing, the samples were ultrasonicated in an Isopropanol bath for 5 minutes and dried with compressed air. These grinding steps were performed to guarantee that the sample surface was free of scratches that may interfere with the uniform corrosion reaction. When there are scratches and breaks on the surface of the sample, a pretty significant corrosion response may develop. Figure 3.1, shows how the sample looked like after the preparation steps.

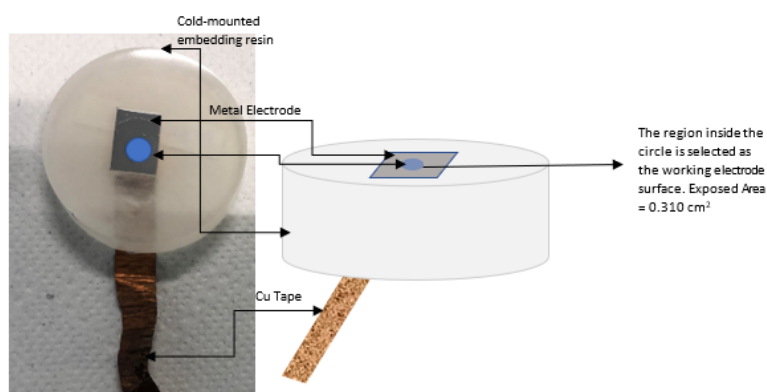


Figure 3.1: Right: A schematic of the cold-mounted sample, Left: Picture of the actual sample. The blue circle on the pictures is just an indication of where the exposed area is on the material.

3.2.1 Experiment to study H/Material Interaction

The test materials must be subjected to a hydrogen-rich environment to explore the H/material interaction. Using a method that can charge hydrogen in such a way that there is a homogeneous distribution of hydrogen across the sample is required to study the interaction of hydrogen with the materials under investigation. There are several methods for charging samples with hydrogen. Hydrogen charging can be accomplished by exposing the sample to either a gaseous hydrogen environment or an aqueous environment in which hydrogen is electrochemically produced. The electrochemical technique allows charging conditions to be changed more accurately and establishes greater hydrogen activity at the sample surface. Furthermore, there is no need for specialized equipment, making it an ideal way to do small-scale research. The electrochemical charging procedure developed by Ozdirik et al.[102] was used as the main guideline for the electrochemical methodology in the present work.

Additionally, to compare the effect of Hydrogen charging and discharging on the active surface and the passive surface of the metals, the experimental process related to H/material interaction was divided into two. This division was based on the pre-conditioning of the metal samples.

3.2.1.1 Experimental Set-up

The electrochemical tests were all carried out with the help of a Biologic VSP-300 potentiostat and the EC-Lab V11.43 software. The experimental setup consisted of a bottom-mounted, three-electrode cell with a reference electrode of Ag/AgCl (saturated KCl) filled with 4M KCl, henceforth called SSC_{sat} in this study. To reduce the impact of contamination, the filling solution was replaced regularly. The potential of the reference electrode was measured before and after each electrochemical experiment, to verify the stability of the reference potential. A platinum wire mesh was used as the counter electrode, and the material surface under investigation functioned as the working electrode. The electrolyte was a 1M NaOH solution containing 8g/L of Thiourea, and the electrolyte was freshly replaced for each test. The pH of this solution was in the range of 13.1-13.7. Additionally, some experiments were done with 1M NaOH only (without the addition of Thiourea) so as to understand the effect of thiourea on Hydrogen adsorption in the materials, but that is not the focus of the study here. Before beginning the electrochemical testing, the setup was enclosed in a Faraday cage to protect it from outside electromagnetic interference. All the experiments were conducted at room temperature. Figure 3.2 depicts the cell setup and a schematic of the three-electrode cell arrangement.

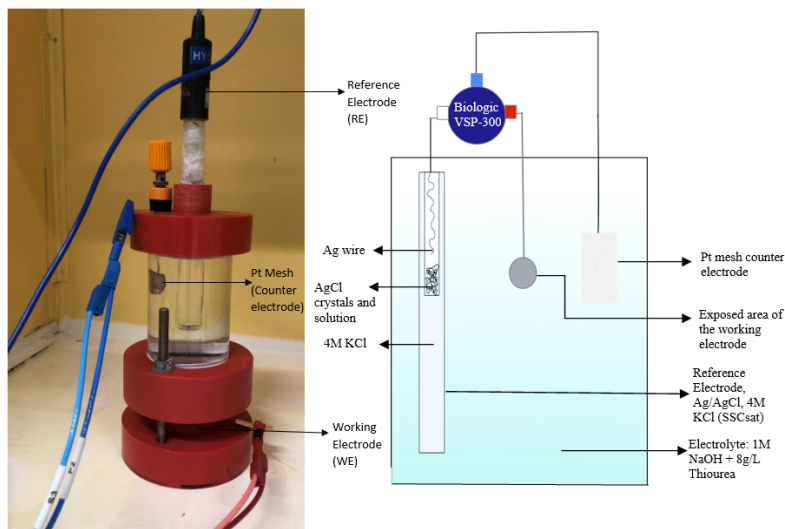


Figure 3.2: Right: A schematic of the three-electrode cell, Left: Picture of the actual set-up used in this experiment, the sample is bottom mounted and clamped between the two bottom plates with a circular area of 0.316 sq.cm diameter being exposed to the electrolyte.

3.2.1.2 Experimental Procedure for H Charging and Discharging on the Active Surface

3.2.1.2.1 Open Circuit Potential

The open circuit potential, or OCP, is determined as the free potential between the working and reference electrodes when there is no net current flowing through the circuit. Typically, the OCP measurement is used as a pre-procedure to track the system state. In this study, the OCP was measured for 1 hour to ensure that the potential stabilizes to a constant value. The OCP is mainly used as a basic step for Electrochemical Impedance Spectroscopy (EIS), but there will also be some observations that can be made from the development of the OCP. The OCP measurement has been performed at least four times and the averages with the error are shown.

3.2.1.2.2 Electrochemical Impedance Spectroscopy

EIS is a non-destructive method for characterizing electrode surfaces and is typically carried out by employing a frequency response analyzer to track the impedance response of working electrode materials. This technique can be used to understand the complex phenomena occurring at the electrode-electrolyte interface. The technique entails periodically applying a small amplitude voltage or current disturbance and monitoring the system's response. The system is typically subjected to an AC signal with an amplitude of 10 – 20 mV, and the current response is recorded. The disturbance moves the system from its current state, followed by relaxation, into a new steady state. Over a broad frequency range of the excitation signal, the system's relaxation process is investigated (10mHz to 10 MHz). Since this technique is performed in-situ, multiple repetitions of measurements of the same electrode-electrolyte system can be implemented.

EIS data can be evaluated by fitting the data to an equivalent electrical circuit. The physical components of the metal/electrolyte interface should be described by the electrical circuit elements.

In this procedure, the EIS was carried out three times: before Hydrogen charging, after Hydrogen charging and after Hydrogen discharging. The first EIS measurement was carried out before the hydrogen charging step, with the samples at OCP to measure the various active electrochemical responses of the three materials of interest. As a result, a baseline for comparison can be established. The second EIS was carried out after hydrogen was charged into the materials. Finally, the third step was carried out after the hydrogen was discharged from the materials. The experimental EIS data were fitted into corresponding electrical circuits using the Zview version 4.0 software.

3.2.1.2.3 Chronoamperometry

Chronoamperometry is an electrochemical method that involves stepping the voltage of the working electrode and measuring the current that results as a function of time. In order to determine the current response and calculate the quantity of charge as a function of time, chronoamperometric curves can be acquired.

In this procedure, the chronoamperometry step is used two times, for hydrogen charging and for hydrogen discharging. It should be noted that the effect of the oxide layer becomes more pronounced with longer charging times, while the amount of thiourea available in the electrolyte decreases. Because of these considerations, the calculation of saturation time was not pursued in this work. Additionally, since the effect of charging duration on some steels has already been discussed in literature^[102], the present study will not compare between different duration times.

For Hydrogen charging: Hydrogen is charged by polarizing the sample cathodically at -1.25 V (vs SSC_{sat}) for 1 hour to have water reduction on the working electrode. The Hydrogen evolved on the working electrode surface can then be absorbed by the surface. For Hydrogen Discharging: Hydrogen is discharged by polarizing the sample cathodically at -0.9 V (vs SSC_{sat}) for 30 minutes to have Hydrogen desorption from the working electrode surface.

3.2.1.2.4 Cyclic Voltammetry

Cyclic Voltammetry (CV) is an electrochemical method that is commonly used to determine the oxidation and reduction processes that can take place in an electrode/electrolyte system within a selected potential window. A potential is applied to the sample within the range of interest and the resulting current response is measured as a function of the applied potential. CV has been used to study the absorption of Hydrogen in steels (refer chapter 2.5.3).

In this study, the CV step was carried out three times: before Hydrogen charging, after Hydrogen charging and after Hydrogen discharging.

Before H charging: Initially, before hydrogen charging, the material was submitted to 3 consecutive CV cycles. The first two CV cycles were done to generate a reproducible sample surface, and the last CV cycle was done to obtain a reference/baseline voltammogram for comparison. After the chronoamperometry hydrogen charging step: 6 consecutive CV scans were carried out. The first CV cycle was used to detect the desorbed Hydrogen, and consecutive CV cycles were carried out to observe the oxidation and reduction state of the metal surface. After the chronoamperometry hydrogen discharging step: 6 consecutive CV scans were carried out. The CV cycles were carried out to observe the oxidation and reduction state of the metal surface after Hydrogen discharging.

To achieve the active surface before the Hydrogen charging and discharging steps, the initial potential (E_i) and the final potential (E_f) for all the CV steps was set to the same value of -1.250 V vs SSC_{sat} ($E_i=E_f$), so as to facilitate the reduction of the oxides formed in the forward cycle of the CV. The samples with the active surface will henceforth be known as samples with pre-conditioning A.

The table 3.4 shows the parameters for all the steps in chronological order. All the tests were repeated at least three times to obtain reproducible data.

Table 3.4: Experimental Procedure for Pre-conditioning A

No.	Step	Parameters
1	Open Circuit Potential (OCP)	Duration : 1 hour
2	Potentiostatic Electrochemical Impedance Spectroscopy (PEIS)	Frequency Range: 50 kHz - 10 mHz Voltage Amplitude: 10mV
3	Cyclic Voltammetry (CV)	Initial Potential (E_i): -1.25 V vs E_{ref} Potential Range ($E_1 - E_2$): $-1.250 - 0.15$ V vs E_{ref} Final Potential (E_f): -1.250 V vs E_{ref} Scan rate: 10 mV/s Number of Cycles (nc): 3
4	Chronoamperometry (CA)	Applied Potential: -1.25 V vs E_{ref} Duration: 1 hour
5	Cyclic Voltammetry (CV)	Initial Potential (E_i): -1.25 V vs E_{ref} Potential Range ($E_1 - E_2$): $-1.250 - 0.15$ V vs E_{ref} Final Potential (E_f): -1.250 V vs E_{ref} Scan rate: 10 mV/s Number of Cycles (nc): 6
6	Open Circuit Potential (OCP)	Duration : 20 minutes
7	Potentiostatic Electrochemical Impedance Spectroscopy (PEIS)	Frequency Range: 50 kHz - 10 mHz Voltage Amplitude: 10mV
8	Chronoamperometry (CA)	Applied Potential: -0.9 V vs E_{ref} Duration: 1 hour
9	Cyclic Voltammetry (CV)	Initial Potential (E_i): -1.25 V vs E_{ref} Potential Range ($E_1 - E_2$): $-1.250 - 0.15$ V vs E_{ref} Final Potential (E_f): -1.250 V vs E_{ref} Scan rate: 10 mV/s Number of Cycles (nc): 6
10	Open Circuit Potential (OCP)	Duration : 20 minutes
11	Potentiostatic Electrochemical Impedance Spectroscopy (PEIS)	Frequency Range: 50 kHz - 10 mHz Voltage Amplitude: 10mV

3.2.1.3 Experimental Procedure for H Charging and Discharging on the Passive Surface

The passive oxide layer of the materials was generated so as to understand the Hydrogen interaction with the passive oxide layer on the materials. This was done using the Cyclic Voltammetry step. The final potential at which the cycle ends was

chosen in the region of passivity as observed from the CV results. This will be shown in the following chapter. The E_f was set as -0.40 V vs SSC_{sat} . The samples with the Passive surface will henceforth be known as samples with pre-conditioning B.

The table 3.5 shows the parameters for just the changed CV steps. All the other steps and parameters are the same as that for pre-conditioning A. All the tests were repeated at least three times to obtain reproducible data.

Table 3.5: Experimental Procedure for H Charging and Discharging on on the Passive Surface

No.	Step	Parameters
3	Cyclic Voltammetry (CV)	Initial Potential (Ei): -1.25 V vs Eref Potential Range (E1 - E2): $-1.250 - 0.15$ V vs Eref Final Potential (Ef): -0.4 V vs Eref Scan rate: 10 mV/s Number of Cycles (nc): 3
5	Cyclic Voltammetry (CV)	Initial Potential (Ei): -1.25 V vs Eref Potential Range (E1 - E2): $-1.250 - 0.15$ V vs Eref Final Potential (Ef): -0.4 V vs Eref Scan rate: 10 mV/s Number of Cycles (nc): 6
9	Cyclic Voltammetry (CV)	Initial Potential (Ei): -1.25 V vs Eref Potential Range (E1 - E2): $-1.250 - 0.15$ V vs Eref Final Potential (Ef): -0.4 V vs Eref Scan rate: 10 mV/s Number of Cycles (nc): 6

3.2.2 Experiment to study the impact of Hydrogen charging and discharging on the corrosion properties of the materials

Sea-water is one of the earth's most abundant and common corrosive agents. Researchers usually use $3.5\text{wt}\%$ NaCl to simulate seawater conditions. Hence understanding the impact that hydrogen charging and discharging can have on the corrosion properties of iron-based alloys when exposed to $3.5\text{wt}\%$ NaCl solution is crucial.

3.2.2.1 Experimental Set-up

The same three-electrode Electrochemical cell setup as mentioned in the previous experiments is used here. The electrolytes used were 1M NaOH solution containing 8g/L of Thiourea and $3.5\text{wt}\%$ NaCl solution, and the electrolytes were freshly replaced for each test. The pH of this solution was in the range of $13.1-13.7$ for the 1 M NaOH + 8g/L Thiourea solution and $6.1-6.7$ for the $3.5\text{wt}\%$ NaCl solution. All the other operating parameters are the same as the previous Electrochemical experiments.

3.2.2.2 Experimental Procedure

The experiment was divided into two parts. For the first part, the corrosion properties of the materials in the $3.5\text{wt}\%$ NaCl electrolyte were characterized using OCP and Potentiodynamic Polarization tests. For the second part, the materials were first charged and discharged with hydrogen using the chronoamperometry method in the 1 M NaOH + 8g/L Thiourea electrolyte; then, the electrolyte was removed and replaced with the $3.5\text{wt}\%$ NaCl electrolyte. After which OCP and Potentiodynamic

Polarization tests were conducted. The first part is used to generate a reference for comparison with the results from the second part. In addition, it should explain how the material corrosion properties in 3.5wt%NaCl solution change before and after hydrogen charging and discharging. Table 3.6 shows the parameters and the tests for the part 1 in chronological order.

Table 3.6: Experimental Procedure for part 1 - electrochemical characterization in NaCl electrolyte before Hydrogen charging

No.	Step	Parameters
1	Open Circuit Potential (OCP)	Duration: 1 hour Scan Rate: 0.166 mV/s
2	Potentiodynamic Polarisation	Initial Potential (Ei): -0.300 vs Eocp Final Potential (Ef): -0.400 vs Eocp

Table 3.7 shows the parameters and the tests for the part 2 in chronological order.

Table 3.7: Experimental Procedure for part 2 - electrochemical characterization in NaCl electrolyte after Hydrogen charging and discharging

No.	Electrolyte	Step	Parameters
1	1 M NaOH + 8 g/L Thiourea	Open Circuit Potential (OCP)	Duration: 1 hour
2	1 M NaOH + 8 g/L Thiourea	Chronoamperometry (CA)	Applied Potential: -1.250 V vs Eref Duration: 1 hour
3	1 M NaOH + 8 g/L Thiourea	Chronoamperometry (CA)	Applied Potential: -0.900 V vs Eref Duration: 30 mins
4	3.5wt% NaCl	Open Circuit Potential (OCP)	Duration: 1 hour Scan Rate: 0.166 mV/s
5	3.5wt% NaCl	Potentiodynamic Polarisation	Initial Potential (Ei): -0.300 vs Eocp Final Potential (Ef): -0.400 vs Eocp

3.2.3 Scanning Kelvin Probe (SKP)

The SKP is a non-contact, non-destructive vibrating capacitor device that measures the difference in work function between a vibrating tip and a conductive sample or the surface potential of semiconducting or insulating surfaces[113]. The minimum amount of energy required to remove an electron from an atom's outer shell is known as the work function. This value is a very good predictor of the sample's surface condition. A parallel plate capacitor is created by the surface under investigation and the vibrating tip. This happens when two distinct materials, usually metals, come into electrical contact, a flow of charge between the two materials takes place to balance their Fermi levels. This equilibration produces a potential difference that causes the materials to develop a surface[21]. Figure 3.3 shows the evolution of the Fermi level and the charging of the probe and sample. The electrochemical potential of the electrons in both metals will be equal when two metals (the probe and the sample) are linked. Due to this, one of the metals becomes more charged than the other, which causes a potential difference between the two metals in contact. This difference is known as the Volta potential difference or contact potential difference. Thus, by measuring the Volta potential difference in relation to a reference metal with a constant reference work function, the work function of a metal can be determined. In a paper by Stratmann et al.[114] it is shown that the contact potential difference of a metal is related to the corrosion potential measured by a micro reference electrode.

In this study, Scanning Kelvin probe measurements were conducted to investigate the H/material interaction for the iron-based alloys under study. The Volta potential distribution across the sample area of interest is measured using scanning Kelvin probe (SKP) in a humidity control chamber. The SKP technique is used two times for

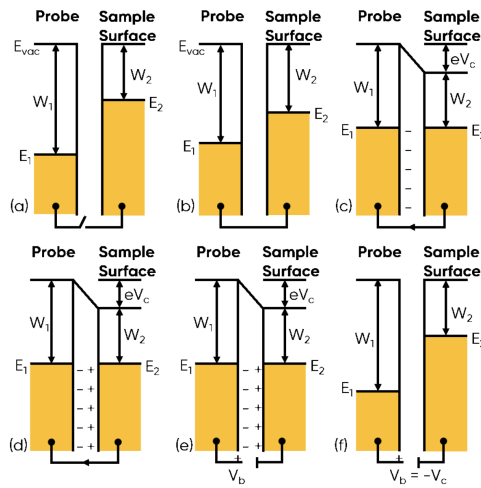


Figure 3.3: When there is no electrical connection between the probe and the sample, each has a unique Fermi level E_{xp} and work function W_{xp} . Since the probe and sample are electrically linked during an SKP measurement (b), charge flows from the sample to the probe (c). As a result, a surface charge known as the contact potential difference V_{cp} is created between the probe and sample. In SKP, a backup potential V_b is provided between the probe and the sample (e) to null the surface charge and restore the Fermi levels to their initial positions. This potential is equal to the contact potential difference but has the opposite sign.[21]

each material; before hydrogen charging (on the bare metal surface after polishing) and after hydrogen charging.

- Before Hydrogen charging - A freshly polished sample of the three materials was used for the SKP experiment.
- After Hydrogen Charging - A freshly polished sample was electrochemically charged with hydrogen and then used for the SKP experiment. To note: the SKP tests were done within an 10 mins after charging with hydrogen.

3.2.3.1 Sample Preparation

The following steps were used to prepare the samples for Scanning Kelvin probe (SKP) measurements. The as-received three materials, Pure Iron, DP1000 and AISI 420 were cut into strips of dimensions approximately equal to 15mm x 15 mm, using the Struers Discotom. The samples were ground using 80 to 4000 grit damp SiC sanding paper. The samples were then polished using a Struers DiaDuo-2 fine diamond suspension with particle sizes of 3 μm and 1 μm .

Electrochemical experimental Set-up and Procedure for sample preparation

The same three-electrode Electrochemical cell setup as mentioned in the H-Charging experiments is used here. The electrolyte was a 1M NaOH solution containing 8g/L of Thiourea, and the electrolyte was freshly replaced for each test. All the other operating parameters are also the same as the previous Electrochemical experiments. For the samples After Hydrogen charging used for the SKP tests, the electrochemical procedure used is detailed in the table 3.8.

Table 3.8: Electrochemical sample preparation for SKP - After Hydrogen Charging

No.	Step	Parameters
1	Open Circuit Potential	Duration: 1 hour
2	Chronoamperometry (CA)	Applied Potential: -1.250 V vs Eref Duration: 1 hour

The samples before hydrogen charging and the samples obtained after hydrogen charging were gently washed with Isopropanol and dried with compressed air. Following sample preparation, potential measurements were carried out using a height-regulated scanning Kelvin probe (SKP5050) from KM Soft Control. The SAE 304 stainless steel tip of the SKP probe has a diameter of around 550 μm . The probe was calibrated against a Cu/CuSO_4 reference prior to the experiments. All the tests were carried out at room temperature (23 $^{\circ}\text{C}$), with a relative humidity of approx. 53 percent. The figure 3.4 shows a schematic of the SKP sample (in grey), the area charged with Hydrogen (in yellow) and the area of interest (in blue).

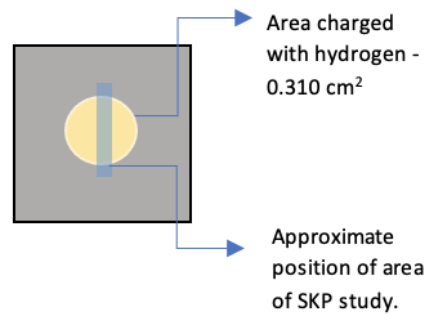


Figure 3.4: A schematic of the SKP sample and the area of interest.

Table 3.9 shows the SKP parameters set for the line scans.

Table 3.9: SKP Parameters

No.	SKP Parameters	Values
1	Gradient Required	123 +/- 6
2	Probe Amplitude	40
3	No. of Lines	4
4	Area scan (x)	508 μm
5	Area scan (y)	1.02 cm
6	x step	254 μm
7	y step	254 μm

3.3 Microstructure Characterization

3.3.1 X-Ray Diffraction (XRD)

XRD is a powerful, non-destructive analytical technique that can be used to ascertain the atomic and molecular structure of crystalline and semi-crystalline materials. X-rays produced in a cathode ray tube are fired at a sample while being accelerated by a voltage. A portion of the energy is absorbed by electrons in the sample, and as excitation takes place, inner shell electrons are knocked loose and generate a distinctive X-ray spectrum. The spectra generated are identified using an existing database, and they show the crystalline phases present in the sample material, providing information on the chemical composition. Crystalline and semi-crystalline materials have distinct diffraction patterns that they produce. Additionally, data on average particle size, structures, phase ratios, crystallinity, stress states, and crystal defects can be obtained.

The scattering phenomenon is represented by Bragg's law, where n is an integer, λ is the x-ray wavelength, d is the distance between planes in the sample's atomic lattice, and θ is the diffraction angle in degrees. Bragg's law is represented by the equation given below.

$$n\lambda = 2d\sin\theta$$

In this thesis, XRD is used to characterize the three materials under study to gain a better understanding of its surface microstructure. The XRD technique is used three times for each material; before hydrogen charging (on the bare metal surface after polishing), after hydrogen charging and after hydrogen discharging. The instrument used and the relevant settings and measurements made are shown in table 3.10. The XRD technique was used at three different stages of the Hydrogen charging and discharging process. For the case of XRD, the samples were extracted from three different stages of the process detailed in table 3.4:

- Before Hydrogen charging - A freshly polished sample of the three materials was given for the XRD characterization
- After Hydrogen Charging - A freshly polished sample was electrochemically charged with hydrogen and then given for XRD characterization. To note: the XRD tests were done within an hour after charging with hydrogen.
- After H discharging - A freshly polished sample was electrochemically charged and discharged with hydrogen after which it was given for XRD characterization.

Table 3.10: XRD Instrument specifications and parameters

Sample taken at which stage	Before Hydrogen Charging	After Hydrogen Charging and After Hydrogen Discharging
Instrument	Bruker D8 Discover diffractometer and Eiger-2 500k 2D-detector. Incoatec Microfocus Source (1 μ S)	Bruker D8 Discover diffractometer and Eiger-2 500k 2D-detector. Incoatec Microfocus Source (1 μ S)
Emission source	Cu K α radiation, 50 kV 1000 μ A.	Cu K α radiation, 50 kV 1000 μ A.
Measurement	Continuous θ -2 θ scan 10 $^\circ$ - 110 $^\circ$, step size 0.020 $^\circ$ 2 θ , counting time per step 5s.	Continuous θ -2 θ scan 10 $^\circ$ - 110 $^\circ$, step size 0.04 $^\circ$ 2 θ , counting time per step 2s, 10s. Continuous θ -2 θ scan 20 $^\circ$ - 80 $^\circ$, step size 0.04 $^\circ$ 2 θ , counting time per step 10 s. First a relatively quick measurement with step time 2s was done, immediately after the charging treatment. After that a slower measurement with a smaller 2theta range was performed with step time of 10 s, to resolve small peaks. After discharging only a full range slow measurement was needed.
Data Evaluation	Bruker software DiffracSuite.EVA vs 6.0.	Bruker software DiffracSuite.EVA vs 6.0.

3.3.1.1 Sample Preparation

The as-received three materials, Pure Iron, DP1000 and AISI 420 were cut into strips of dimensions approximately equal to 15mm x 15 mm, using the Struers Discotom. The samples were ground using 80 to 4000 grit damp SiC sanding paper. The samples were then polished using a Struers DiaDuo-2 fine diamond suspension with particle sizes of 3 μ m and 1 μ m. After polishing, the samples were ultrasonicated in an Isopropanol bath for 5 minutes and dried with compressed air. These grinding steps were performed to guarantee that the sample surface was free of scratches.

Electrochemical Experiment Set-up for sample preparation

The same three-electrode Electrochemical cell setup as mentioned in the H-Charging experiments is used here. The electrolyte was a 1M NaOH solution containing 8g/L of Thiourea, and the electrolyte was freshly replaced for each test. All the other operating parameters are also the same as the previous Electrochemical experiments.

Table 3.11: Electrochemical sample preparation for XRD - After Hydrogen Charging

No.	Step	Parameters
1	Open Circuit Potential (OCP)	Duration: 1 hour
2	Cyclic Voltammetry (CV)	Initial Potential (E _i): -1.250 V vs E _{ref} Potential Range (E ₁ - E ₂): -1.250 - 0.15 V vs E _{ref} Final Potential (E _f): - 0.4 V vs E _{ref} Scan rate: 10 mV/s No. of cycles: 3
3	Chronoamperometry (CA)	Applied Potential: -1.25 V vs E _{ref} Duration: 1 hour

For the samples After Hydrogen charging used for the XRD test, the electrochemical procedure used is detailed in the table 3.11.

For the samples After Hydrogen Discharging used for the XRD test, the electrochemical procedure used is detailed in the table 3.12.

Table 3.12: Electrochemical sample preparation for XRD - After Hydrogen Discharging

No.	Step	Parameters
1	Open Circuit Potential (OCP)	Duration: 1 hour
2	Cyclic Voltammetry (CV)	Initial Potential (E _i): -1.250 V vs E _{ref} Potential Range (E ₁ - E ₂): -1.250 - 0.15 V vs E _{ref} Final Potential (E _f): - 0.4 V vs E _{ref} Scan rate: 10 mV/s No. of cycles: 3
3	Chronoamperometry (CA)	Applied Potential: -1.25 V vs E _{ref} Duration: 1 hour
4	Cyclic Voltammetry (CV)	Initial Potential (E _i): -1.250 V vs E _{ref} Potential Range (E ₁ - E ₂): -1.250 - 0.15 V vs E _{ref} Final Potential (E _f): - 0.4 V vs E _{ref} Scan rate: 10 mV/s No. of cycles: 5
5	Chronoamperometry (CA)	Applied Potential: -0.90 V vs E _{ref} Duration: 30 minutes

4 | RESULTS

4.1 Microstructure Characterization - XRD

The microstructural characterization of the metals in this study was performed through XRD analyses. The samples for this analysis was taken from three different stages of the Hydrogen charging and discharging process as mentioned in section 3.3.1.

4.1.1 Before Hydrogen Charging

Pure Iron is generally said to be composed of ferrite (α -Ferrite, BCC). In an earlier study by Kar et al.[115] the same Pure Iron material was characterised using optical microscopy. It was found that the samples have a single ferrite phase. This can be confirmed from the XRD diffractogram seen in figure 4.1. All the major diffraction peaks can be associated to the α -Ferrite phase.

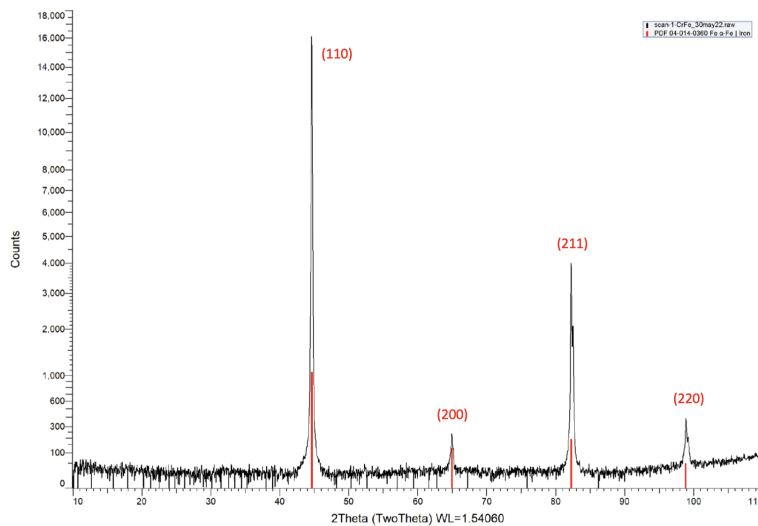


Figure 4.1: X-Ray Diffraction peaks of Pure Iron Before Hydrogen charging (Peak fitting with the red lines - α -Fe).

Dual-phase (DP) steels are typically composed of ferrite and 5-20% martensite and including some retained austenite, with yield strengths ranging from 500 to 1200 MPa. In an earlier study by Ozkan et al.[116] the same DP1000 material was characterised using optical microscopy and SEM. It was found that the material had a ferrite-martensite microstructure with a ferrite volume fraction of 50%. This can be confirmed from the XRD diffractogram for Dual Phase 1000 steel which shown in figure 4.2. The most contributing peaks relate to the α -Fe(BCC ferrite/BCT martensite). However, there are also a few minor contributing peaks associated with the γ -Fe (FCC retained austenite) phase that were found. XRD distinguishes various crystallographic modifications of iron (α -Fe, γ -Fe). It cannot, however, clearly distinguish between ferrite and martensite. As a result of the investigated steels' low carbon content, it was predicted that martensite would have a roughly cubic structure comparable to ferrite rather than a tetragonal structure[117].

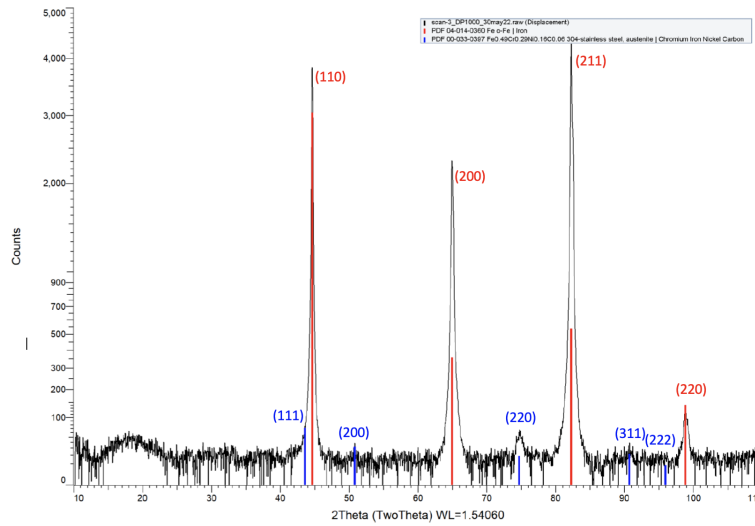


Figure 4.2: X-Ray Diffraction peaks of DP1000 Before Hydrogen charging (Peak fitting with the red lines - α -Fe and Peak fitting with the blue lines - γ -Fe).

The XRD diffractogram in Figure 4.3 reveals that martensite makes up the majority of the AISI 420 material. Additionally, a few minor secondary carbide peaks can be detected. In an earlier research by Crousen et al.[118] on the same material, using microscopy techniques, it was found that the microstructure was clearly dominated by martensite laths. Retained austenite was, however, not easily distinguished in optical microscopy. There were no distinguishable retained austenite peaks in the XRD diffractogram in figure 4.3 either.

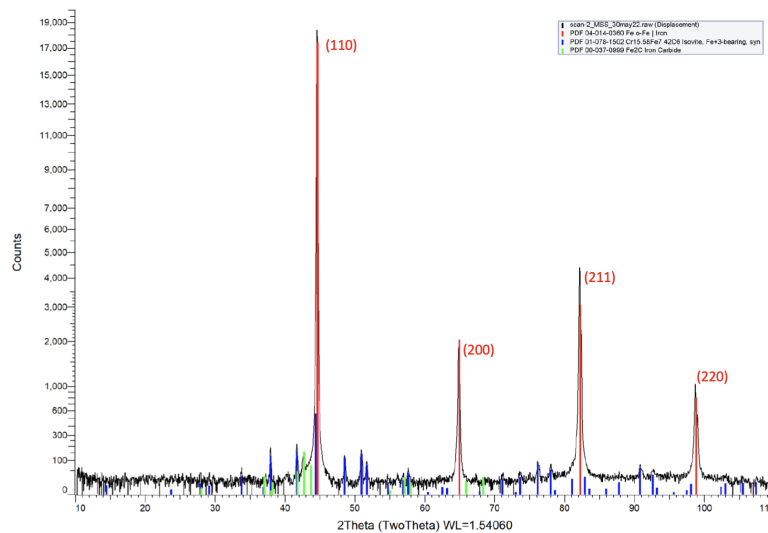


Figure 4.3: X-Ray Diffraction peaks of AISI 420 Before Hydrogen charging (Peak fitting with the red lines - α -Fe (BCT martensite)).

The table 4.1 shows the possibly present crystalline phases in the materials before H charging.

Table 4.1: The table shows the possibly present crystalline phases in the materials before H charging, using the ICDD pdf4 database. The color sticks mentioned correspond to the colored fitting lines in the XRDs.

Material	Compound	Values
Pure Iron	α -Iron	Fe (red sticks)
	α -Iron	Fe (red sticks)
	Isovite	Cr _{15.58} Fe _{7.42} C ₆ (blue sticks)
AISI 420	Iron Carbide	Fe ₂ C (Green sticks)
	α -Iron	Fe (red sticks)
DP1000	Austenite	Fe _{0.49} Cr _{0.29} Ni _{0.16} Co _{0.06} (blue sticks)

4.1.2 After Hydrogen Charging and After Hydrogen Discharging

For the pure iron samples after H charging and after H discharging, the XRD diffractogram in figure 4.4 showed peaks with respect to the α -Fe peaks (BCC Ferrite) phase, and there were some additional peaks related to Ferroxyhyte (FeO(OH)) phase. Similarly, for the DP1000 samples after H charging and after H discharging,

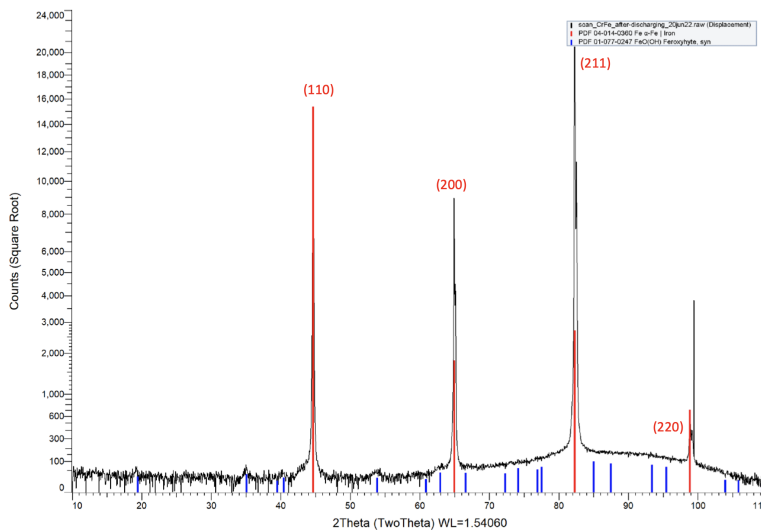


Figure 4.4: X-Ray Diffraction peaks of Pure Iron After Hydrogen (dis)charging (Peak fitting with the red lines - α -Fe (BCC Ferrite), Peak fitting with the blue lines - Ferroxyhyte (FeO(OH))).

the XRD diffractogram in figure 4.5 showed peaks with respect to the α -Fe (BCC ferrite/BCT martensite) phase and the γ -Fe (FCC retained austenite) phase, and there were some additional peaks related to Ferroxyhyte (FeO(OH)). Now, the XRD diffractogram for the AISI 420 material After H (dis)charging did not show any differences with respect to the appearance of new phases in comparison with the XRD from before H charging. The table 4.2 shows the possibly present crystalline phases after H charging and H discharging.

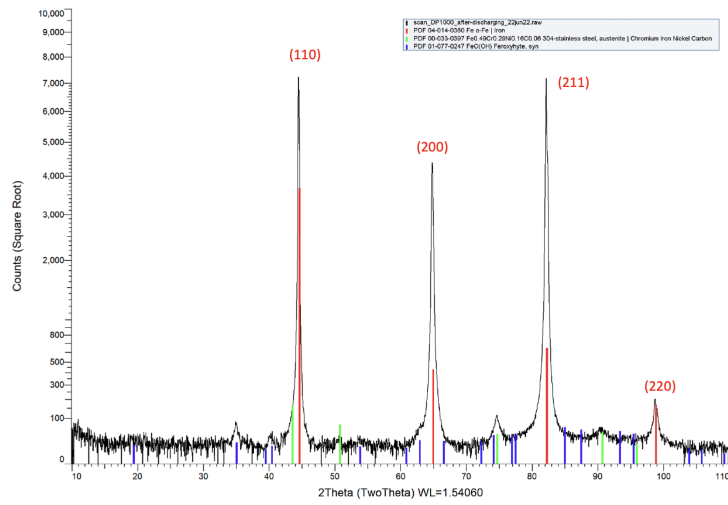


Figure 4.5: X-Ray Diffraction peaks of DP1000 After Hydrogen (dis)charging (Peak fitting with the red lines - α -Fe (BCC Ferrite/ BCT Martensite), Peak fitting with the blue lines - Feroxyhyte (FeO(OH), Peak fitting with the green lines - γ -Fe).

Table 4.2: The table shows the possibly present crystalline phases after H charging and H discharging, using the ICDD pdf4 database.

Material	Compound	Values
Pure Iron	α -Iron	Fe
+ After H Charging	Feroxyhyte	FeO(OH)
+ After H Discharging	Feroxyhyte	FeO(OH)
AISI 420	α -Iron	Fe
	Isovite	Cr _{15.58} Fe _{7.42} C ₆
	Iron Carbide	Fe ₂ C
+ After H Charging	-	-
+ After H Discharging	-	-
DP1000	α -Iron	Fe
	Austenite	Fe _{0.49} Cr _{0.29} Ni _{0.16} Co _{0.06}
+ After H Charging	Feroxyhyte	FeO(OH)
+ After H Discharging	Feroxyhyte	FeO(OH)

4.2 H/material interaction - Electrochemical Experiments

4.2.1 Pourbaix Diagram

The electrochemical stability of an element in various redox states is plotted as a function of pH on Pourbaix Diagrams. These diagrams, as previously mentioned, are essentially phase diagrams that depict the potential and pH conditions (usually in aqueous solutions) at which certain redox species are stable. When identifying the peaks in the cyclic voltammograms of materials in electrolytes of varying pH, a Pourbaix diagram is a very useful tool. Pourbaix diagrams in the relevant area of interest need to be analyzed for this reason. For the understanding the electrochemical processes alongside the potential range studied (-1.25 V to 0.15 V vs. Ag/AgCl(sat-KCl)), figure 4.6 depicts the Pourbaix diagram for iron. Iron is stable up to a potential of -1 V versus SHE at a pH range of 13.1 - 13.7. Increasing the potential to more positive values causes iron to oxidize to FeO, Fe₃O₄, and Fe₂O₃. Around -0.65 V (-0.85 V vs Ag/AgCl), Fe oxidizes to Fe₂O₃. The lower orange dashed line represents the lower limit of water stability (LLW), below which hydrogen liberation begins. This corresponds to a potential of roughly -0.7 V (-0.9 V vs SSCsat) in the pH range of interest in the Pourbaix diagram in figure 4.6. Due to experimental inconsistencies, all the values read from the pourbaix diagrams when converted into real values have to be considered with a degree of flexibility.

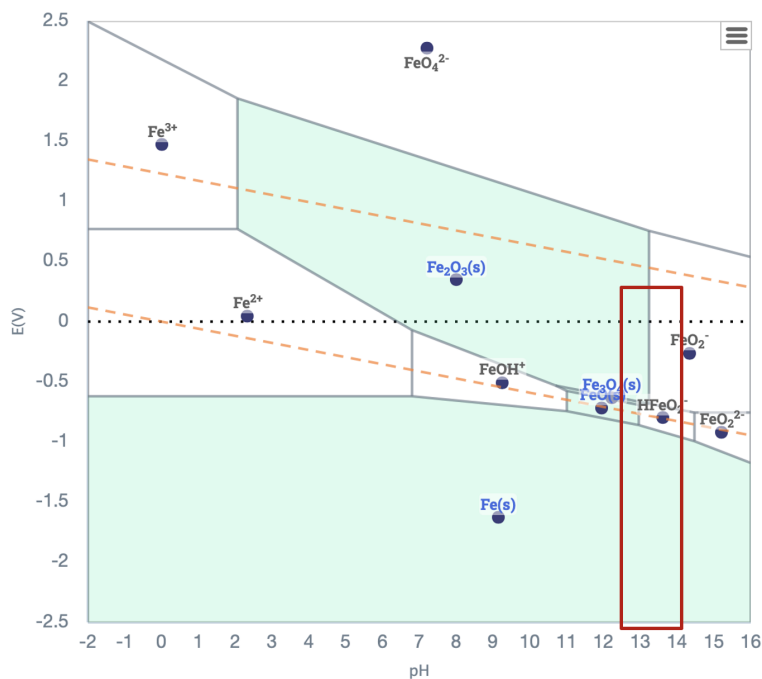


Figure 4.6: Pourbaix diagram of iron. The red rectangle marks the pH range of the electrolyte used in this study and the lower dashed orange line represent the stability region of water. The filled regions in the diagram indicate a solid phase whereas empty regions indicate dissolution of Fe ions.

The Pourbaix diagram of an Fe(87%)-Cr(13%) alloy resembling the composition ratio (in weight) of AISI 420 stainless steel, if no other alloying elements were present, is shown in Figure 4.7. Only Iron and chromium were considered since they have the highest weight percentage with respect to all the other elements composing the AISI 420 stainless steel. In the pH region of interest, from 13.1-13.7, until approx. -1.5 V vs SHE, Fe(s) and Cr(s) are stable after which the Fe(s) is stable until

-1 V vs SHE. Increasing to higher concentrations causes the Cr and Fe to oxidize to Cr_2O_3 , FeO , Fe_3O_4 , FeO_2^- , combined oxides of Fe and Cr, etc. The lower orange dashed line represents the lower limit of water stability (LLW), below which hydrogen liberation begins. This corresponds to a potential of roughly -0.7 V (-0.9 V vs SSCsat) in the pH range of interest in the Pourbaix diagram in figure 4.6. Due to experimental inconsistencies, all the values read from the pourbaix diagrams when converted into real values have to be considered with a degree of flexibility.

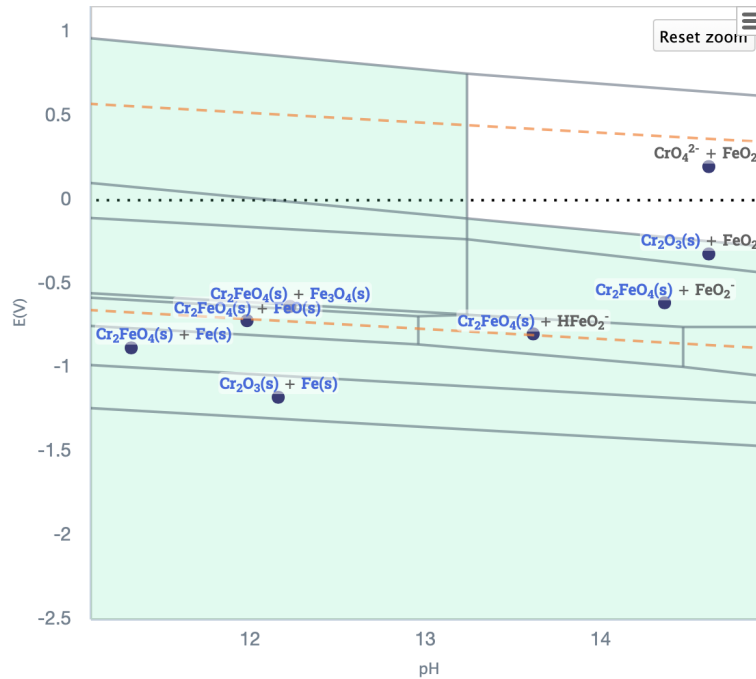


Figure 4.7: Pourbaix diagram of Fe 87% Cr 13% system. The lower dashed orange line represent the stability region of water. The filled regions in the diagram indicate a solid phase whereas empty regions indicate dissolution of Fe and Cr ions.

4.2.2 Determination of Operating Parameters

Sodium Hydroxide(NaOH) was chosen as the electrolyte for all the H charging experiments so as to compare hydrogen sorption properties in passivity conditions. Thiourea was used as a recombination poison to promote the absorption of H into the material surface by preventing the recombination of H^+ ions to H_2 gas. Initially, some tests were done using 0.1 M NaOH and 8 g/L of thiourea, but the results did not show distinguishable peaks with respect to Hydrogen desorption. Therefore, based on the study by Ozdirk et al.[102], a concentration of 1 M NaOH and 8 g/L of Thiourea (TU) was used as the electrolyte. Additionally some tests were also done without the addition of Thiourea i.e. with 1 M NaOH alone, as the electrolyte, so as to identify if the addition of Thiourea was necessary. The choice of potential for H charging and discharging was on the basis of the Pourbaix Diagram for Iron and steel systems and the literature study. This will be expanded upon later.

4.2.3 OCP Measurements

The figure 4.8 presents the OCP measurements that have have stabilised after 1 hour for the 4 active materials. The figure shows the results of a single repetition of each sample. It is crucial to note that a single repetition for the OCP value

will not provide a reliable indicator of the typical behavior of the sample under consideration. However, in this case, this representative OCP plot shows the general trend as observed from all the repetitions. It shows that the AISI 420 material has the most negative potential. This might be due to the continuous passivisation of the steel in the alkaline medium. Additionally, the presence of thiourea might also have an effect on the OCP value.

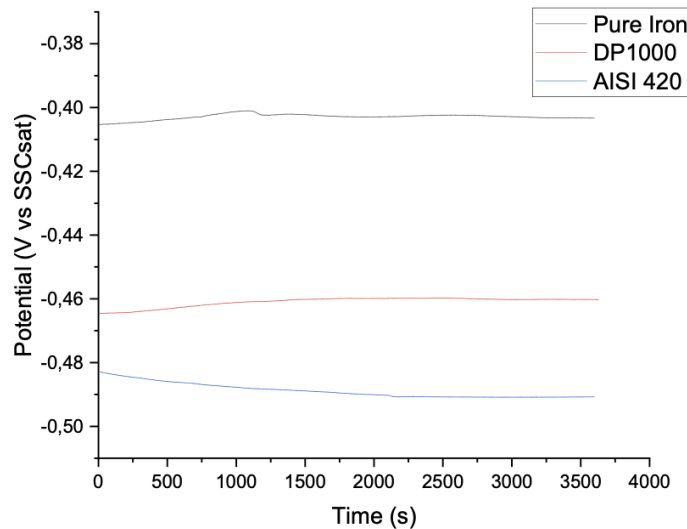


Figure 4.8: OCP values for DP1000, Pure Iron and AISI 420 in 1 M NaOH + 8 g/L Thiourea

The table 4.3 shows the OCP values of the three materials under study in the 1 M NaOH + 8 g/L Thiourea electrolyte.

Table 4.3: OCP values of the three materials under study in the 1 M NaOH + 8 g/L Thiourea electrolyte. The OCP measurement has been performed at least four times and the averages with the error are shown.

Electrolyte	Material	OCP (V vs SSC_{sat})
1 M NaOH + 8 g/L Thiourea	DP1000	-0.404 ± 0.012
	Pure Iron	-0.392 ± 0.010
	AISI 420	-0.506 ± 0.020

4.2.4 Hydrogen Charging and Discharging Curves

Figures 4.9 and 4.10 show the chronoamperometric charging and discharging curves for DP1000 in 1 M NaOH + 8 g/L Thiourea electrolyte. Both figures show stable curves that indicate that there is no H_2 bubbling in the Electrochemical cell setup, that might show up as perturbations in the I vs t curve. The CA curves for charging and discharging have a similar profile across the three materials and for both active and passive behaviour. Therefore, the CA curves for H charging and Discharging in DP1000 is used as a representation here.

The Cyclic Voltammetry and the EIS results will be presented in detail in the next section.

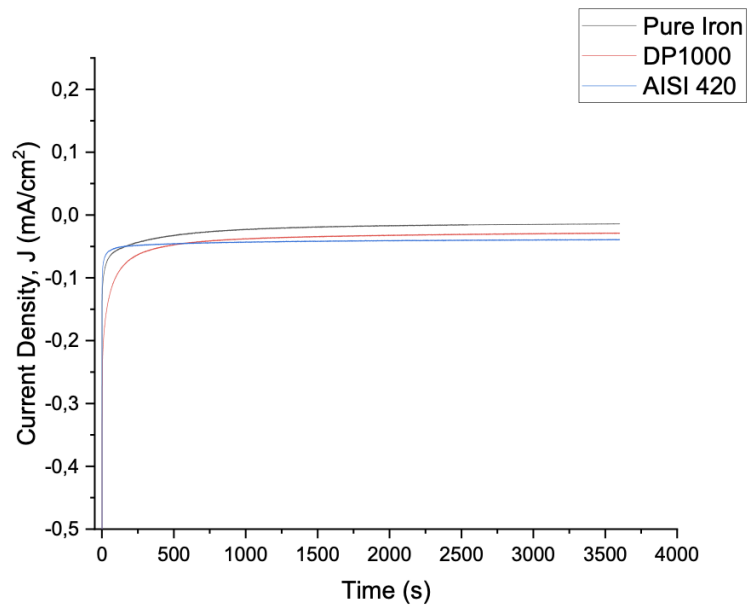


Figure 4.9: CA curve for H charging at a constant potential of -1.25 V vs SSCsat for DP1000 in 1 M NaOH + 8 g/L Thiourea

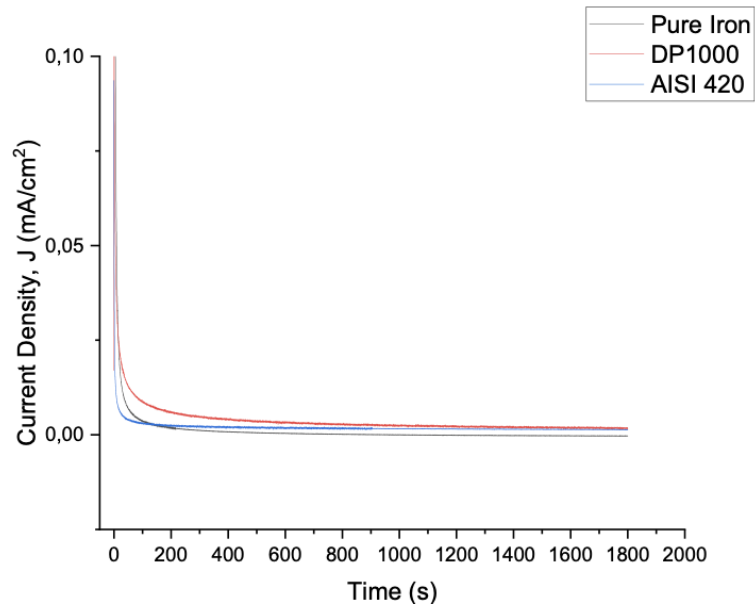


Figure 4.10: CA curve for H discharging at a constant potential of -0.90 V vs SSCsat for DP1000 in 1 M NaOH + 8 g/L Thiourea

4.3 H/material interaction - Electrochemical Experiments - Cyclic Voltammetry

4.3.1 Active Behaviour (Pre-conditioning A) - Attribution of Peaks

4.3.1.1 DP1000

Figure 4.11a shows the voltammograms obtained for the CV scan prior to hydrogen charging for the DP1000 sample. Three consecutive CV cycles are performed on the steel as pre-treatment before hydrogen charging. Three anodic and two cathodic responses are observed in the voltammogram. Peak a1 decreases with cycling, while peak a2 and peak c1 grow.

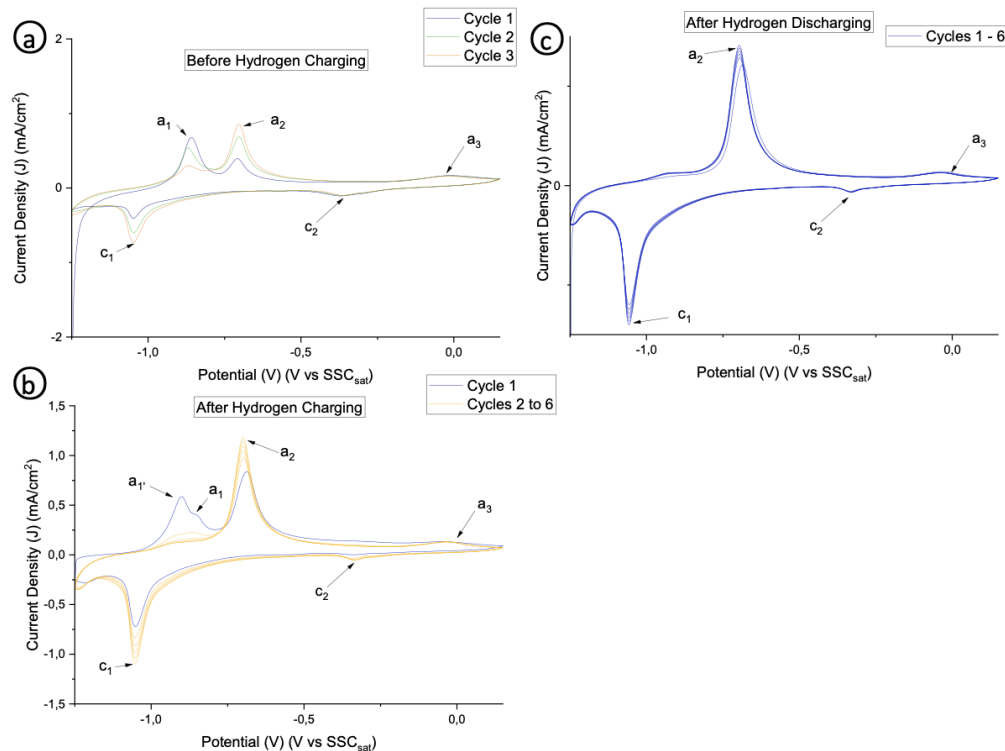
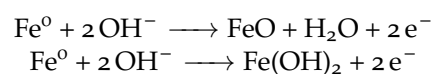


Figure 4.11: Overview of the procedure for cyclic voltammetry, DP1000 (a) three CV scans before hydrogen charging, (b) six CV scans after 1 hour of hydrogen charging and (c) six CV scans after 30 mins of hydrogen discharging in 1 M NaOH solution containing 8 g/l thiourea solution (scan rate 10 mV/s).

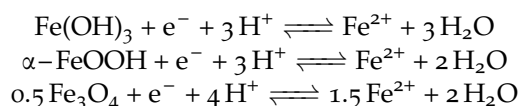
During the forward scan (oxidation process), which starts at a potential $E_i = -1.25$ V vs SSC_{sat} and increases in a positive direction, there appears to be a peak at a₁, as indicated in the figure 4.11a. For the anodic peak at a₁, it can be seen that an accompanying reduction peak does not appear in the reverse scan which is an indication that an irreversible oxidation process is taking place. Either of the two following reactions can take place,



As the potential becomes more positive, an anodic peak appears at a₂ followed by a peak at a₃. The CV scan switches to the reverse sweep at a potential $E_2 = 0.15$ V vs SSC. In the reverse scan (Reduction process, as the potential becomes more

negative, a cathodic peak appears at c2 followed by a peak at c1. However, an accompanying reduction peak does not appear in the reverse scan, indicating an irreversible oxidation process. Additionally, the colour of the sample turns orange-brown during the forward anodic scan, while the colour diminishes after the reverse cathodic scan.

The integration of the peaks at a2 and c1 shows that the amount of charge released is similar. The standard potential of this reaction was calculated, and based on the pourbaix diagram in the figure 4.6 and Literature[102, 37, 119, 120], the peaks are generally attributed to (hydr)oxidation/reduction reactions. The following reactions can take place, as to which exact reaction is taking place will be discussed in the next chapter.

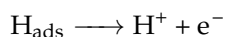


Similarly, the integration of the peaks at a3 and c2 shows that the amount of charge released is similar. From literature[121], it can be assumed that the peaks at a3 and c2 can be assigned to the redox system $\text{Mn}_3\text{O}_4/\text{Mn}_2\text{O}_3$. This agrees with the composition of the dual phase steel. As these processes are not the focus of the presented work, they will not be discussed further.

Then, in the potential region between approx -0.200V to -0.600 V vs SSCsat, the current response is more or less constant, showing the passivity of the surface due to the formation of oxide layers.

Figure 4.11b shows six consecutive voltammograms taken after hydrogen charging. For the scanning conditions mentioned earlier, the first anodic response in the first CV scan contains four peaks a1', a1, a2 and a3. In the second CV cycle, peak a1' is highly diminished and only the other three anodic peaks remain, showing a decreasing trend from the first to the second cycle. From the third cycle on, peak a1' does not change significantly.

Peaks a1, a2, a3, c1 and c2 all occur at the same potentials as in the uncharged case. However, a hitherto unknown peak a1' was created at a potential of roughly -0.9 V versus SSCsat. According to the Pourbaix diagram in the figure 4.6, this potential corresponds to hydrogen evolution. According to the equation below, hydrogen is evolved from the electrolyte during the charging process.



The hydrogen atoms are initially adsorbed or chemisorbed on the sample surface and subsurface, then diffuse into the bulk, where they may become trapped. Accordingly, peak a1' is attributed to diffusible hydrogen desorbed from the specimen's bulk. The hydrogen measured by this approach comprises contributions from surface and subsurface sites, as well as reversible traps in the bulk of the specimen, such as grain boundaries[31]. Upon further cycling, the hydrogen-related peak completely vanished. It can be inferred that the a1' peak was related to complete evolution of diffusible hydrogen from the material.

Additionally, from figures 4.11b and 4.11c, it can be observed that with further cycling the peak a1 disappears, while peak a2 and c1 stabilizes. It can be inferred that the oxide products formed at peak a1 are the primary reactants for the oxidation reaction taking place at a2. Any further increase in the intensities of peak a2 and c1 is probably due to the formation of multilayers of the metal oxide or is due to surface roughening[102].

In the paper by Ozdirik et al.[102], it was suggested that the peak at a1 might be formed due to two possible reaction phenomena. The first hypothesis was mentioned earlier and the second one is due to the presence of thiourea. They proposed that the thiourea is adsorbed on the metal surface in alkaline electrolytes and gets irreversibly transformed by hydrolysis. H_2S is then adsorbed into the surface and

decomposed to facilitate the formation of a chemisorbed layer of Sulphur on the metal surface. It was assumed that the peak a1 could have been formed due to the oxidation reaction of sulphur to sulphate at the respective potential.

To clarify the attribution of the peak a1, some CV experiments were done with 1 M NaOH (without Thiourea). The figure 4.12 shows a comparison of the peaks a1', a1 and a2 formed in the CV after Hydrogen charging for DP1000 with two electrolyte, 1M NaOH and 1M NaOH + 8 g/L Thiourea. It can be observed that the the peak a1 appears in the case of both electrolytes and does not seem to depend on the presence of Thiourea. Therefore the first hypothesis seems more likely. The

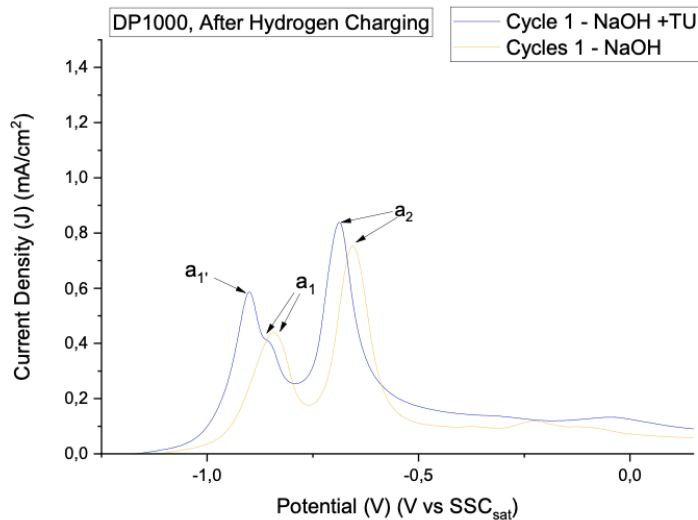


Figure 4.12: Comparison of a1 peaks after hydrogen charging for DP1000 in 1 M NaOH solution and 1 M NaOH solution containing 8 g/l thiourea (scan rate 10 mV/s).

table A.1 showing the peak values relating to the CV's of the material can be found in the appendix. The general peak positions of all the peaks are indicated.

4.3.1.2 Pure Iron

The analysis of Pure Iron with respect to CV is quite similar to the DP1000 steel. The main difference between the two is that the current intensities of all the peaks are more in the case of pure iron. Additionally, the Mn-related peaks are also not seen in the CV for Pure Iron, which again agrees with the composition of the pure iron sample. Figure 4.11 shows the voltammograms obtained for the CV scan of Pure Iron.

The table A.2 in the appendix shows the peak values relating to the CV's of the Pure Iron - Pre-Conditioning A. The general peak positions of all the peaks are indicated.

4.3.1.3 AISI 420

The analysis of AISI 420 with respect to CV is quite similar to the DP1000 steel and Pure Iron. Figure 4.14a shows the main difference between the CV's for AISI 420 and the other two materials. The peak a1 in the CV's for DP1000 and Pure Iron, that is related to the non-equilibrium (hydr)oxidation reaction, does not appear in the CV for the AISI 420 material.

The integration of the peaks at a2 and c1 shows that the amount of charge released is similar. The standard potential of this reaction was calculated, and based on the pourbaix diagram in the figure 4.6 and Literature[102, 37, 119, 120], the peaks are generally attributed to (hydr)oxidation/reduction reactions. The following re-

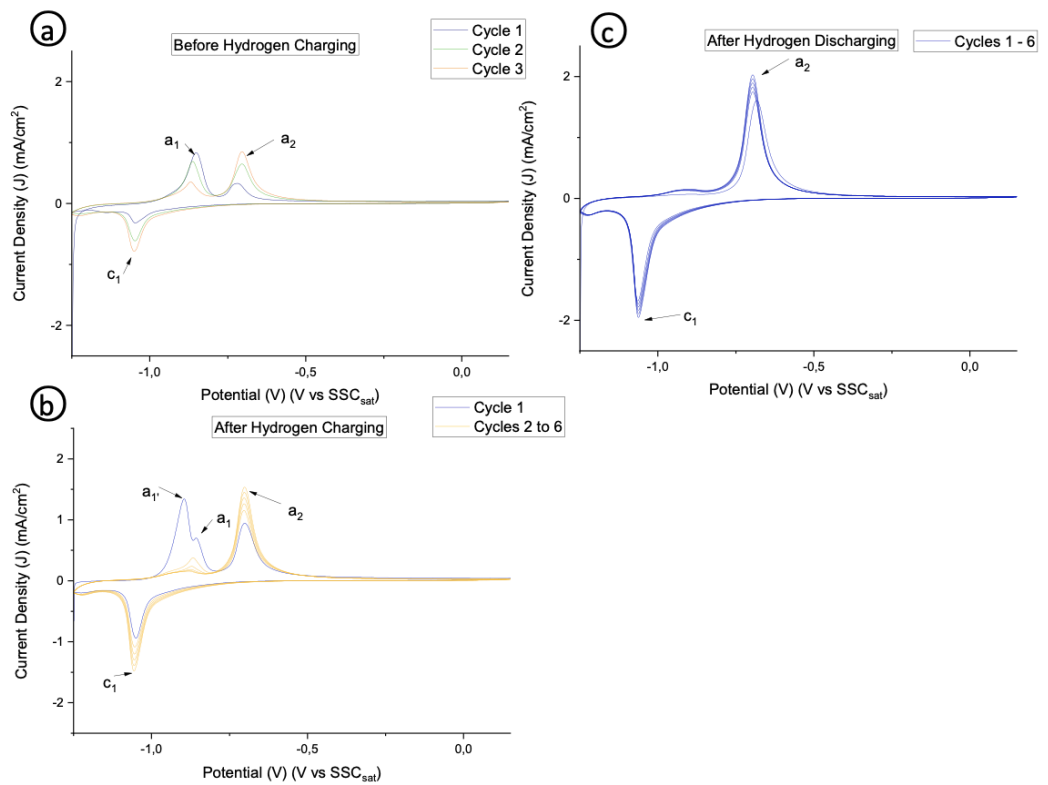
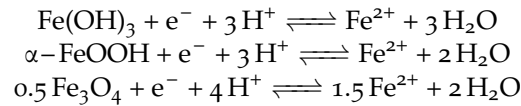


Figure 4.13: Overview of the procedure for cyclic voltammetry, Pure Iron (a) three CV scans before hydrogen charging, (b) six CV scans after 1 hour of hydrogen charging and (c) six CV scans after 30 mins of hydrogen discharging in 1 M NaOH solution containing 8 g/l thiourea solution (scan rate 10 mV/s).

actions can take place, as to the exact reactions will be discussed in the following chapter in detail.



Then, in the potential region between approx -0.2 V to -0.6 V vs SSC_{sat}, the current response is more or less constant, showing the passivity of the surface due to the formation of oxide layers. During the reverse scan, apart from the c1 peak, there is a peak in the current response at c2, indicating the irreversible reduction of the oxidative species of non-equilibrium products.

The current intensities of the peaks a2 and c1 are observed to decrease with time though not by a large degree. This might have something to do with the protective air-formed oxide on the material or the oxide layer formed on the steel due to the alkaline environment, which is comprised of chromates that do not get reduced in the potential sweep range of (-1.25 to 0.15) V vs SSC_{sat}. To prove the latter, some additional CV tests were done with the AISI 420 material using a larger potential window where oxidation/reduction of chromium species might be expected to occur. It was found that the peaks relating to a2 and c1 increased with subsequent scans. It can be gathered that the redox reactions of the chromium compounds allowed for or promoted the redox reactions for the Fe compounds in the steel.

Figure 4.14 shows the voltammograms obtained for the CV scan of AISI 420.

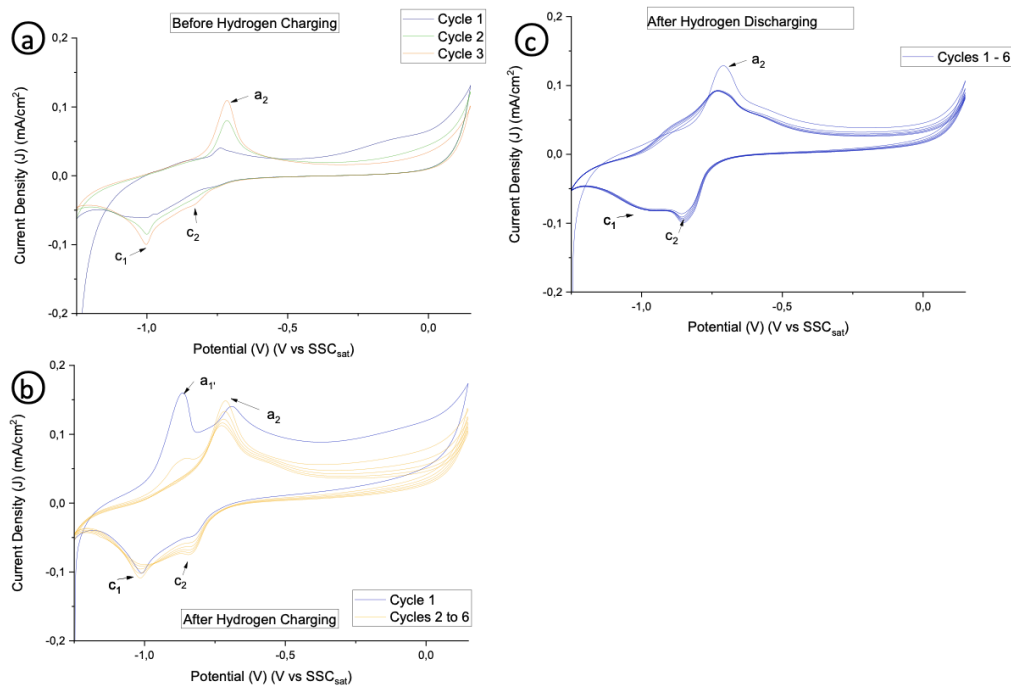
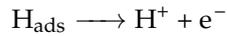


Figure 4.14: Overview of the procedure for cyclic voltammetry, AISI 420 (a) three CV scans before hydrogen charging, (b) six CV scans after 1 hour of hydrogen charging and (c) six CV scans after 30 mins of hydrogen discharging in 1 M NaOH solution containing 8 g/l thiourea solution (scan rate 10 mV/s).

After the material is charged with Hydrogen^{4.14b}, in the first forward scan, a peak a₁' appears that did not exist in the CV before Hydrogen charging. This peak intensity decreases significantly with the number of cycles until the peak almost disappears as it reaches the 4th CV cycle. The assignment of this peak is a bit problematic in the case of AISI 420 as there is nothing in the Literature, to this author's knowledge, that could explain its presence.

Now, there is hypotheses as to what this peak might represent. It is related to H desorption; the peak appears at a potential range where H evolution can be assumed to occur (pourbaix diagram 4.7).

It is known from Literature that diffusible H in the bulk of the metal bound to relatively weak traps like grain boundaries and dislocations have low activation energy. Therefore, it gets desorbed from the bulk of the alloy[122].



To give further proof to this hypothesis, tests were done with the AISI 420 material in 1 M NaOH + 8 g/L Thiourea, with a charging duration of 3 hours instead of the 1-hour duration previously taken for the experiment. The figure 4.15 shows a comparison of the peak a_1' for two CV curves after H charging for 1 hour and 3 hours. It can be observed that the peak a_1' is higher after H charging for 3 hours compared to 1 hour. From this, it was assumed that the peak a_1' in figure 4.14b is

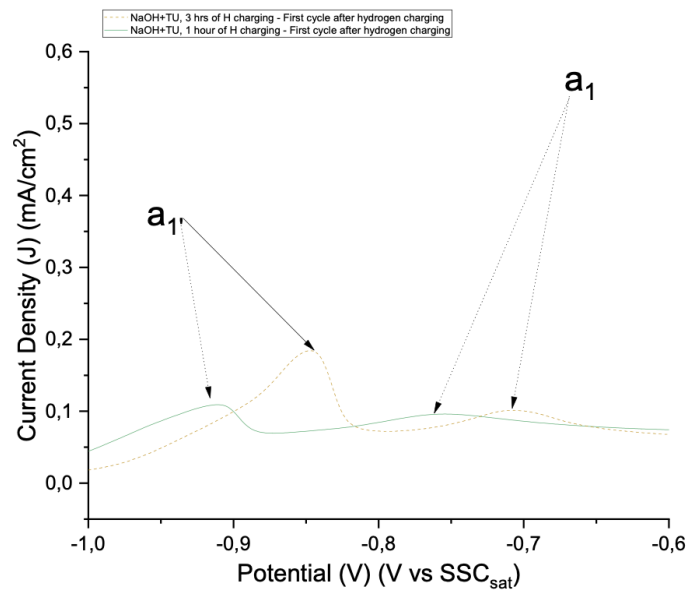


Figure 4.15: Comparison of the peak a_1' for two CV curves after H charging for 1 hour and 3 hours, AISI 420 in 1 M NaOH solution containing 8 g/l thiourea solution (scan rate 10 mV/s).

related to H desorption.

The table A.3 in the appendix shows the peak values relating to the CV's of the material. The general peak positions of all the peaks are indicated.

4.3.2 Passive Behaviour (Pre-conditioning B) - Attribution of Peaks

4.3.2.1 DP1000

The attribution of peaks is exactly the same as that for the DP steel in Active behaviour. The most important difference is in the current response of the a_1' peak, which is associated with H desorption. In the figure 4.16b, the current response is lower than that in figure 4.11b. Additionally, the a_3 and c_2 peaks related to the Mn redox processes is also only barely visible. Figure 4.16 shows the voltammograms obtained for the CV scan of DP1000.

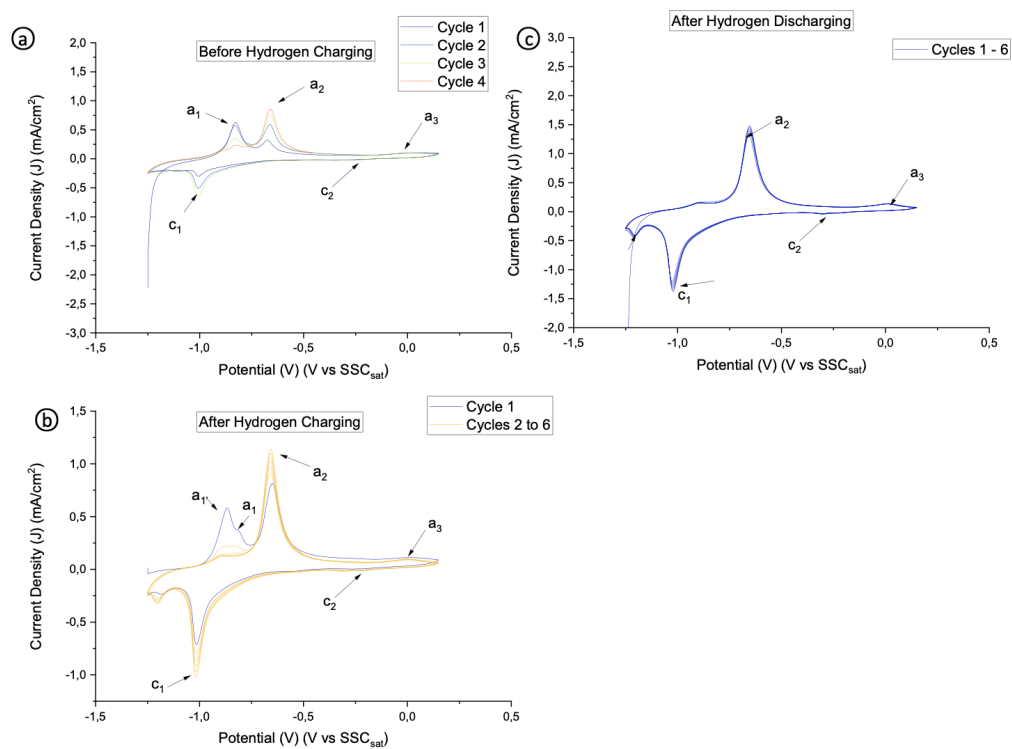


Figure 4.16: Overview of the procedure for cyclic voltammetry, DP1000, Pre-conditioning B (a) three CV scans before hydrogen charging, (b) six CV scans after 1 hour of hydrogen charging and (c) six CV scans after 30 mins of hydrogen discharging in 1 M NaOH solution containing 8 g/l thiourea solution (scan rate 10 mV/s).

The table A.4 in the appendix shows the peak values relating to the CV's of the material. The general peak positions of all the peaks are indicated. The values of peak potentials are more or less similar for both active and passive behaviour.

4.3.2.2 Pure Iron

The attribution of peaks is exactly the same as that for the Pure Iron in Active behaviour. The most important difference is in the current response of the a₁' peak, which is associated with H desorption. In the figure 4.17b, the current response is lower than that in figure 4.13b. Figure 4.17 shows the voltammograms obtained for the CV scan of Pure Iron.

The table A.4 in the appendix shows the peak values relating to the CV's of the material. The general peak positions of all the peaks are indicated. The values of peak potentials are more or less similar for both active and passive behaviour.

4.3.2.3 AISI 420

The attribution of peaks is exactly the same as that for the AISI 420 in Active behaviour. The most important difference is in the current response of the a₁' peak, which is associated with H desorption. In the figure 4.18b, the current response is lower than that in figure 4.14b. Figure 4.18 shows the voltammograms obtained for the CV scan of AISI 420.

The table A.4 in the appendix shows the peak values relating to the CV's of the material. The general peak positions of all the peaks are indicated. The values of peak potentials are more or less similar for both active and passive behaviour.

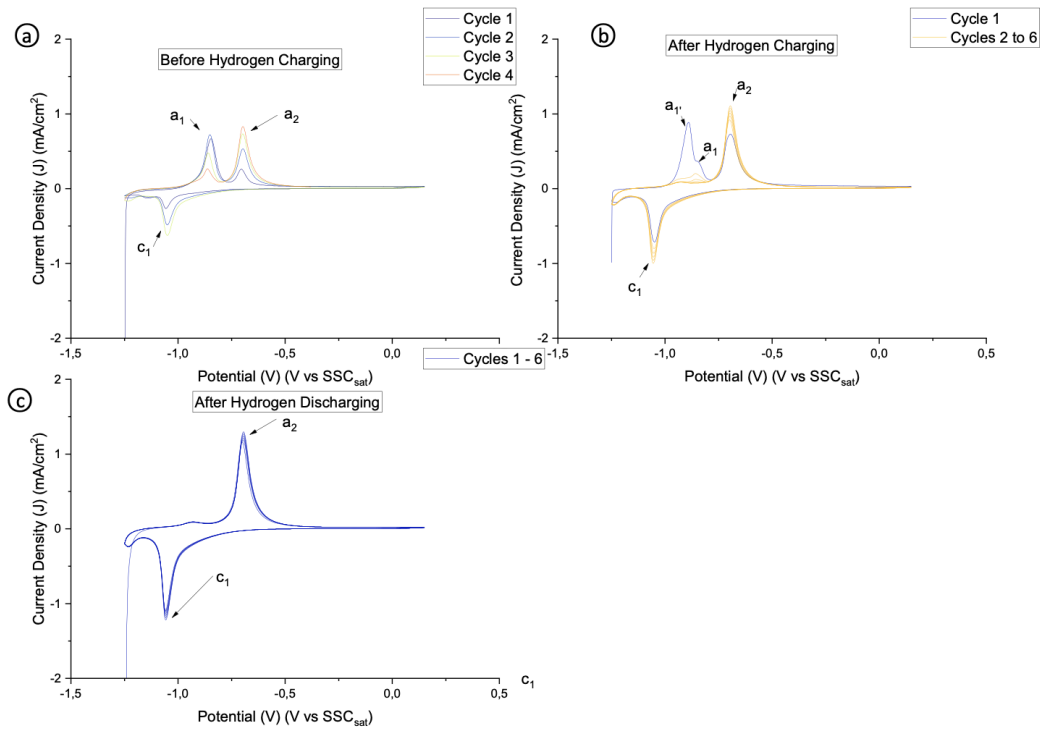


Figure 4.17: Overview of the procedure for cyclic voltammetry, Pure Iron, Pre-conditioning B (a) three CV scans before hydrogen charging, (b) six CV scans after 1 hour of hydrogen charging and (c) six CV scans after 30 mins of hydrogen discharging in 1 M NaOH solution containing 8 g/l thiourea solution (scan rate 10 mV/s).

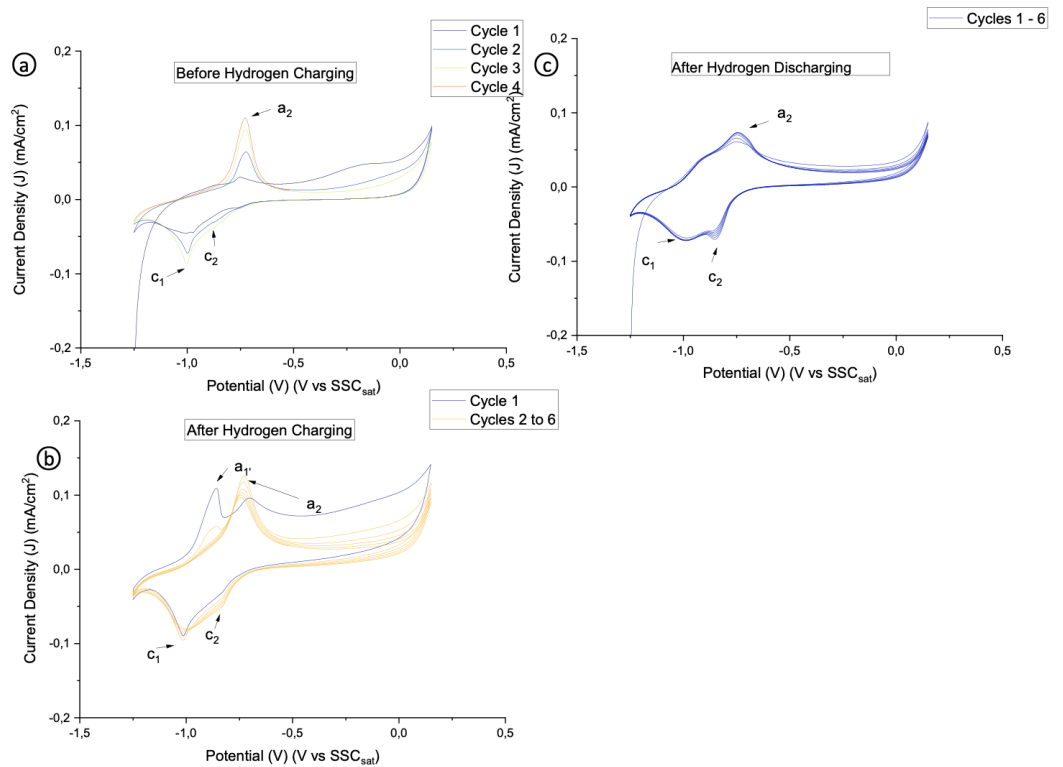


Figure 4.18: Overview of the procedure for cyclic voltammetry, AISI 420, Pre-conditioning B (a) three CV scans before hydrogen charging, (b) six CV scans after 1 hour of hydrogen charging and (c) six CV scans after 30 mins of hydrogen discharging in 1 M NaOH solution containing 8 g/l thiourea solution (scan rate 10 mV/s).

4.3.3 Detection of Hydrogen and Data Processing

Several ways can be used to quantify the desorbed hydrogen from CV. The most popular way is to determine the amount of hydrogen corresponding to the hydrogen peak seen in the first CV scan after hydrogen charging. This study also uses the same method. The amount of hydrogen desorbed can be calculated using the variables recorded by the potentiostat during the CV experiment, specifically the total charge (Q). Each electron corresponds to one hydrogen atom (desorbed via the Volmer-Heyrovsky pathway). As a result, it is feasible to directly correlate with the quantity of hydrogen atoms desorbed off the material's surface. It is important to note that when the potential is near the E_i , a very small amount of hydrogen is probably being adsorbed into the material. However, because this amount is so small, it does not produce a hydrogen desorption peak on the CV scans before H₂ loading and can thus be ignored.

The "Peak Baseline analyser" feature in the Origin Pro program is used to obtain the H desorption data. The last anodic scan from the CV before H charging is used as the baseline scan, which is then subtracted from the first anodic CV scan after H charging. Then, the hydrogen related a_1' peak is deconvoluted from any overlapping peaks, and the area under the peak is determined. This area is measured in V.A/cm². Divided by the voltage sweep rate (V/s), this yields the surface charge density. See equation below,

$$\rho_{desorbed}(C/cm^2) = \frac{PeakArea(V.A/cm^2)}{SweepRate(V/s)}$$

A comparison of the hydrogen-related, after H charging, CV peak a_1' for DP1000, Pure Iron and AISI 420 in both Active Behaviour (Pre-conditioning A) and Passive Behaviour (Pre-conditioning B) is presented in figure 4.19.

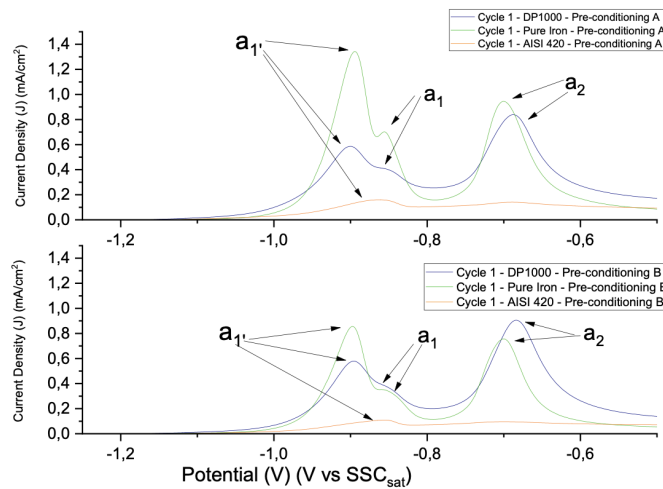


Figure 4.19: A comparison of the hydrogen-related, after H charging, CV peak a_1' for DP1000, Pure Iron and AISI 420 in both Active Behaviour (Pre-conditioning A) and Passive Behaviour (Pre-conditioning B).

It can be seen from the figure 4.19 that the pure iron sample has the highest peak current intensity, followed by the dual phase steel sample and then the AISI 420 sample. The bar graph in figure 4.20 shows the Hydrogen desorption as a function of the surface charge density. It can be seen that for both pre-conditioning types, the pure iron sample has the highest surface charge density, followed by the dual phase steel sample and then the AISI 420 sample. When comparing the pre-conditioning types A and B, it can be seen from both figures 4.15 and 4.19 that more Hydrogen is desorbed from the materials when the H is charged directly to the active surface

instead of the passive surface. It can be speculated that this is due to the passive layer on the metals' surface acting as a barrier for H adsorption. The next chapter will address this in relation to the Microstructure and the EIS.

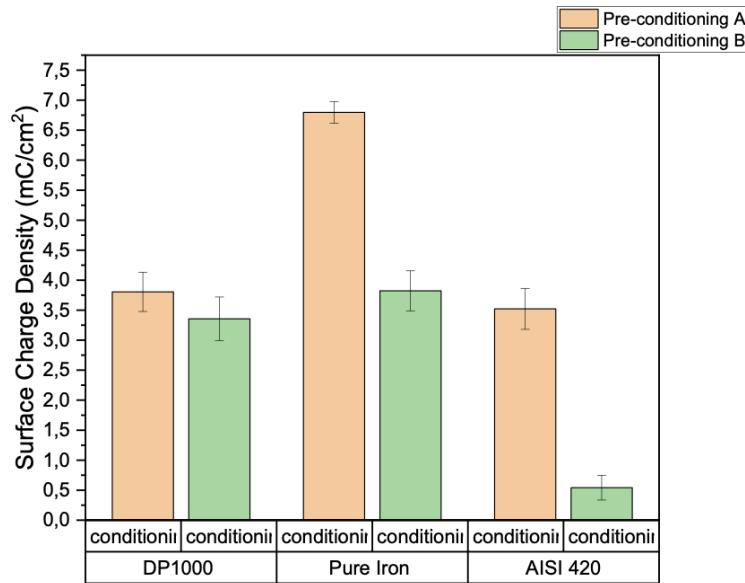


Figure 4.20: A comparison of the surface charge density under the α_1' peak for DP1000, Pure Iron and AISI 420 in both Active Behaviour (Pre-conditioning A) and Passive Behaviour (Pre-conditioning B).

4.4 H/material interaction - Electrochemical Experiments - Electrochemical Impedance Spectroscopy (EIS)

4.4.1 Active Behaviour (Pre-conditioning A)

4.4.1.1 DP1000

Electrochemical Impedance Spectroscopy (EIS) is performed on the samples in the solution medium, Before H Charging, After H Charging and After H Discharging, to understand the electrochemical interface and the corrosion resistance of the samples. EIS investigations are demonstrated in the figure 4.21, which shows selected Nyquist and Bode plots for the DP1000 material in 1 M NaOH + 8 g/L Thiourea solution. From the figure 4.21b, the shape of the Nyquist plots is identical across the samples, with an incomplete semi-circular appearance. Nyquist plots show that the dual phase steel sample exhibits a larger arc diameter in before H charging when compared to after H charging and after H discharging. The smaller arcs for the other two steps, found at higher frequencies, are only clearly identified after zooming in on the graph. It can be seen from the decreasing arc diameters across the three steps (Before H charging, After H charging and After H Discharging) that the sample before H charging shows a more corrosion-resistant electrochemical response as the H charging procedure proceeds. The bigger the capacitance arc radius, the higher the stability of the film[123].

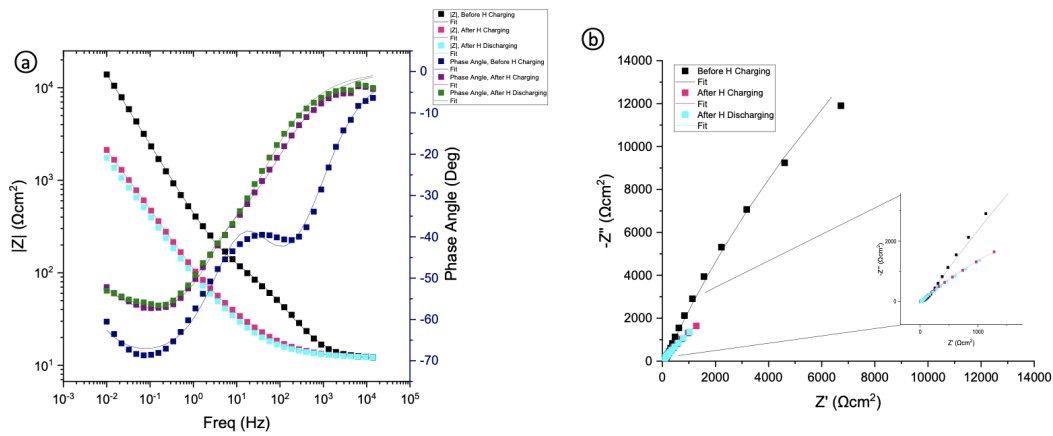


Figure 4.21: (a) Bode plots of DP1000: Before H Charging, After H Discharging and After H Charging in 1 M NaOH solution containing 8 g/l thiourea solution; (b) Nyquist plots of DP1000: Before H Charging, After H Discharging and After H Charging in 1 M NaOH solution containing 8 g/l thiourea solution - Pre-conditioning A.

The Bode $|Z|$ plots, in figure 4.21a, of the samples show frequency-independent regions at high frequencies and a linear slope in the intermediate to low frequencies related to the double-layer capacitance and the passive layer capacitance. The phase angle curves show the deviation from the ideal behaviour of the capacitance. This behaviour is attributed to the inhomogeneities and roughness of the working electrode surface[22, 116].

The inherent quality of the film is related to the impedance of the low-frequency flat surface in the bode $|Z|$ plot. The combination of the electrolyte resistance, transfer resistance, and surface layer resistance is represented by this low-frequency platform. Changes in the low-frequency plateau represent changes in the film and can be attributed to the conductive channels through the film. The Bode plots also show a higher impedance value for the DP material before H charging, at the low frequency of 0.01 Hz. Additionally, the impedance $|Z|$ values at low frequencies, are very close by for the samples after H charging and after H discharging. The increase in low-frequency impedance is indicative of a higher corrosion resistance of the film formed on the metal surface. The impedance modulus values for the "before H charging" step, the "after H charging" step and the "after H discharging" step are 13.931 k Ω cm², 2.123 k Ω cm² and 1.712 k Ω cm², respectively, at the low frequency of 0.01 Hz.

The two time constants are more clearly visualized in the Bode plot, especially in the twin valleys that appear in the phase angle plots for the "before H charging" step. The "after H charging" and the "after H discharging" steps only show one time constant that can be clearly visualized, but there does exist an additional shallow valley.

Solid lines show the fitted curves by the proposed equivalent circuit. $|Z|$ values correspond to the impedance modulus values in the Bode plots. The EIS results are fitted by an electrical equivalent circuit (EEC) shown in the figure 4.22.

The larger arc in the Nyquist plots and the higher impedance modulus values in the Bode plots for the DP samples after H charging, indicates a higher barrier property for the passive layer formed on the Dual-phase material. It can be said that due to the multilayers of oxide formed during the CV cycles, the barrier properties of the passive layer are reduced[102]. This leaves further room for discussion relating to the microstructure of the material and the H absorption into the material.

Electrical equivalent circuits were obtained based on ZView software. The EEC circuit chosen in the study with two time constants was used in a recent study for fitting the EIS response of Dual Phase steels in an alkaline NaOH environment[22].

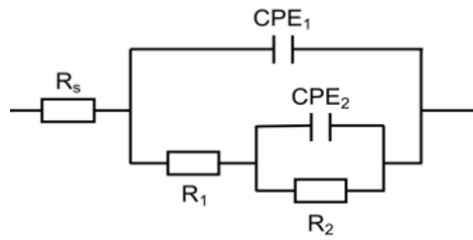


Figure 4.22: Equivalent circuit proposed for modelling the electrochemical response of DP1000 in 1 M NaOH solution containing 8 g/l thiourea solution - Pre-conditioning A[22].

The presence of two visible time constants, in the form of valleys in the $|Z|$ vs Hz Bode plot also lead to the assumption of the EEC circuit in figure 4.22. Additionally two other models were also chosen to try the fitting (See figure 4.23 a b), but the fitting results were not good.

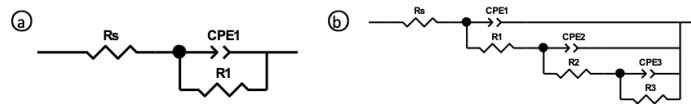


Figure 4.23: Equivalent circuits considered for modelling the electrochemical response of DP1000 in 1 M NaOH solution containing 8 g/l thiourea solution - Pre-conditioning A[22].

R_s represents the resistance of the electrolyte, R_1 and CPE_1 , the resistance and capacitance of the double layer, R_2 is the passive layer resistance and CPE_2 is the capacitance of the passive film surface. Constant phase elements (CPE) are used instead of capacitors due to the deviation from the ideal capacitive behaviour. Capacitance values, C_1 and C_2 , are calculated using the resistance, R_1 and R_2 , and constant phase element values, QPE_{1-T} and QPE_{1-P} ; QPE_{2-T} and QPE_{2-P} , with the Hsu and Mansfeld approach, where $QPE-T$ is Q and $QPE-P$ is n .

$$Capacitance(C) = R^{(1-n)/n} Q^{1/n}$$

The table 4.4 shows the equivalent circuit parameters obtained by fitting the collected EIS data of DP1000 in Active Behaviour (Pre-conditioning A). The parameters are the averaged values and standard deviation Error resulting from minimum three measurement repetitions. The Chi Sqr. value is obtained from the ZView fitting software. The equivalent resistance value of the passive film layer, R_2 , is significantly higher before H charging. The R_2 values after H charging and after H discharging are similar especially when considering the error. Calculated Capacitance value is higher before H charging. The C values after H charging and after H discharging are similar especially when considering the error. Despite the good fit of the equivalent circuits with their low Chi-Squared value, there appeared to be an appreciable scatter in some of the EIS parameters obtained across 3-4 measurement repetitions. This could relate to an issue with the reproducibility of the EIS data, due to changes in the experimental conditions.

4.4.1.2 Pure Iron

Electrochemical Impedance Spectroscopy (EIS) is performed on the Pure Iron samples in the solution medium, Before H Charging, After H Charging and After H Discharging, to understand the electrochemical interface and the corrosion resistance of the samples. EIS investigations are demonstrated in the figure 4.24, which

show selected Nyquist and Bode plots for the Pure Iron material in 1 M NaOH + 8 g/L Thiourea solution.

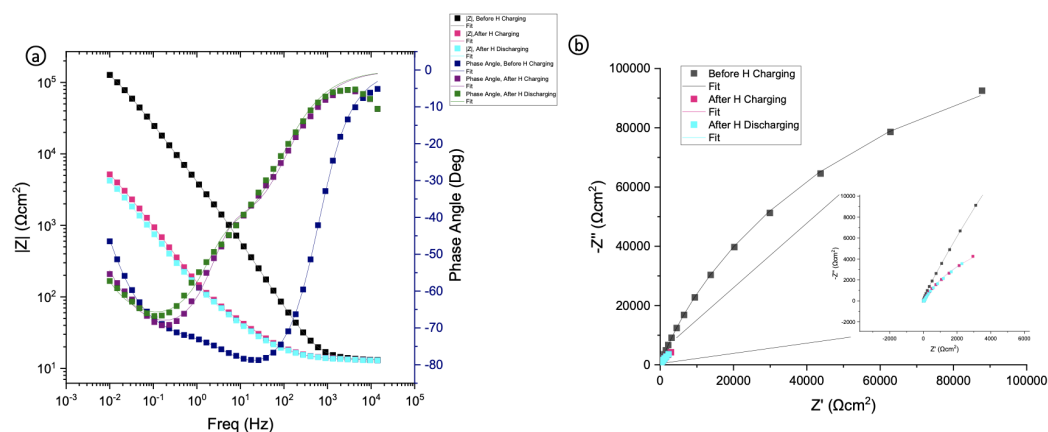


Figure 4.24: (a) Bode plots of Pure Iron: Before H Charging, After H Discharging and After H Charging in 1 M NaOH solution containing 8 g/l thiourea solution; (b) Nyquist plots of Pure Iron: Before H Charging, After H Discharging and After H Charging, After H Discharging in 1 M NaOH solution containing 8 g/l thiourea solution - Pre-conditioning A.

A similar trend when compared to the DP1000 material can be observed in the Pure Iron material. In the pure iron sample's bode plot (4.21a), the time constant in the lower frequency ranges is not as prominent as the time constant indicated by the deep valley in the higher half of the frequency range. This could mean that, for the pure Iron sample before H charging, the resistance offered by charge transfer dominates in the material. However, from the bode plot it can be observed that after H charging and discharging, the resistance offered by the passive film is also a relevant part of the overall resistance offered by the system.

The same trend as seen with the dual phase material follows from the Nyquist plots. It can be seen from the decreasing arc diameters across the three steps (Before H charging, After H charging and After H Discharging) that the sample before H charging shows a more corrosion-resistant electrochemical response as the H charging procedure proceeds. The bigger the capacitance arc radius, the higher the stability of the film [123]. The impedance modulus values for the pure iron sample for the "before H charging" step, the "after H charging" step and the "after H discharging" step is 127.536 kΩcm², 5.173 kΩcm² and 4.229 kΩcm², respectively at the low frequency of 0.01 Hz. The difference in the $|Z|$ modulus values between the before H charging step and the after H charging is much higher than in the dual phase steel material case. From the CV data, it was observed that pure iron absorbs more H during the 1-hour charging duration than DP steel. Now, considering that the adsorption of H reduced the corrosion resistance of the passive layer, it makes sense that the difference in $|Z|$ values is higher in the case of the pure Iron sample. This will be further discussed in the next chapter.

Electrical equivalent circuits were obtained based on ZView software. The EEC circuit chosen in the study for Pure Iron is shown in figure 4.22. The presence of two visible time constants, in the form of valleys in the $|Z|$ vs Hz Bode plot lead to the assumption of the EEC circuit. Additionally two other models were also chosen to try the fitting (See figure 4.23 a b), but the fitting results were not good.

The table 4.4 shows the equivalent circuit parameters obtained by fitting the collected EIS data of Pure Iron in Active Behaviour (Pre-conditioning A). The parameters are the averaged values and standard deviation Error resulting from minimum three measurement repetitions. The Chi Sqr. value is obtained from the ZView fitting software. The equivalent resistance value of the passive film layer, R₂, is significantly higher before H charging. The R₂ values after H charging and after H

discharging are similar especially when considering the error. Calculated Capacitance value is lower before H charging. The C values after H charging and after H discharging are similar especially when considering the error. Despite the good fit of the equivalent circuits with their low Chi-Squared value, there appeared to be an appreciable scatter in some of the EIS parameters obtained across 3-4 measurement repetitions. This could relate to an issue with the reproducibility of the EIS data, due to changes in the experimental conditions.

4.4.1.3 AISI 420

Electrochemical Impedance Spectroscopy (EIS) is performed on the AISI 420 samples in the solution medium, Before H Charging, After H Charging and After H Discharging, to understand the electrochemical interface and the corrosion resistance of the samples. EIS investigations are demonstrated in the figures 4.25b and 4.25a, which show selected Nyquist and Bode plots for the AISI 420 material in 1 M NaOH + 8 g/L Thiourea solution.

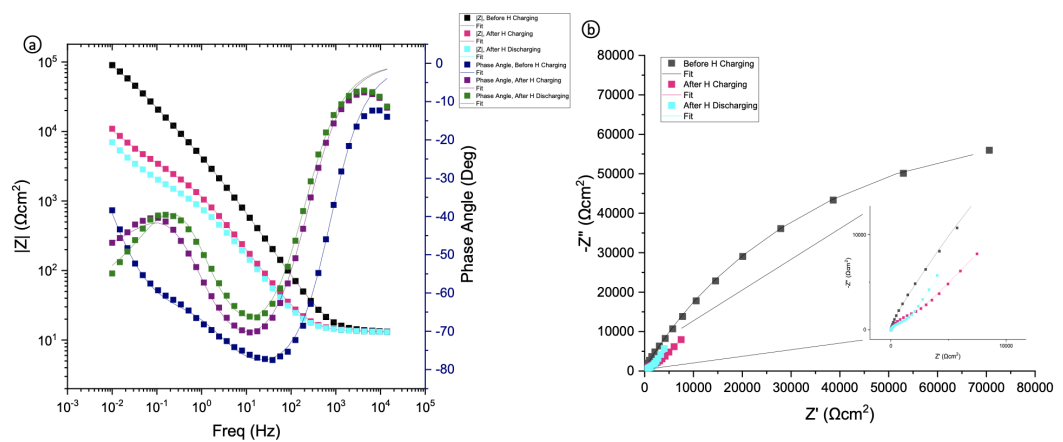


Figure 4.25: (a) Bode plots of AISI 420: Before H Charging, After H Discharging and After H Discharging in 1 M NaOH solution containing 8 g/l thiourea solution; (b) Nyquist plots of AISI 420: Before H Charging, After H Discharging and After H Discharging in 1 M NaOH solution containing 8 g/l thiourea solution - Pre-conditioning A.

A similar trend when compared to the DP1000 material and the Pure Iron material can be observed here. In the AISI 420 material's bode plot (4.25a), the time constant in the lower frequency ranges is not as prominent as the time constant indicated by the deep valley in the higher half of the frequency range. This means that, before H charging, the resistance offered by charge transfer dominates in the material. However, after H charging and discharging, the time constant indicated in the lower half of the frequency range is seen to dominate over the other time constant. This means that the oxide layer formed on the AISI 420 material contributes significantly to the overall impedance offered by the system.

From the Nyquist plots 4.25b, the same trend as seen with the other two materials follows. It can be seen from the decreasing arc diameters across the three steps (Before H charging, After H charging and After H Discharging) that the sample before H charging shows a more corrosion-resistant electrochemical response as the H charging procedure proceeds. The bigger the capacitance arc radius, the higher the stability of the film [123]. The impedance modulus values for the "before H charging" step, the "after H charging" step and the "after H discharging" step are 67.89 $\text{k}\Omega\text{cm}^2$, 10.26 $\text{k}\Omega\text{cm}^2$ and 6.986 $\text{k}\Omega\text{cm}^2$, respectively, at the low frequency of 0.01 Hz. The difference in the $|Z|$ modulus values for the AISI 420 sample before and after H charging is higher than that of the dual phase steel material but lower than that of the pure iron material. This is an interesting point for further discussion.

Electrical equivalent circuits were obtained based on ZView software. The EEC circuit chosen in the study for AISI 420 is shown in figure 4.22. While the data does not immediately reveal the presence of a distinct second time constant, the circuit shown in Figure 4.22 suited the EIS data considerably better. In the literature [124, 125, 22], this circuit is also frequently employed for stainless steel and passive materials with oxide coatings. The presence of two visible time constants, in the form of valleys in the $|Z|$ vs Hz Bode plot lead to the assumption of the EEC circuit. Additionally two other models were also chosen to try the fitting (See figure 4.23 a b), but the fitting results were not good. While the circuit in figure 4.23a is a fairly typical circuit for fitting EIS data in stainless steel research and was also utilized by Lu et al. [126], it was discovered that this circuit did not fit the data properly.

The table 4.4 shows the equivalent circuit parameters obtained by fitting the collected EIS data of AISI 420 in Active Behaviour (Pre-conditioning A). The parameters are the averaged values and standard deviation Error resulting from minimum three measurement repetitions. The Chi Sqr. value is obtained from the ZView fitting software. The equivalent resistance value of the passive film layer, R_2 , before H charging, after H charging and after H discharging are similar especially when considering the error. Calculated Capacitance value is lower before H charging. The C values after H charging is higher than after H discharging. Despite the good fit of the equivalent circuits with their low Chi-Squared value, there could be a fitting anomaly or an artefact of the equipment.

Table 4.4: Equivalent circuit parameters obtained by fitting the collected EIS data of DP1000, Pure Iron and AISI 420 samples in Active Behaviour (Pre-conditioning A). Parameters are the averaged values and standard deviation resulting from three measurement repetitions. The Chi Sqr. value is obtained from the ZView fitting software.

Material	Step	Rs		CPEr-T		R1		C1		CPEz-T		R2		C2		Chi-Sqr				
		(Ωcm^2)	\pm Error	($W^{-1}s^{\alpha}\text{cm}^2$ $\times 10^{-5}$)	\pm Error	(Ωcm^2)	\pm Error	($F\text{cm}^{-2}$ $\times 10^{-5}$)	\pm Error	($W^{-1}s^{\alpha}\text{cm}^2$ $\times 10^{-5}$)	\pm Error	(Ωcm^2)	\pm Error	($F\text{cm}^{-2}$ $\times 10^{-5}$)						
DP1000	Before H Charging	17.4	2.8	12.02	2.00	0.79	0.02	280.2	53.6	4.21	0.35	37.87	1.90	0.56	0.09	63178.5	5638.8	117.91	1.13	0.000398
	After H Charging	13.3	0.4	192.36	13.54	0.60	0.03	115.0	39.9	57.52	15.29	52.57	11.80	0.89	0.04	16280.7	1683.9	87.29	23.04	0.000142
	After H Discharging	17.5	3.9	171.45	93.70	0.74	0.08	111.9	78.1	125.36	81.78	174.43	94.21	0.76	0.12	17073	1283.3	47.68	34.75	0.000677
Pure Iron	Before H Charging	13.0	0.1	2.15	0.62	1.17	0.14	264.9	18.4	1.90	0.55	2.96	0.39	0.76	0.03	244040.0	26343.8	5.41	0.46	4.53E-05
	After H Charging	13.9	0.5	78.58	5.20	0.75	0.01	99.5	1.3	33.40	2.27	55.44	0.86	0.92	0.00	17657.3	1041.8	67.36	0.91	7.33E-04
	After H Discharging	13.4	0.2	104.68	4.36	0.63	0.05	128.9	2.0	37.28	8.72	65.01	1.29	0.90	0.01	20401.3	927.6	87.40	1.65	7.87E-04
AISI 420	Before H Charging	13.5	0.1	3.18	0.04	0.92	0.00	5359.0	273.7	2.73	0.04	5.27	0.96	0.63	0.01	175766.67	19432.17	20.27	5.63	5.30E-04
	After H Charging	13.3	0.1	12.80	0.34	0.87	0.00	2471.0	172.7	10.73	0.29	55.02	4.70	0.58	0.00	379450.00	91628.16	1278.3	240.48	5.25E-04
	After H Discharging	13.2	0.1	17.11	0.88	0.85	0.00	1495.0	106.7	13.45	0.83	99.35	4.93	0.70	0.04	211640	23462.87	219.80	38.73	1.32E-03

4.4.2 Passive Behaviour (Pre-conditioning B)

4.4.2.1 DP1000

Electrochemical Impedance Spectroscopy (EIS) is performed on the samples in the solution medium, Before H Charging, After H Charging and After H Discharging, to understand the electrochemical interface and the corrosion resistance of the samples. EIS investigations are demonstrated in the figure 4.26, which shows selected Nyquist and Bode plots for the DP1000 material in 1 M NaOH + 8 g/L Thiourea solution.

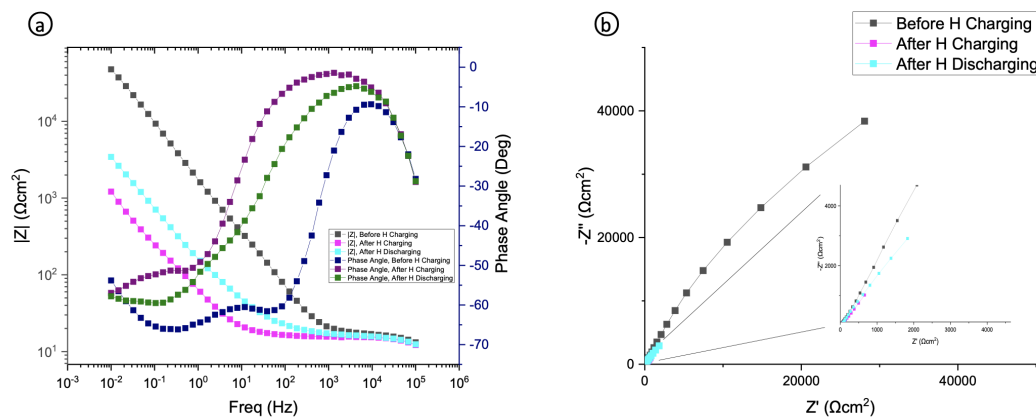


Figure 4.26: (a) Bode plots of DP1000: Before H Charging, After H Discharging and After H Discharging in 1 M NaOH solution containing 8 g/l thiourea solution; (b) Nyquist plots of DP1000: Before H Charging, After H Discharging and After H Discharging in 1 M NaOH solution containing 8 g/l thiourea solution - Pre-conditioning B.

From the figure 4.26b, the shape of the Nyquist plots is identical across the samples, with an incomplete semi-circular appearance. Nyquist plots show that the dual phase steel sample exhibits a larger arc diameter in before H charging when compared to after H charging and after H discharging. The smaller arcs for the other two steps, found at higher frequencies, are only clearly identified after zooming in on the graph. It can be seen from the decreasing arc diameters across the three steps (Before H charging, After H charging and After H Discharging) that the sample before H charging shows a more corrosion-resistant electrochemical response as the H charging procedure proceeds. The bigger the capacitance arc radius, the higher the stability of the film [123]. In contrast with the EIS plots of DP1000 with the active surface, the EIS plots of DP1000 with a passive surface have one significant difference in trend. From figure 4.26b it can be seen that the arc diameter of the curve for the sample after H charging is lesser than that of the sample after H discharging. This behaviour has been reflected in all repetitions of the EIS measurement. It can be inferred that, in the case of the pre-conditioning B, after the material is charged with H, the barrier properties of the passive film decrease, thereby reducing its corrosion resistance. After the H is discharged from the material, the barrier properties of the material increase, though not as high as it was initially.

The Bode $|Z|$ plots, in figure 4.26a, of the samples show frequency-independent regions at high frequencies and a linear slope in the intermediate to low frequencies related to the double-layer capacitance and the passive layer capacitance. The phase angle curves show the deviation from the ideal behaviour of the capacitance. This behaviour is attributed to the inhomogeneities and roughness of the working electrode surface [22, 116].

The Bode plots also show a higher impedance value for the DP material before H charging, at the low frequency of 0.01 Hz. Additionally, the impedance $|Z|$ values at low frequencies, are close by for the samples after H charging and after H discharging. The impedance modulus values for the "before H charging" step, the "after H charging" step and the "after H discharging" step are 14.739 k Ω cm², 0.376 k Ω cm² and 1.065 k Ω cm², respectively, at the low frequency of 0.01 Hz.

The two time constants are more clearly visualized in the Bode plot, especially in the twin valleys that appear in the phase angle plots for the "before H charging" step. The "after H charging" and the "after H discharging" steps only show one time constant that can be clearly visualized, but there does seem to exist an additional indistinct shallow valley.

The larger arc in the Nyquist plots and the higher impedance modulus values in the Bode plots for the DP samples after H charging, indicates a higher barrier property for the passive layer formed on the Dual-phase material. It can be said that due to the multilayers of oxide formed during the CV cycles, the barrier properties of the passive layer are reduced[102]. This leaves further room for discussion relating to the microstructure of the material and the H absorption into the material.

$|Z|$ values correspond to the impedance modulus values in the Bode plots. The EIS results are fitted by an electrical equivalent circuit (EEC) shown in the figure4.23.

Electrical equivalent circuits were obtained based on ZView software. The EEC circuit chosen in the study with two time constants was used in a recent study for fitting the EIS response of Dual Phase steels in an alkaline NaOH environment[22]. The presence of two visible time constants, in the form of valleys in the $|Z|$ vs Hz Bode plot also lead to the assumption of the EEC circuit in figure4.22. Additionally two other models were also chosen to try the fitting (See figure4.23 a b), but the fitting results were not good. The Hsu and Mansfeld approach was used to calculate the fitting parameters shown in table4.5.

The table 4.5 shows the equivalent circuit parameters obtained by fitting the collected EIS data of DP1000 in passive Behaviour (Pre-conditioning B). The parameters are the averaged values and standard deviation Error resulting from minimum three measurement repetitions. The Chi Sqr. value is obtained from the ZView fitting software. Despite the good fit of the equivalent circuits with their low Chi-Squared value, there appeared to be an appreciable scatter in some of the EIS parameters obtained across 3-4 measurement repetitions. This could relate to an issue with the reproducibility of the EIS data, due to changes in the experimental conditions.

4.4.2.2 Pure Iron

Electrochemical Impedance Spectroscopy (EIS) is performed on the Pure Iron samples in the solution medium, Before H Charging, After H Charging and After H Discharging, to understand the electrochemical interface and the corrosion resistance of the samples. EIS investigations are demonstrated in the figure 4.27, which show selected Nyquist and Bode plots for the Pure Iron material in 1 M NaOH + 8 g/L Thiourea solution.

A similar trend when compared to the Pure Iron material(Pre-conditioning A) can be observed in the Pure Iron material(Pre-conditioning B). In the pure iron sample's bode plot (4.26a), the time constant in the lower frequency ranges is not as prominent as the time constant indicated by the deep valley in the higher half of the frequency range. This could mean that, for the pure Iron sample before H charging, the resistance offered by charge transfer dominates in the material. However, from the bode plot it can be observed that after H charging and discharging, the resistance offered by the passive film is also a relevant part of the overall resistance offered by the system.

The same trend as seen with the dual phase material follows from the Nyquist plots. It can be seen from the decreasing arc diameters across the three steps (Before

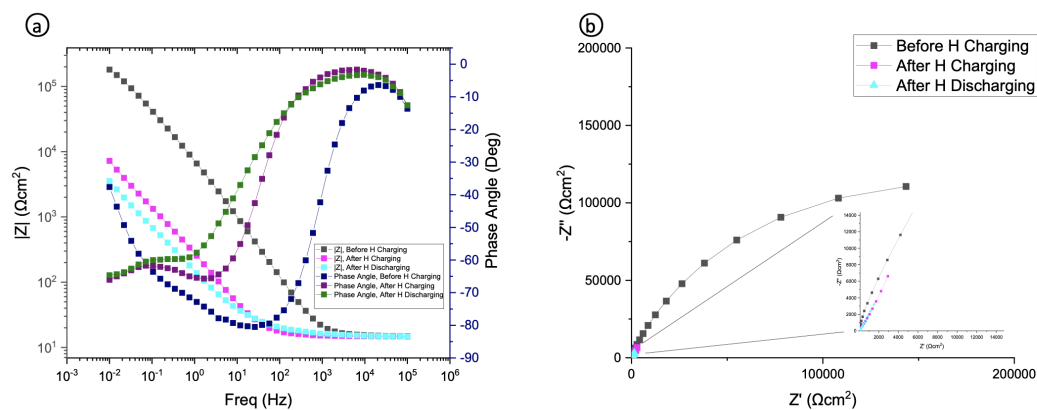


Figure 4.27: (a) Bode plots of Pure Iron: Before H Charging, After H Discharging and After H Charging in 1 M NaOH solution containing 8 g/l thiourea solution; (b) Nyquist plots of Pure Iron: Before H Charging, After H Discharging and After H Charging in 1 M NaOH solution containing 8 g/l thiourea solution - Pre-conditioning B.

H charging, After H charging and After H Discharging) that the sample before H charging shows a more corrosion-resistant electrochemical response as the H charging procedure proceeds. The bigger the capacitance arc radius, the higher the stability of the film[123]. The impedance modulus values for the pure iron sample for the "before H charging" step, the "after H charging" step and the "after H discharging" step is 54.154 $\text{k}\Omega\text{cm}^2$, 52.243 $\text{k}\Omega\text{cm}^2$ and 1.099 $\text{k}\Omega\text{cm}^2$, respectively at the low frequency of 0.01 Hz. The difference in the $|Z|$ modulus values between the before H charging step and the after H charging is much higher than in the dual phase steel material case. From the CV data, it was observed that pure iron absorbs more H during the 1-hour charging duration than DP steel. Now, considering that the adsorption of H reduced the corrosion resistance of the passive layer, it makes sense that the difference in $|Z|$ values is higher in the case of the pure Iron sample. This will be further discussed in the next chapter.

Electrical equivalent circuits were obtained based on ZView software. The EEC circuit chosen in the study for Pure Iron is shown in figure4.22. The presence of two visible time constants, in the form of valleys in the $|Z|$ vs Hz Bode plot lead to the assumption of the EEC circuit. Additionally two other models were also chosen to try the fitting (See figure4.23 a b), but the fitting results were not good.

The table 4.5 shows the equivalent circuit parameters obtained by fitting the collected EIS data of Pure Iron in Passive Behaviour (Pre-conditioning B). The parameters are the averaged values and standard deviation Error resulting from minimum three measurement repetitions. The Chi Sqr. value is obtained from the ZView fitting software. Despite the good fit of the equivalent circuits with their low Chi-Squared value, there appeared to be an appreciable scatter in some of the EIS parameters obtained across 3-4 measurement repetitions. This could relate to an issue with the reproducibility of the EIS data, due to changes in the experimental conditions.

4.4.2.3 AISI 420

Electrochemical Impedance Spectroscopy (EIS) is performed on the AISI 420 samples in the solution medium, Before H Charging, After H Charging and After H Discharging, to understand the electrochemical interface and the corrosion resistance of the samples. EIS investigations are demonstrated in the figures 4.28b and 4.28a, which show selected Nyquist and Bode plots for the AISI 420 material in 1 M NaOH + 8 g/L Thiourea solution.

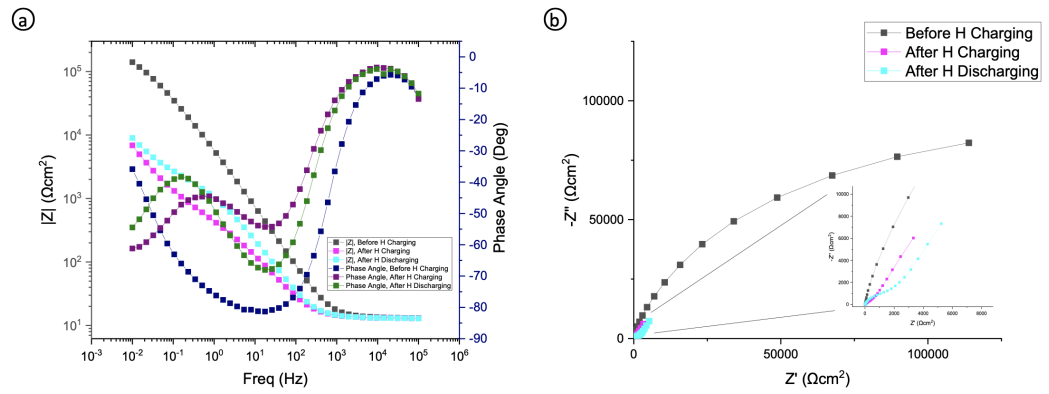


Figure 4.28: (a) Bode plots of AISI 420: Before H Charging, After H Discharging and After H Discharging in 1 M NaOH solution containing 8 g/l thiourea solution; (b) Nyquist plots of AISI 420: Before H Charging, After H Discharging and After H Discharging in 1 M NaOH solution containing 8 g/l thiourea solution - Pre-conditioning B.

A similar trend when compared to the DP1000 material and the Pure Iron material can be observed here. In the AISI 420 material's bode plot (4.28a), the time constant in the lower frequency ranges is not as prominent as the time constant indicated by the deep valley in the higher half of the frequency range. This means that, before H charging, the resistance offered by charge transfer dominates in the material. However, after H charging and discharging, the time constant indicated in the lower half of the frequency range is seen to dominate over the other time constant. This means that the oxide layer formed on the AISI 420 material contributes significantly to the overall impedance offered by the system.

From the Nyquist plots 4.28b, the same trend as seen with the other two materials follows. It can be seen from the decreasing arc diameters across the three steps (Before H charging, After H charging and After H Discharging) that the sample before H charging shows a more corrosion-resistant electrochemical response as the H charging procedure proceeds. The bigger the capacitance arc radius, the higher the stability of the film[123]. The arc diameters of the Nyquist curves for the material after H charging and after H discharging are similar, so one cannot be said to be higher than the other. The impedance modulus values for the "before H charging" step, the "after H charging" step and the "after H discharging" step are 43,564 kΩcm², 2.134 kΩcm² and 2.791 kΩcm², respectively, at the low frequency of 0.01 Hz.

Electrical equivalent circuits were obtained based on ZView software. The EEC circuit chosen in the study for AISI 420 is shown in figure 4.22. While the data does not immediately reveal the presence of a distinct second time constant, the circuit shown in Figure 4.22 suited the EIS data considerably better. In the literature[124, 125, 22], this circuit is also frequently employed for stainless steel and passive materials with oxide coatings. The presence of two visible time constants, in the form of valleys in the $|Z|$ vs Hz Bode plot lead to the assumption of the EEC circuit. Additionally two other models were also chosen to try the fitting (See figure 4.23 a b), but the fitting results were not good. While the circuit in figure 4.23a is a fairly typical circuit for fitting EIS data in stainless steel research and was also utilized by Lu et al.[126], it was discovered that this circuit did not fit the data properly.

The table 4.5 shows the equivalent circuit parameters obtained by fitting the collected EIS data of AISI 420 in Active Behaviour (Pre-conditioning A). The parameters are the averaged values and standard deviation Error resulting from minimum three measurement repetitions. The Chi Sqr. value is obtained from the ZView fitting software. Despite the good fit of the equivalent circuits with their low Chi-

Squared value, there appeared to be an appreciable scatter in some of the EIS parameters obtained across 3-4 measurement repetitions. This could relate to an issue with the reproducibility of the EIS data, due to changes in the experimental conditions.

Table 4.5: Equivalent circuit parameters obtained by fitting the collected EIS data of DP1000, Pure Iron and AISI 420 samples in Passive Behaviour (Pre-conditioning B). Parameters are the averaged values and standard deviation resulting from three measurement repetitions. The Chi Sqr. value is obtained from the ZView fitting software.

Material	Step	Rs (Ωcm^2)	\pm Error	CPEr-P	\pm Error	C1		CPEz-T		R2 (Ωcm^2)	\pm Error	C2		Chi-Sqr						
						R1 (Ωcm^2)	\pm Error	(10^{-5})	Fcm (10^{-5})			$(10^{-1})\text{s}^n\text{cm}^2$	\pm Error		Fcm $^{-1}$	$\times 10^{-5}$				
DP1000	Before H Charging	14.9	0.6	12.89	1.68	0.78	0.02	81674.0	49032.9	52.77	2.12	5431.42	3726.16	1.36	0.45	975.4	297.4	107.73	80.05	0.000744
	After H Charging	13.9	0.2	425.34	48.55	0.74	0.02	3587.0	1233.5	1569.43	536.58	370.87	90.87	1.35	0.20	5753.7	2006.7	323.23	66.20	0.002154
	After H Discharging	15.3	0.2	176.39	7.43	0.68	0.01	51910.0	16645.3	1589.07	496.98	547.26	140.45	1.82	0.11	18857.3	8984.1	342.74	121.85	0.002165
Pure Iron	Before H Charging	14.1	0.4	2.80	0.23	0.91	0.01	14457	2932.7	2.79	0.25	2.04	0.21	0.66	0.06	250323.3	36140.2	5.18	0.71	2.99E-03
	After H Charging	14.4	0.5	108.47	15.43	0.83	0.00	1591.0	128.5	120.60	18.22	70.89	9.29	0.69	0.01	264026.7	73480.3	653.13	79.42	7.79E-05
	After H Discharging	13.4	0.5	66.25	15.71	0.70	0.01	29.9	12.8	16.10	6.49	101.91	12.89	0.74	0.03	79710.7	17349.0	778.69	226.10	2.24E-04
AISI 420	Before H Charging	14.6	0.6	1.52	0.80	1.03	0.07	15.6	4.1	1.37	0.10	2.57	0.56	0.67	0.10	2.09E+05	1.52E+04	5.74	0.46	5.06E-04
	After H Charging	13.8	0.7	25.93	3.41	0.78	0.01	601.3	0.5	15.58	2.30	85.15	2.50	0.72	0.01	100940.00	40751.64	20462.5	1159.83	5.41E-04
	After H Discharging	14.1	0.8	12.43	0.31	0.86	0.00	1532.0	127.3	9.51	0.40	69.00	0.57	0.66	0.01	252140.00	85493.44	405.99	10.23	3.45E-04

4.5 Electrochemical characterization in NaCl electrolyte

4.5.1 DP1000

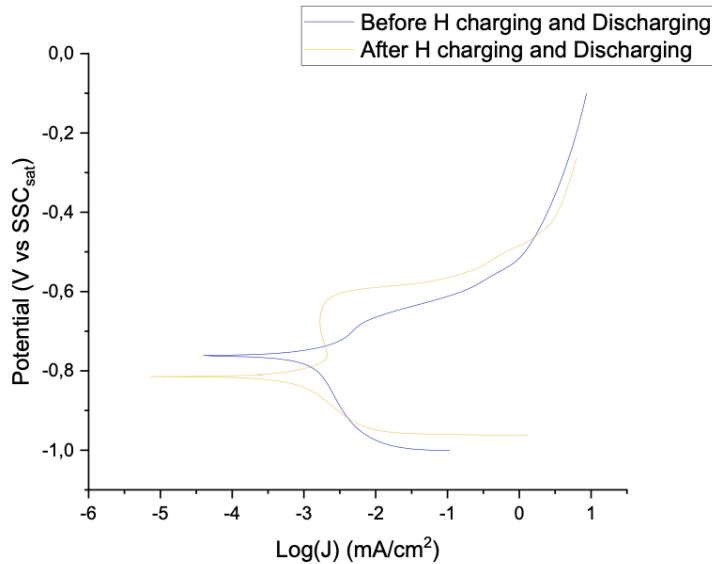


Figure 4.29: Potentiodynamic polarisation plots for DP1000 in 3.5 wt% NaCl before charging with H and after charging and discharging with H.

Figure 4.29 shows the corrosion behavior in 3.5wt% NaCl of DP1000 samples before charging with H and after charging with H. A noticeable difference is observed in the cathodic branches of the polarization curves. The material after being charged with H shows a higher cathodic current density in the applied potential range. Table 4.6 summarizes the polarization parameters obtained from the curves by Tafel extrapolation. The corrosion potential (E_{corr}) value is higher for the material after H charging compared to before H charging, which is also evident from the plot. The corrosion current density (i_{corr}) values are also higher for material after H charging compared to before H charging. However, the decrease in the corrosion rate observed for the sample after H charging is interesting and requires a more in-depth analysis of the role of other microstructural features (Chapter 5).

Both examples exhibit immediate passivation. However, at higher potentials, the samples indicate breakdown due to pitting in the case of the material after H charging, after the passive zone. The current density rises dramatically, suggesting that the passive coating has failed and a corrosion pit has formed on the exposed surface. In comparison, the region of passive behavior for materials prior to H charging is substantially narrower. It can be inferred that, the role of the oxide layer formed during H charging has a protective effect of the material. This will be further discussed.

Table 4.6: Potentiodynamic polarisation table for DP1000 in 3.5 wt% NaCl before charging with H and after charging and discharging with H

Material	Test	E_{corr} (mV vs SSCsat)	J_{corr} ($\mu\text{A}/\text{cm}^2$)	β_c (mV vs SSCsat)	β_a (mV vs SSCsat)	Corrosion rate (mmpy)
DP1000	Before H charging	-729.2±20.1	0.865±0.208	93.3±25.2	37.6±3.4	0.0245±0.0025
	After H charging	-800.3±13.8	0.454±0.151	91.6±14.0	66.5±6.0	0.017± 0.0056

4.5.2 Pure Iron

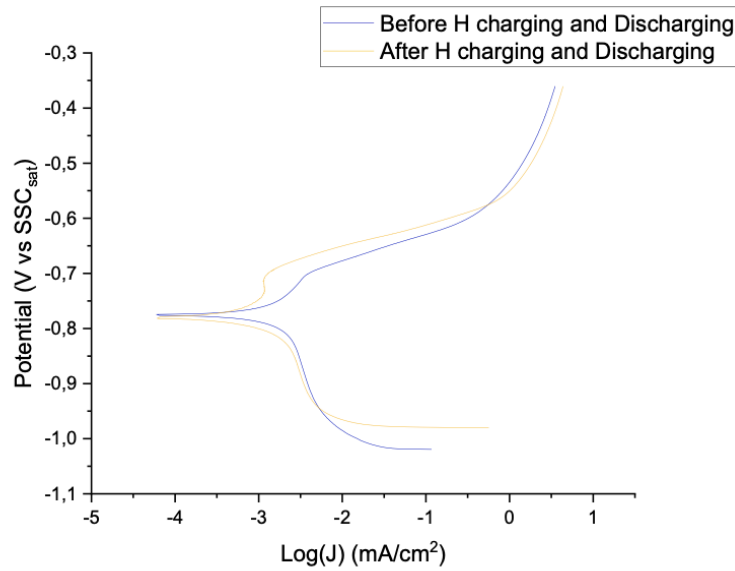


Figure 4.30: Potentiodynamic polarisation plots for Pure Iron in 3.5 wt% NaCl before charging with H and after charging and discharging with H.

Figure 4.30 shows the corrosion behavior in 3.5wt% NaCl of Pure Iron samples before charging with H and after charging with H. A noticeable difference is observed in the cathodic branches of the polarization curves. The material after being charged with H shows a higher cathodic current density in the applied potential range. In comparison, the anodic branches of the polarization curves overlap each other after the region of passivation.

Table 4.7 summarizes the polarization parameters obtained from the curves by Tafel extrapolation. The corrosion potential (E_{corr}) values for both cases are similar, which is also evident from the plot. The corrosion current density (i_{corr}) values are also similar for both cases. However, there is a slight decrease in the corrosion rate observed for the sample after H charging which is interesting and requires a more in-depth analysis of the role of other microstructural features (Chapter 5).

Both examples exhibit immediate passivation. However, the material after H is charged shows passivity at a lower current density compared with the material before H charging. At higher potentials, both the samples indicate breakdown due to pitting after the passive zone. The current density rises dramatically, suggesting that the passive coating has failed and a corrosion pit has formed on the exposed surface. The region of passive behavior for the material prior to H charging is substantially narrower compared to that of the material after H charging. It can be inferred that, the role of the oxide layer formed during H charging has a protective effect of the material. This will be further discussed.

Table 4.7: Potentiodynamic polarisation table for Pure Iron in 3.5 wt% NaCl before charging with H and after charging and discharging with H

Material	Test	E_{corr} (mV vs SSCsat)	i_{corr} ($\mu\text{A}/\text{cm}^2$)	β_c (mV vs SSCsat)	β_a (mV vs SSCsat)	Corrosion rate (mmpy)
Pure Iron	Before H charging	-774.2 ± 11.7	0.649 ± 0.172	194.5 ± 25.2	75.5 ± 19.8	0.0235 ± 0.0058
	After H charging	-779.6 ± 7.78	0.449 ± 0.346	67 ± 48.8	131.5 ± 12.3	0.017 ± 0.0020

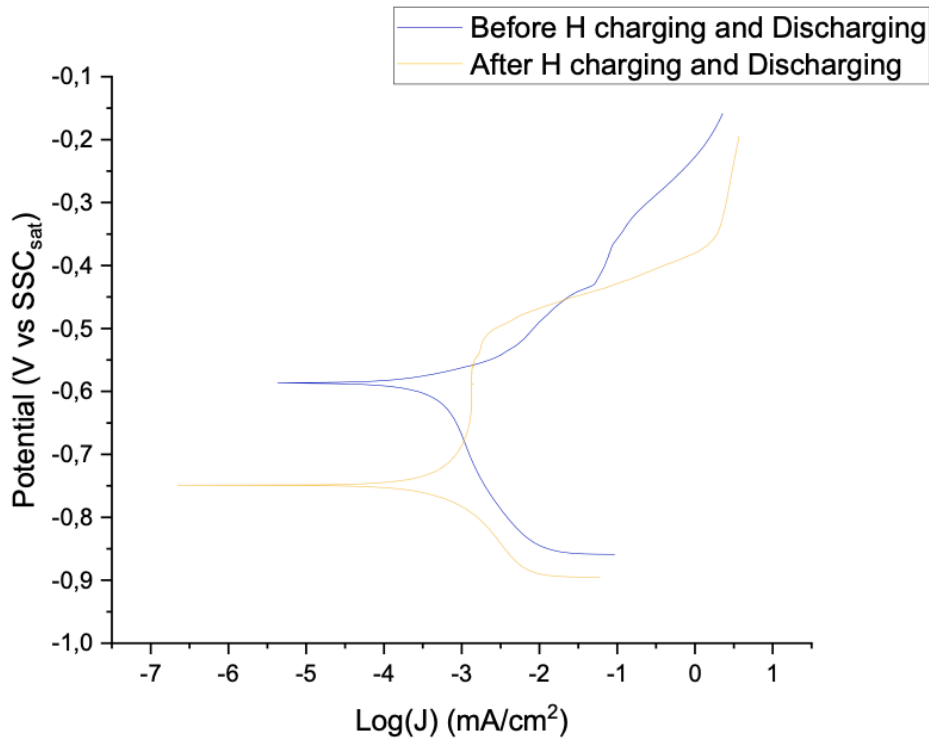


Figure 4.31: Potentiodynamic polarisation plots for AISI 420 in 3.5 wt% NaCl before charging with H and after charging and discharging with H.

4.5.3 AISI 420

Figure 4.31 shows the corrosion behavior in 3.5wt% NaCl of AISI 420 samples before charging with H and after charging with H. Table 4.6 summarizes the polarization parameters obtained from the curves by Tafel extrapolation. The corrosion potential (E_{corr}) value is higher for the material after H charging compared to before H charging, which is also evident from the plot. The corrosion current density (i_{corr}) values are lower for material after H charging compared to before H charging. However, the corrosion rates observed for both cases is similar. This is interesting and requires a more in-depth analysis of the role of other microstructural features (Chapter 5).

Both the cases show immediate passivation, as would be expected of martensitic stainless steel in 3.5 wt% NaCl. In the case of the material after H charging, after the passive region, at higher potentials, the samples show breakdown due to pitting. The current density increases drastically, indicating that the passive film has failed, and a corrosion pit has been formed on the exposed surface. In comparison, for the materials before H charging, the region of passive behaviour is much smaller.

Table 4.8: Potentiodynamic polarisation table for AISI 420 in 3.5 wt% NaCl before charging with H and after charging and discharging with H

Material	Test	E_{corr} (mV vs SSCsat)	J_{corr} ($\mu\text{A}/\text{cm}^2$)	β_c (mV vs SSCsat)	β_a (mV vs SSCsat)	Corrosion rate (mmpy)
AISI 420	Before H charging	-506.7 \pm 12.1	0.298 \pm 0.152	178.85 \pm 66.25	75.95 \pm 23.55	0.015 \pm 0.0049
	After H charging	-749.15 \pm 0.0	0.519 \pm 0.414	97.1 \pm 46.0	203.1 \pm 1.4	0.018 \pm 0.004

4.6 Scanning Kelvin Probe

SKP analyzed the surface potential of steel samples after charging for the three materials. Figures 4.32a, b and c shows the SKP maps for DP1000, Pure Iron and AISI 420, respectively, after 1 hour of H charging in 1 M NaOH + 8 g/L Thiourea.

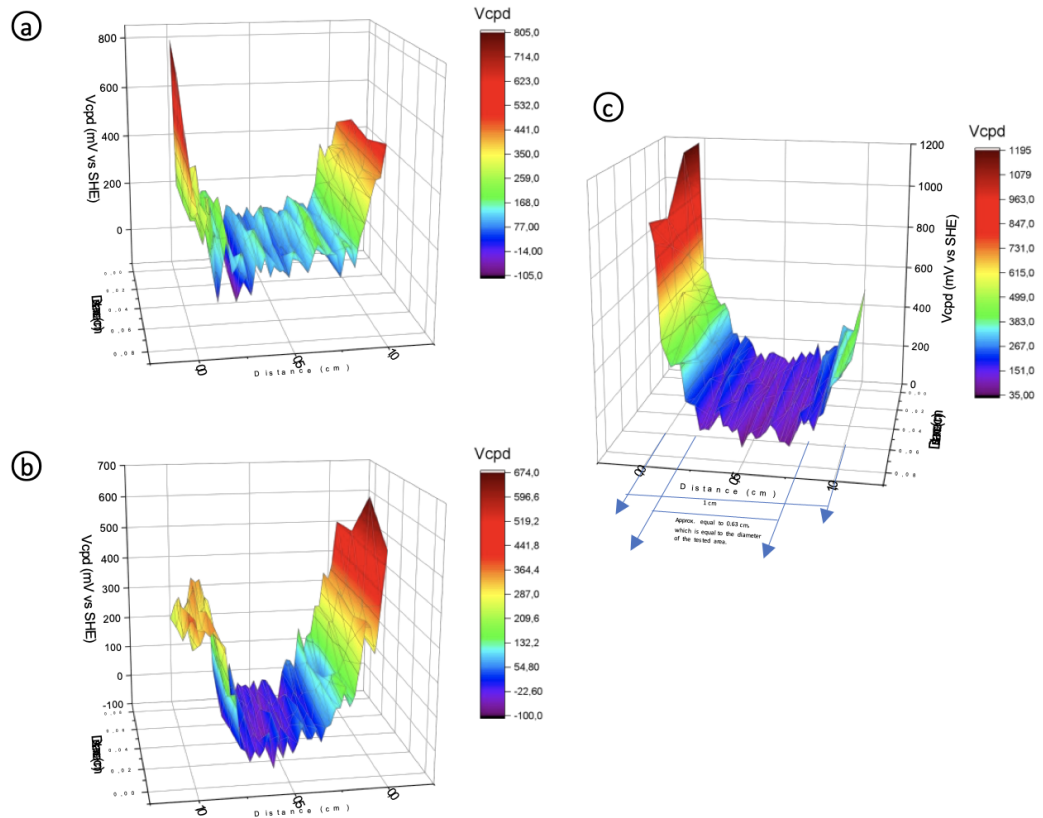


Figure 4.32: Map of Vcpd distribution on the surface of (a)DP1000, (b)Pure Iron and (c) AISI 420 samples that was locally charged with hydrogen, measured by SKP microscopy

As shown, a significant potential drop was observed at the centre of the specimen, relating to the area submitted to cathodic charging. The SKP maps show that lower contact potential difference spots appear in the area where Hydrogen was charged, and the contact potential difference of hydrogen-free surrounding areas remains unaffected. For each map, one line scan was extracted at the centre of the specimen across the low potential area. These profiles are compared in the figure showing an SKP line graph for the three materials. It can be observed that the area of low potential was approximate the same size as the charging area. Figure 4.33 shows the line scan of Vcpd distribution on the surface of (a)DP1000, (b)Pure Iron (PI) and (c) AISI 420 samples before and after H charging. It can be seen that the Vcpd is the highest for the AISI 420 material and similar for the DP1000 and Pure Iron material. The dip in Vcpd due to H charging, can be clearly visualized in the figure. In studies by Evers et al.[109] and Williams et al.[110], it was found that Hydrogen reduces parts of Fe^{3+} species and decreases the contact potential difference as the ratio of Fe^{3+} and Fe^{2+} species determines the work function of the specimen. Based on the literature, the atomic Hydrogen interacts with the air-formed iron oxide film reducing Fe^{3+} to Fe^{2+} species, thereby decreasing the oxide film thickness. This agrees with the thermochemical study of molecular hydrogen interaction with iron oxide, Fe_2O_3 . Additionally, the regions corresponding to the lowest Vcpd may relate to regions of localized corrosion. Additionally, it is possible to avoid the scatter is

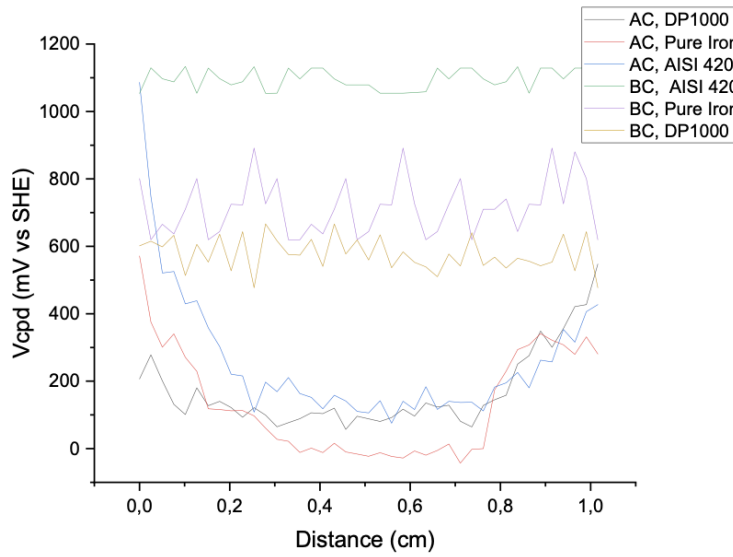


Figure 4.33: Line scan of V_{cpd} distribution on the surface of DP1000, Pure Iron (PI) and AISI 420 samples Before H Charging (BC) and After H Charging (AC), measured by SKP microscopy.

data seen in the figure 4.33 by the use of a Pd coating on the metal surface before and after H charging as has been used in literature to get less scatter on the SKP results. Due to the scatter in data, after H charging, it was not possible to compare the the three materials efficiently. Before H charging, the AISI 420 materials seems to have the highest potential followed by similar potentials for the Pure Iron and DP1000 material.

5

DISCUSSION

This chapter will discuss the results presented in Chapter 4, with the aim to relate these results to the research objectives proposed in the Introduction.

The Hydrogen charging experiments both with the active and the passivated surfaces reveal that in 1 hour, more Hydrogen is absorbed by the Pure Iron material, followed by the DP1000 material and then the AISI 420 material, (see figures 4.20 and 4.19). In the case of the passivated surface, the H desorption values for Pure Iron and DP1000 are comparable when including the standard deviation error. In the following section, the effect of material microstructure on the H/Material Interaction based on the results obtained will be discussed.

5.1 Active Metal

From the results, it was observed that the H desorbed after H charging for 1 hour was the most for the Pure Iron material, followed by the DP1000 material and then the AISI material. There are a few possible explanations for why this might be the case.

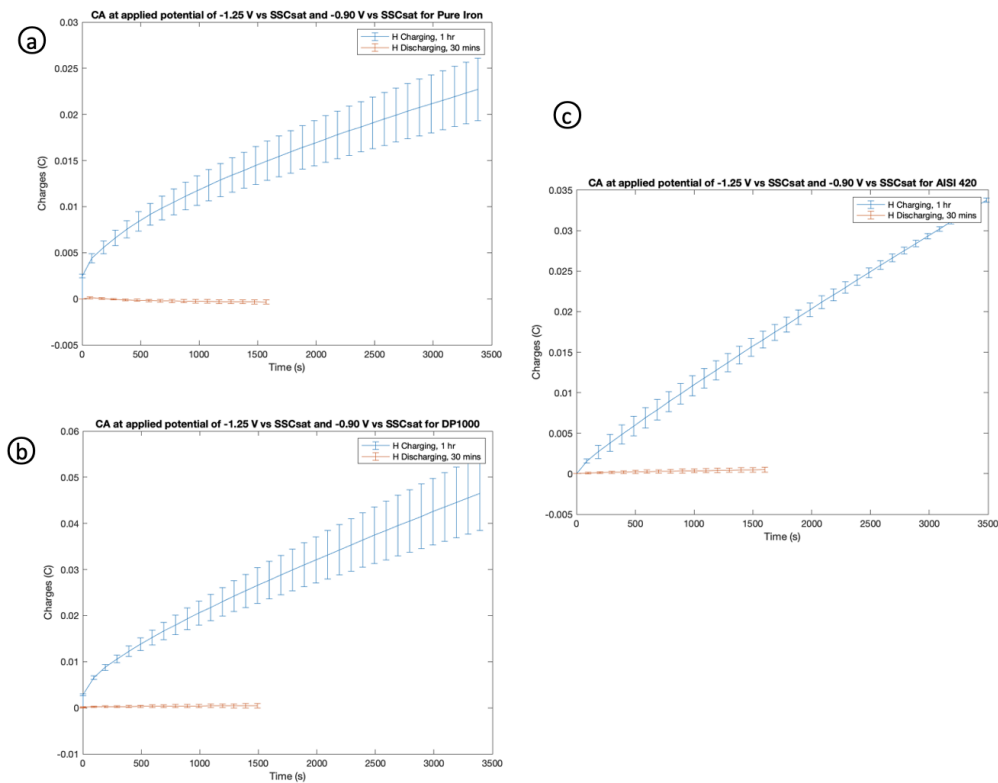


Figure 5.1: Comparison of charge density(C/cm^2) vs time(s) curves obtained after integrating current density vs time curves, for DP1000, Pure Iron and AISI 420 in 1 M NaOH + 8 g/L Thiourea.

To understand the H charging results, the charge density (C/cm^2) vs time(s) curves obtained after integrating the current density vs time curves were compared

for DP1000, Pure Iron and AISI 420 in 1 M NaOH + 8 g/L Thiourea. In figure 5.1, the current response, in this case, is connected mainly to the ab/adsorption of Hydrogen in steel and partly to the evolution reaction of hydrogen gas[102]. It can also be observed that after the H has been desorbed during the CV scan, relatively little charge is discharged during chronoamperometric discharging experiments, suggesting that there is not much Hydrogen in the metal that needs to be desorbed. The plot can be interpreted in the following way, the higher the charge/cm² values or larger the area under the curve, the more number of Hydrogen atoms did not get adsorbed into the material. The H charges that did not get adsorbed/absorbed by the metal show up as the charges on the plot. In this way Pure Iron has the most H ad/absorption, followed by DP1000 and then AISI 420, which has a very steep curve.

The blue curves indicating the charge density vs time after H charging is of interest. From figures 5.1 a,b and c, in the case of the pure iron sample, it can be seen that the curve reaches a constant value sooner than the Dual phase steel sample and the AISI 420 sample. In the case of the AISI 420 sample, the amount of charge increases steeply with charging duration; this could indicate that it takes the material longer for the same amount of H saturation as the other two materials.

Based on the results from the experiments conducted by Ozdirik[37] on As-Q martensitic steel, the experiments conducted by Encalada[127] on 304L Stainless steel and the results from this study (see figure 4.15), it was confirmed that compared to the Pure Iron and DP1000 material, the AISI 420 material takes much longer for the Hydrogen to saturate the matrix. It also suggests that the diffusion of H during the H charging step is the fastest in the case of the pure iron sample, followed by the Dual-phase sample and then the martensitic stainless steel sample.

There are a few possible reasons why the AISI 420 Material takes more time for H saturation. For this, the microstructure of the three materials has to be compared. Firstly, as discussed in the paper by Galindo et al.[128], H trapping sites such as dislocations strongly influence the overall hydrogen transport process in martensitic steels therefore, they take longer to saturate during charging and are released quickly during degassing. This might be why the H surface charge density (see figure 4.20) is the lowest in the case of the AISI 420 sample. Furthermore, a previous microstructure analysis by Crousen [118], on the same AISI 420 material used in this study showed the presence of martensitic lath boundaries and prior austenitic grain boundaries in the sample. In Literature, it was found that martensitic lath boundaries, prior austenitic grain boundaries and dislocations are sites where reversible H trapping can occur. Therefore it can be indirectly inferred that due to the presence of these trapping sites in the AISI 420 material, it takes longer for H saturation.

Additionally, in a paper by Hinds et al.[129] on AISI 410 steel, which has a similar composition to AISI 420 steel, it was discussed that reversible H trapping was attributed to dislocations. However, irreversible H trapping was believed to be considerable and most likely related to carbides. Now, traps can be reversible or irreversible in nature. Irreversible sites are characterized by high activation energies. The activation energy for an irreversible trap is high that of lattice diffusion. In fact the activation energy for an irreversible trap would be higher than the bond energy for the trap[71]. Carbide interfaces, solutes, precipitates and inclusions are examples for irreversible traps, where a large potential barrier has to be surpassed for the H to escape. Reversible H traps, on the other hand, have shallow energy barriers and detrapping is much easier. The reversibility of trapping sites is dependent on the temperature. Dislocations, grain boundaries, and microvoids are examples for reversible H traps. Between irreversible and reversible trap types, a differentiation is typically established. It is considered that hydrogen trapped in irreversible traps cannot participate in diffusion processes, but hydrogen held in reversible traps can[130]. Now, The XRD (see figure 4.3) of AISI 420 shows the presence of carbide phases in stainless steel. The carbides in the steel acting as irreversible trapping

sites could also be a reason for the AISI 420 steel having the least amount of H desorbed after H charging for 1 hour. A technique such as Thermal Desorption Analysis might have to be used to obtain the quantity of H trapped in these sites.

The presence of the air-formed Cr_2O_3 passive oxide layer on the AISI 420 steel, unlike the Pure Iron and DP1000 steel, might also inhibit the ingress of H into the steel. In a paper by Kuo et al.[131], it was observed that hydrogen permeation through passivated metals is mostly governed by the kinetic processes in the passive film and that hydrogen permeation through Cr_2O_3 film has a very low permeation rate and diffusivity. This might also explain why AISI 420 exhibits the lowest H desorption among the other materials investigated.

The DP1000 steel and the Pure Iron material can be compared as they have similar chemical compositions. There are high density of dislocations in the martensite phase structure of the DP1000 steel as a result of the trapped carbon during the diffusionless transformation[116]. Resulting in there being large residual stresses in the material. The microstructure is strained by carbon that becomes trapped in the crystal lattice during the martensitic transition. Through a reduction in the activation energy around the dislocations, increased strain and dislocation density speed up corrosion. By promoting atomic and ionic transport, this change in surface energy has an impact on chemical reactions. Furthermore, a previous study[116] on the same DP1000 material found that the stressed structure of the DP1000 steel lattice creates a less dense and more active surface, facilitating cathodic surface reactions such as the reduction of H, compared to the more relaxed ferrite phase.

It has been mentioned earlier that DP1000 steel has a two-phase microstructure consisting of ferrite and martensite. For instance, it has been mentioned in Literature[37] that for certain dual phase (DP) steel alloys, Hydrogen can be potentially trapped at phase boundaries, in addition to grain boundaries, dislocations, and lattice vacancies. This could mean that there are more available trapping sites for the DP1000 material compared to the Pure Iron material, which has a pure ferrite microstructure and a similar composition. Due to there being more trapped H compared to diffusible mobile H in the DP1000 material, the amount of H that is available for desorption is likely lesser. This can be seen in 4.20. The presence of the trapping site might also reduce the rate of H entry and exit from the steel. The presence of the retained austenite phase, as indicated by the XRD of DP1000 (see figure 4.2), also affects the H desorption from the steel. In a paper by Park et al.[132], it was found that the retained austenite phase exhibited low H diffusivity and high H solubility. Moreover, the Retained austenite phase acts as a substantial high-temperature bulk hydrogen trap in high-strength steel welds. These trapping sites make the desorption of H from the steel much slower due to the requirement for higher activation energy.

Pure Iron consists mainly of the ferrite phase. The Literature[133] in this study shows that this phase can be considered to have reversible hydrogen traps such as dislocations, vacancies and voids. Additionally, due to the high hydrogen diffusion coefficient in ferrite even at room temperature, the absorbed Hydrogen desorbs quickly from the steel([37]).

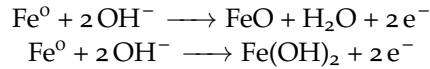
5.2 Passive Oxide

5.2.1 H Charging and Discharging

The sample surface changes continuously during a CV scan due to the formation and breakdown of oxide films on the surface. Ion exchange across the films is influenced by the steric hindrance provided by the oxide film[134].

Various iron oxide compounds have been reported to be present in the passive film on the surface of Iron. These include hematite ($\alpha\text{-Fe}_2\text{O}_3$), maghemite ($\gamma\text{-Fe}_2\text{O}_3$),

magnetite (Fe_3O_4), goethite ($\alpha\text{-FeOOH}$), akaganeite ($\beta\text{-FeOOH}$), lepidocrocite ($\gamma\text{-FeOOH}$) and feroxyhyte ($\delta\text{-FeOOH}$)[135]. Among the oxides mentioned, it was possible to identify the presence of feroxyhyte ($\delta\text{-FeOOH}$) in the XRD of the Pure Iron and DP1000 materials after the charging process. It can then be directly concluded that the main oxidation processes contributing to the peak a1 in the CV scans for Pure Iron and DP1000 are either of the two reactions below,



and the main oxidation processes contributing to the peak a2 in the CV scans for Pure Iron and DP1000 is the reaction below,



It is also possible from the CV results obtained in this work that the surface film is composed of a two-layer structure in which the inner part is Fe_3O_4 , and the outer part is the oxidised or reduced feroxyhyte ($\delta\text{-FeOOH}$). However, the Fe_3O_4 layer was not clearly indicated in the diffraction patterns of the material. Possibly, due to the volume fraction of Fe_3O_4 being lower than the detection limit.

The decrease in desorbed Hydrogen in the case of samples with Hydrogen charged on the passive oxide surface is most likely due to a change in the ion transport mechanism caused by the formation of an oxide layer, as shown schematically in figure 5.2. In the case of Pre-conditioning B, the oxide layer that forms between the metal and the electrolyte during the anodic sweep of the CV scan is not reduced, thereby changing the ion transfer path and the electrical double layer between the metal and the solution. Ions pass through three transport processes in the presence of an oxide layer: the oxide-electrolyte interface, the oxide film itself, and the metal-oxide interface. Any of these three transport processes can act as the rate-determining reaction. Furthermore, the formed oxide layer can have many microstructural imperfections and, in some cases, can even be amorphous, influencing ion migration. If the oxide layer formed is amorphous, it would not necessarily be easily identifiable on the XRD tests[23].

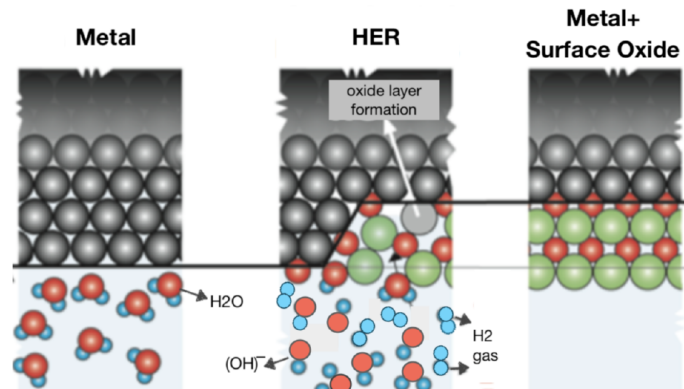


Figure 5.2: Schematic representation of the oxide layer formation on the metal surface during HER, adapted from [23]. The light blue color corresponds to the electrolyte.

A study by Bruzozni et al.[136] reported their results for the entry of H through the passive film on Iron. They suggested that in the case of metal with a passive oxide layer, the rate-determining step for hydrogen permeation is the passage through the film instead of the passage through an interface (oxide/electrolyte or metal/oxide). Additionally, in a paper by Swansiger et al.[137] on the H permeation properties of stainless steel, they reported that a portion of the oxide was functioning very well as a barrier and allowing almost no hydrogen to infiltrate. While some of the oxide was broken or flawed, providing hydrogen access to a smaller portion of the substrate.

From the results of the CV scans in the present study, it can be observed that for the Pure Iron sample and the DP1000 sample, the CV curves are highly similar, including their current response values. Furthermore, the XRD diffractograms are similar after charging for both materials. From this, it can be concluded that the composition of the oxide film on Pure Iron and DP1000 are alike. Furthermore, the values of H desorbed by the materials are also close, especially considering the measurement standard deviation error (see figure 4.20). As mentioned earlier, assuming that the oxide film controls the entry of H into the steel instead of the interface effects, it would make sense that the values of H desorbed by the materials are similar.

The AISI 420 material, on the other hand, has the most negligible value of H desorbed. Again assuming that the oxide film controls the entry of H into the steel instead of the interface effects. Cr is likely present in the passive layer of the stainless steel. Even though the Cr oxide layer was not induced during the CV scan, the air-formed Cr oxide layer is likely present on the metal surface. The XRD results for AISI 420 after H charging do not indicate the presence of a Cr oxide layer, but the layer might be beyond the detectable limits of the XRD instrument. In a publication on the retarding mechanism of thermally grown oxide films on hydrogen embrittlement of AISI 430 stainless steel, Yen et al. showed a direct relationship between the amount of hydrogen entrance retardation and the amount of chromium in the oxide coating[138].

For the passive behaviour, defectivity and composition of the passive film play an important role in the H entry and exit behaviour.

In summary, from the present results, in the absence of a significant passive oxide layer (Active surface, Pre-conditioning A), the H desorption from the materials can be governed by reversible and irreversible H trapping sites in the steel. On the other hand, in the presence of a passive oxide film (Pre-conditioning B), the oxide layer properties can be assumed to govern the H entry and exit. However, from the results obtained in this study, additional investigations are necessary to completely isolate the effects of the oxide layer and the base microstructure on H charging.

5.2.1.1 Effect of Hydrogen charging/discharging on the metal/electrolyte interface

The passive film layer of the ferrite-martensite microstructure of DP1000 has fewer protective barrier capabilities in a passive NaOH environment. The more defective passive film generated on the substrate microstructure is connected to the inferior barrier characteristics of the ferrite-martensite microstructure[116]. This can be seen in the EIS graphs (figures 4.21 and 4.26) for DP1000.

Additionally, from the tables showing the EIS fitting parameters (tables 4.4 and 4.5), it can be seen that some of the capacitance (C_1 and C_2) values are too large ($>100 \text{ mF/cm}^2$). This might be due to the real surface area with the roughness introduced by oxide layer being very large. Relatively high values ($1-100 \text{ mF/cm}^2$), usually correspond to the oxidation–reduction process on a highly subdivided surface texture as reported by Joiret et al.[139]. Analysis of impedance data shows that after Hydrogen charging the charge transfer resistance decreased significantly.

The oxidation and reduction of Fe(II) to Fe(III) and vice-versa cause lattice expansion on the passive layer due to the variation in size between the Fe(II) and Fe(III) ions, resulting in the decrease in the stability of the passive film ([140], [141]). From Literature and further supported by the EIS experiments in this study, it can be seen that H charging has affected the stability of the passive layer.

Overall, from all the Bode plots in the study, it can be seen that the AISI 420 material has the highest $|Z|$ value at 0.01 Hz, followed by DP1000 and Pure Iron. Therefore, the AISI 420 material has the best passive layer barrier properties, followed by DP1000 and Pure Iron. From the CV results, it was possible to determine that Pure Iron had the highest value for H desorption, followed by DP1000 and then

AISI 420. Comparing the EIS and the CV results, it can be said the lower barrier properties of the passive layer on Pure Iron facilitated higher H adsorption and desorption, and the higher barrier properties of the passive layer on AISI 420 facilitated lower H adsorption and desorption. Nonetheless, it was only possible to compare the barrier properties of the passive layer on the three materials, and obtained in this study, additional investigations are necessary to isolate the effect of H charging across the three materials.

5.3 Influence of Hydrogen Charging on the corrosion Properties of the investigated steels

Recent studies[142] revealed that hydrogen, a consequence of the corrosion reaction, significantly affects the composition and structure of passive films, increasing their sensitivity to pitting and decreasing their resistance to corrosion. There is considerable debate over why hydrogen makes passive films more vulnerable to pitting.

The propensity of H to destabilize the passive film generated on the metal has historically been used as an explanation for the enhanced corrosion of steels that have been charged with H[143]. However, in the present study, the results in section 4.5 indicate otherwise. It can be seen from figures 4.29, 4.31 and 4.30 that far from increasing the corrosion rate of the materials, the corrosion resistance of the material seems to have actually improved. For all three materials, after H Charging in NaOH with Thiourea in the NaCl electrolyte, the passive behaviour starts at a lower current density and seems much more stable. Now, there are some reasons why this might be the case. First, it is possible that when the NaOH (with Thiourea) electrolyte was replaced with the NaCl electrolyte, the mobile diffusible H might have escaped from the material. However, the time taken for replacing the electrolyte was always in the range of 2-3 minutes, so it is doubtful if a lot of H would have actually escaped. Second, in the NaCl experiments, the samples were directly charged with H using the chronoamperometric charging step without preparing the surface using the CV step. So, the H for all three materials were charged into the air formed oxides and the oxides formed due to immersion in the alkaline NaOH electrolyte on the surface of the materials. It is possible that the Hydrogen charged is too low to show any appreciable effect on the metals, and the positive effect on the corrosion resistance is due to the passive layers formed on the metals.

6 | CONCLUSIONS

The conclusions are presented based on the research questions in the Introduction Chapter.

The electrochemical approach, made up of the chronoamperometric and cyclic voltammetry techniques, has proven to be an effective tool for analyzing hydrogen sorption on metal surfaces at a lab scale. This approach demonstrated many benefits and some disadvantages, including,

- Once the conditions and parameters of the electrochemical experiment are clearly defined, such as a stable reference electrode (RE) at the operating pH and consistency in the electrolytic set-up configuration (constant distance between the electrodes), the same sample surface preparation each time, good reproducibility is possible.
- We were able to determine a trend in the sensitivity to hydrogen intake of several materials using the electrochemical method. In addition, the cyclic voltammetry method creates accelerated circumstances for studying H/material interaction as opposed to the hydrogen gas-metal interaction that occurs in the actual world at atmospheric pressure on a longer time-scale.
- A clear determination of the amount of hydrogen desorbed is made difficult by the overlap in peaks caused by the vicinity of the hydrogen oxidation potential (desorption peak a1') and the iron oxidation peaks (a1 and a2).
- Despite the fact that electrochemical methods were successful in detecting and measuring the amount of hydrogen adsorbed. However, the results of quantifying the H desorption peak are influenced by the experimental design (choice of potential range) and the volume of hydrogen developed in the sample. Despite this, the approach enables comparison of the many tested materials and offers a gauge of hydrogen susceptibility.

Some general conclusions regarding the H desorption trends in the active and passive surface,

- In the case of an Active surface, among the alloys tested, AISI 420 martensitic Stainless Steel has the lowest amount of diffusible hydrogen. It was indirectly concluded that the diffusible hydrogen measured in AISI 420 steel mostly comes from the dislocations among the other microstructural constituents such as martensitic lath boundaries, prior austenitic grain boundaries and carbide phases. The presence of an air-formed Cr oxide layer also inhibits the H ab/adsorption to a certain extent. In Pure Iron, the diffusible hydrogen measured mainly comes from the ferrite phase as well as other microstructural constituents such as interstitial sites, grain boundaries and dislocations. In DP1000, the diffusible hydrogen measured mainly comes from the phases (ferrite and martensite), phase boundaries and other microstructural constituents such as interstitial sites, grain boundaries and dislocations. The presence of retained austenite phase also contributes to the diffusible H. Considering all the results in the present study and literature; it can be indicated that the fraction of fast disappearing kind of hydrogen (mobile hydrogen) in Pure Iron is relatively higher than in the other alloys. Followed by the DP1000 material and then the AISI 420 material. The value of H desorbed in Pure Iron is approximately 44% higher than the DP1000 steel and 48% higher than the AISI 420 steel.

- In the case of a Passive surface, among the alloys tested, AISI 420 martensitic Stainless Steel still has the lowest amount of diffusible hydrogen compared to the Pure Iron material and the DP1000 material. In the case of the materials with passive films, the H entry and exit mechanisms are dominated by the effect of the oxide layer. It has been established in the present study that Pure Iron and DP1000 material have oxide films that are primarily similar in composition. Hence, the CV results also agree that the value for H desorbed is similar for Pure Iron and DP1000, with the Pure Iron having a slightly higher value, not including the error. The oxide layers on the AISI 420 have the addition of Cr oxide, which separates it from the other two materials. The oxide layer on the AISI material seems to provide a higher H retarding effect than the oxide layers on the other two materials. Considering all the results in the present study and literature, it can be indicated that the value of hydrogen (mobile hydrogen) desorbed in Pure Iron is similar to the DP1000 material and significantly higher than the AISI 420 material. The value of H desorbed in Pure Iron is approximately 12% higher than the DP1000 steel and 85% higher than the AISI 420 steel.

While the EIS technique was useful in identifying a trend between the barrier properties of the passive layer and the H desorption values for the three materials, it was impossible to isolate the effect of H charging across the three materials. The trend showed that a lowering in the barrier properties of the passive layer corresponded to an increase in the H desorption values.

Potentiostatic Polarization tests, which were introduced as a technique to gauge the impact of H charging and discharging on the investigated materials in 3.5wt% NaCl, were not able to clearly identify the effect of H on the corrosion properties of the three materials.

Scanning Kelvin Probe was introduced as a technique to study the effect of Hydrogen charging on the air and alkaline electrolyte-formed passivity of Pure Iron, DP1000 and AISI 420 stainless steel. It was shown that in the materials after Hydrogen charging in 1 M NaOH aqueous electrolyte (With 8 g/L Thiourea) for 1 hour, a potential well was generated locally corresponding to the H charged area. The Volta potential at the site of detection dropped as a result of hydrogen partially reducing the surface oxide coating and adsorbing oxygen. Due to the scatter in data, after H charging, it was not possible to compare the the three materials efficiently.

7

RECOMMENDATIONS AND OUTLOOK

The following suggestions can help to gain a greater knowledge of the mechanism underlying the surface and microstructural changes caused by the interaction of hydrogen with metals:

- Mott-Schottky analysis can be done to understand the effect of Hydrogen charging on the semiconductive properties of passive-oxide properties of the Iron-based alloys in this study. Gaining an understanding of the semi-conductive properties can help in making the alloys more resistant to corrosion.
- It would be useful to characterise the oxide layer formed on the bare metals after the Hydrogen charging step used in the study, e.g. by X-ray photoelectron spectroscopy (XPS) or Auger Electron Spectroscopy (AES).
- To use thermal desorption spectroscopy (TDS) to determine the varieties and amounts of traps that are present in the bulk material . TDS can also be considered as a substitute approach for measuring adsorbed hydrogen.
- In-situ experiments, with respect to Fourier Transform Infrared Spectroscopy (FTIR) can be performed to better understand the Thiourea related oxidation peaks formed on the iron-based alloys under study.
- To gain more clarity, quantifying the contribution of the oxide layer to hydrogen adsorption might be done by using ab-initio calculations on the trapping of hydrogen by oxides.
- Modifying the microstructure of the materials by heat treatment to reduce the trapping of Hydrogen in the alloy matrix and following up with mechanical testing can be the next step to improve the performance of the materials.
- Hydrogen permeation experiments using the double cell permeation method proposed by Devanathan et al. can be used to find Hydrogen Permeation curves (i_{∞} hydrogen flux vs time) that can provide information such as the diffusion coefficient(D), the steady-state permeation rate , and the trapping behaviour of hydrogen in the steel, the charging concentration of hydrogen etc.
- To do a cross-sectional analysis of the sample material to investigate hydrogen diffusion from surface to bulk using techniques such as Scanning Kelvin Probe (SKP) or Scanning Kelvin Probe Force Microscopy (SKPFM).
- With respect to the electrochemical procedures used in the study, it can be fine-tuned to a greater extent to get better results. For instance, it might be interesting to perform the EIS right after the chronoamperometric H charging step, to isolate the effect H charging has on the metal.

BIBLIOGRAPHY

- [1] M. Nagumo, "Function of hydrogen in embrittlement of high-strength steels," *ISIJ international*, vol. 41, no. 6, pp. 590–598, 2001.
- [2] G. Krauss, *Steels: processing, structure, and performance*. Asm International, 2015.
- [3] J. Chen, M. Y. Lv, S. Tang, Z. Y. Liu, and G. D. Wang, "Low-carbon bainite steel with high strength and toughness processed by recrystallization controlled rolling and ultra fast cooling (rcr+ ufc)," *Isij International*, vol. 54, no. 12, pp. 2926–2932, 2014.
- [4] N. Ridley, "A review of the data on the interlamellar spacing of pearlite," *Metallurgical and Materials Transactions A*, vol. 15, no. 6, pp. 1019–1036, 1984.
- [5] I. Razumov, Y. N. Gornostyrev, and M. Katsnelson, "Towards the ab initio based theory of phase transformations in iron and steel," *Physics of Metals and Metallography*, vol. 118, no. 4, pp. 362–388, 2017.
- [6] Q. Liu, Q. Zhou, J. Venezuela, M. Zhang, J. Wang, and A. Atrens, "A review of the influence of hydrogen on the mechanical properties of dp, trip, and twip advanced high-strength steels for auto construction," *Corrosion Reviews*, vol. 34, no. 3, pp. 127–152, 2016.
- [7] C. LibreTexts, "20.8: Corrosion," Jul 2020.
- [8] S. for life, "Corrosion of structural steel." https://www.steelconstruction.info/Corrosion_of_structural_steel, May 2013. Accessed: 2020-09-30.
- [9] C. McMahon, "Structural materials: a textbook with animations," ch. 1, pp. "1–12", Merion Books, 2004.
- [10] "Passivity," in *Engineering Materials and Processes*, pp. 53–63, Springer London.
- [11] E. E. Stansbury and R. A. Buchanan, *Fundamentals of electrochemical corrosion*. ASM international, 2000.
- [12] K. Yanagisawa, T. Nakanishi, Y. Hasegawa, and K. Fushimi, "Passivity of dual-phase carbon steel with ferrite and martensite phases in ph 8.4 boric acid-borate buffer solution," *Journal of the Electrochemical Society*, vol. 162, no. 7, p. C322, 2015.
- [13] E. Protopopoff and P. Marcus, "Surface effects on hydrogen entry into metals," *CORROSION TECHNOLOGY-NEW YORK AND BASEL-*, vol. 17, pp. 53–96, 2002.
- [14] G. Caskey Jr, "Hydrogen effects in stainless steel," tech. rep., Du Pont de Nemours (EI) and Co., 1983.
- [15] S. Lynch, "Hydrogen embrittlement phenomena and mechanisms," *Corrosion reviews*, vol. 30, no. 3-4, pp. 105–123, 2012.
- [16] M. M. Salleh, A. M. Al Bakri, A. Abdullah, and H. Kamarudin, "Failure modes of hydrogen damage on metal tubes," *Australian Journal of Basic and Applied Sciences*, vol. 7, no. 5, pp. 329–335, 2013.

- [17] S. K. Dwivedi and M. Vishwakarma, "Effect of hydrogen in advanced high strength steel materials," *international journal of hydrogen energy*, vol. 44, no. 51, pp. 28007–28030, 2019.
- [18] E. Legrand, J. Bouhattate, X. Feaugas, and H. Garmestani, "Computational analysis of geometrical factors affecting experimental data extracted from hydrogen permeation tests: li-consequences of trapping and an oxide layer," *international journal of hydrogen energy*, vol. 37, no. 18, pp. 13574–13582, 2012.
- [19] N. Elgrishi, K. J. Rountree, B. D. McCarthy, E. S. Rountree, T. T. Eisenhart, and J. L. Dempsey, "A practical beginner's guide to cyclic voltammetry," *Journal of chemical education*, vol. 95, no. 2, pp. 197–206, 2018.
- [20] G. Schimo, W. Burgstaller, and A. W. Hassel, "Rolling direction dependent diffusion coefficients of hydrogen in ferritic steel by sdcm charging and skp probing," *ISIJ International*, vol. 56, no. 3, pp. 487–491, 2016.
- [21] BioLogic, "Skp101: An introduction to scanning kelvin probe," Dec 2021.
- [22] A. Yilmaz, C. Ozkan, J. Sietsma, and Y. Gonzalez-Garcia, "Properties of passive films formed on ferrite-martensite and ferrite-pearlite steel microstructures," *Metals*, vol. 11, no. 4, p. 594, 2021.
- [23] H.-H. Strehblow, V. Maurice, and P. Marcus, "Passivity of metals," *Corrosion mechanisms in theory and practice*, pp. 235–326, 2011.
- [24] G. Krauss, "Microstructure and transformations in steel," *Materials Science and Technology*, 2006.
- [25] P. Chakraborti and M. Mitra, "Microstructure and tensile properties of high strength duplex ferrite–martensite (dfm) steels," *Materials Science and Engineering: A*, vol. 466, no. 1-2, pp. 123–133, 2007.
- [26] W. H. Johnson, "Ii. on some remarkable changes produced in iron and steel by the action of hydrogen and acids," *Proceedings of the Royal Society of London*, vol. 23, no. 156-163, pp. 168–179, 1875.
- [27] P. Blanchard and A. Troiano, "Embrittlement of metals by hydrogen. influence of the crystallographic and electronic structure," *Mem. sci. rev. met.*, vol. 57, 1960.
- [28] R. Latanision and H. Opperhauser, "The intergranular embrittlement of nickel by hydrogen: the effect of grain boundary segregation," *Metallurgical Transactions*, vol. 5, no. 2, pp. 483–492, 1974.
- [29] M. O. Speidel, "Hydrogen embrittlement of aluminum alloys," *Hydrogen in metals*, pp. 274–276, 1974.
- [30] R. Oriani, "Hydrogen embrittlement of steels," *Annual review of materials science*, vol. 8, no. 1, pp. 327–357, 1978.
- [31] H. Hrdinová, V. Kreibich, J. Kudláček, and J. Horník, "Hydrogen embrittlement after surface treatments," in *International Scientific-Technical Conference MANUFACTURING*, pp. 266–275, Springer, 2019.
- [32] A. Turnbull, "Hydrogen diffusion and trapping in metals," in *Gaseous hydrogen embrittlement of materials in energy technologies*, pp. 89–128, Elsevier, 2012.
- [33] T. Carter and L. Cornish, "Hydrogen in metals," *Engineering Failure Analysis*, vol. 8, no. 2, pp. 113 – 121, 2001.

- [34] S. K. Bonagani, B. Vishwanadh, S. Tenneti, N. N. Kumar, and V. Kain, "Influence of tempering treatments on mechanical properties and hydrogen embrittlement of 13 wt% cr martensitic stainless steel," *International Journal of Pressure Vessels and Piping*, vol. 176, p. 103969, 2019.
- [35] Q. Liu, Q. Zhou, J. Venezuela, M. Zhang, and A. Atrens, "Hydrogen concentration in dual-phase (dp) and quenched and partitioned (q&p) advanced high-strength steels (ahss) under simulated service conditions compared with cathodic charging conditions," *Advanced Engineering Materials*, vol. 18, no. 9, pp. 1588–1599, 2016.
- [36] R. Agrawal and T. Nambodhiri, "The inhibition of corrosion and hydrogen embrittlement of aisi 410 stainless steel," *Journal of applied electrochemistry*, vol. 22, no. 4, pp. 383–389, 1992.
- [37] B. Ozdirik, T. Depover, L. Vecchi, K. Verbeken, H. Terryn, and I. De Graeve, "Comparison of electrochemical and thermal evaluation of hydrogen uptake in steel alloys having different microstructures," *Journal of The Electrochemical Society*, vol. 165, no. 11, p. C787, 2018.
- [38] J. Malina, A. Begičhadžipašić, and Š. Nižnik, "Electrochemical corrosion and hydrogen diffusivity in dual phase steel," *Zaštita materijala*, vol. 54, no. 2, pp. 130–134, 2013.
- [39] H. Bhadeshia and R. Honeycombe, *Steels: microstructure and properties*. Butterworth-Heinemann, 2017.
- [40] D. Jack and K. Jack, "Invited review: carbides and nitrides in steel," *Materials Science and Engineering*, vol. 11, no. 1, pp. 1–27, 1973.
- [41] L. Toth, *Transition metal carbides and nitrides*. Elsevier, 2014.
- [42] "Austenite martensite bainite pearlite and ferrite structures." <https://www.twi-global.com/technical-knowledge/faqs/faq-what-are-the-microstructural-constituents-austenite-martensite-bainite-pearlite-and-ferrite>. Accessed: 2020-09-30.
- [43] C. Burnett, "What is stainless steel?," Feb 2014.
- [44] "Ferritic stainless steel: A useful overview of ferritic steel grades."
- [45] T. Stainless, "Practical guidelines for the fabrication of duplex stainless steels; international molybdenum association (imoa): London, uk, 2014," *Google Scholar*.
- [46] "Advanced high-strength steel (ahss) definitions," Jul 2021.
- [47] N. Fonstein, "Arcelormittal global r&d, east chicago labs, united states," *Automotive Steels: Design, Metallurgy, Processing and Applications*, p. 169, 2016.
- [48] A. D. McNaught, A. Wilkinson, *et al.*, *Compendium of chemical terminology*, vol. 1669. Blackwell Science Oxford, 1997.
- [49] X. G. Zhang, *Passivation and Surface Film Formation*, pp. 65–91. Boston, MA: Springer US, 1996.
- [50] K. Morshed-Behbahani, N. Zakerin, P. Najafisayar, and M. Pakshir, "A survey on the passivity of tempered aisi 420 martensitic stainless steel," *Corrosion Science*, vol. 183, p. 109340, 2021.

- [51] S. Vafaeian, A. Fattah-alhosseini, M. K. Keshavarz, and Y. Mazaheri, "Simultaneous investigation of the effect of advanced thermomechanical treatment and repetitive cyclic voltammetry on the electrochemical behavior of aisi 430 ferritic stainless steel," *Journal of Materials Engineering and Performance*, vol. 26, no. 2, pp. 676–684, 2017.
- [52] J. Feng, *Characterization of native oxide and passive film on iron and iron-chromium alloy*. PhD thesis, University of Cincinnati, 2014.
- [53] Corrosionpedia, "What is a flade potential? - definition from corrosionpedia," Aug 2018.
- [54] L. Wegrelius, F. Falkenberg, and I. Olefjord, "Passivation of stainless steels in hydrochloric acid," *Journal of the Electrochemical Society*, vol. 146, no. 4, p. 1397, 1999.
- [55] A. Fattah-alhosseini and K. Babaei, "The influence of grain refinement on the semiconducting properties of passive films formed on ferritic stainless steels: A review," *Anal. Bioanal. Electrochem.*, vol. 11, no. 12, pp. 1747–1769, 2019.
- [56] Q. Guo, J. Liu, M. Yu, and S. Li, "Effect of passive film on mechanical properties of martensitic stainless steel 15-5ph in a neutral nacl solution," *Applied Surface Science*, vol. 327, pp. 313–320, 2015.
- [57] H. S. Abdo, A. H. Seikh, J. A. Mohammed, M. Luqman, S. A. Ragab, and S. M. Almotairy, "Influence of chloride ions on electrochemical corrosion behavior of dual-phase steel over conventional rebar in pore solution," *Applied Sciences*, vol. 10, no. 13, p. 4568, 2020.
- [58] A. B. Chwang and C. D. Frisbie, "Temperature and gate voltage dependent transport across a single organic semiconductor grain boundary," *Journal of Applied Physics*, vol. 90, no. 3, pp. 1342–1349, 2001.
- [59] N. Sato *Electrochim. Acta*, vol. 16, p. 1909, 1971.
- [60] A. Barbucci, G. Cerisola, and P. Cabot, "Effect of cold-working in the passive behavior of 304 stainless steel in sulfate media," *Journal of the Electrochemical Society*, vol. 149, no. 12, p. B534, 2002.
- [61] I. Bösing, L. Cramer, M. Steinbacher, H. W. Zoch, J. Thöming, and M. Baune, "Influence of heat treatment on the microstructure and corrosion resistance of martensitic stainless steel," *AIP Advances*, vol. 9, no. 6, p. 065317, 2019.
- [62] S. Jin and A. Atrens, "Esca-studies of the structure and composition of the passive film formed on stainless steels by various immersion times in 0.1 m nacl solution," *Applied Physics A*, vol. 42, no. 2, pp. 149–165, 1987.
- [63] F. Besenbacher, P. Sprunger, L. Ruan, L. Olesen, I. Stensgaard, and E. Lægsgaard, "Direct observations of changes in surface structures by scanning tunneling microscopy," *Topics in Catalysis*, vol. 1, no. 3-4, pp. 325–341, 1994.
- [64] T. Perng and J. Wu, "A brief review note on mechanisms of hydrogen entry into metals," *Materials Letters*, vol. 57, no. 22-23, pp. 3437–3438, 2003.
- [65] J. Bockris, J. McBreen, and L. Nanis, "The hydrogen evolution kinetics and hydrogen entry into a-iron," *Journal of the Electrochemical Society*, vol. 112, no. 10, p. 1025, 1965.
- [66] K. Vetter, "Electrochemical kinetics: Theoretical and experimental aspects, academic press," *New York.*, 1967.
- [67] M. Nagumo, *Fundamentals of hydrogen embrittlement*, vol. 921. Springer, 2016.

- [68] E. J. Song, H. Bhadeshia, and D.-W. Suh, "Effect of hydrogen on the surface energy of ferrite and austenite," *Corrosion science*, vol. 77, pp. 379–384, 2013.
- [69] M. Luppo and J. Ovejero-Garcia, "The influence of microstructure on the trapping and diffusion of hydrogen in a low carbon steel," *Corrosion science*, vol. 32, no. 10, pp. 1125–1136, 1991.
- [70] A. McNabb and P. Foster, "A new analysis of diffusion of hydrogen in iron and ferritic steels," *Transactions of the Metallurgical Society of AIME*, vol. 227, no. 3, p. 618, 1963.
- [71] S. Li, C. Chen, Y. Liu, H. Yu, and X. Wang, "Influence of surface martensite layer on hydrogen embrittlement of fe-mn-c-mo steels in wet h₂s environment," *International Journal of Hydrogen Energy*, vol. 43, no. 34, pp. 16728–16736, 2018.
- [72] K. Kiuchi and R. McLellan, "The solubility and diffusivity of hydrogen in well-annealed and deformed iron," *Perspectives in Hydrogen in Metals*, pp. 29–52, 1986.
- [73] J. A. Ronevich, J. G. Speer, and D. K. Matlock, "Hydrogen embrittlement of commercially produced advanced high strength sheet steels," *SAE International Journal of Materials and Manufacturing*, vol. 3, no. 1, pp. 255–267, 2010.
- [74] A. Begić Hadžipašić, J. Malina, and M. Malina, "The influence of microstructure on hydrogen diffusion and embrittlement of multiphase fine-grained steels with increased plasticity and strength," *Chemical and biochemical engineering quarterly*, vol. 25, no. 2, pp. 159–169, 2011.
- [75] A. Turnbull, E. Lembach-Beylegaard, and R. Hutchings, "Hydrogen transport in duplex stainless steels.," 1994.
- [76] N. Winzer, O. Rott, R. Thiessen, I. Thomas, K. Mraczek, T. Höche, L. Wright, and M. Mrovec, "Hydrogen diffusion and trapping in ti-modified advanced high strength steels," *Materials & Design*, vol. 92, pp. 450–461, 2016.
- [77] J. Venezuela, Q. Zhou, Q. Liu, H. Li, M. Zhang, M. S. Dargusch, and A. Atrens, "The influence of microstructure on the hydrogen embrittlement susceptibility of martensitic advanced high strength steels," *Materials Today Communications*, vol. 17, pp. 1–14, 2018.
- [78] D. Rudomilova, T. Prošek, P. Salvetr, A. Knaislová, P. Novák, R. Kodým, G. Schimo-Aichhorn, A. Muhr, H. Duchaczek, and G. Luckeneder, "The effect of microstructure on hydrogen permeability of high strength steels," *Materials and Corrosion*, vol. 71, no. 6, pp. 909–917, 2020.
- [79] I. Rodionova, M. Feoktistova, O. Baklanova, A. Amezhnov, and D. D'yakonov, "Effect of chemical composition and microstructure parameters on carbon and low-alloy steel corrosion resistance," *Metallurgist*, vol. 61, no. 9-10, pp. 770–776, 2018.
- [80] C. Izawa, S. Wagner, M. Deutges, M. Martín, S. Weber, R. Pargeter, T. Michler, H.-H. Uchida, R. Gemma, and A. Pundt, "Role of surface oxide layers in the hydrogen embrittlement of austenitic stainless steels: A tof-sims study," *Acta Materialia*, vol. 180, pp. 329–340, 2019.
- [81] Y. Zeng, J. Luo, and P. Norton, "New interpretation of the effect of hydrogen on the ion distributions and structure of passive films on microalloyed steel," *Journal of the Electrochemical Society*, vol. 151, no. 6, p. B291, 2004.

- [82] H. Luo, Z. Li, Y.-H. Chen, D. Ponge, M. Rohwerder, and D. Raabe, "Hydrogen effects on microstructural evolution and passive film characteristics of a duplex stainless steel," *Electrochemistry Communications*, vol. 79, pp. 28–32, 2017.
- [83] M. Yang, J. Luo, Q. Yang, L. Qiao, Z. Qin, and P. Norton, "Effects of hydrogen on semiconductivity of passive films and corrosion behavior of 310 stainless steel," *Journal of the Electrochemical Society*, vol. 146, no. 6, p. 2107, 1999.
- [84] S. Ningshen, U. K. Mudali, G. Amarendra, P. Gopalan, R. Dayal, and H. Khatak, "Hydrogen effects on the passive film formation and pitting susceptibility of nitrogen containing type 316l stainless steels," *Corrosion Science*, vol. 48, no. 5, pp. 1106–1121, 2006.
- [85] N. Saini, C. Pandey, and M. M. Mahapatra, "Effect of diffusible hydrogen content on embrittlement of p92 steel," *International Journal of Hydrogen Energy*, vol. 42, no. 27, pp. 17328–17338, 2017.
- [86] E. Akiyama, S. Li, T. Shinohara, Z. Zhang, and K. Tsuzaki, "Hydrogen entry into fe and high strength steels under simulated atmospheric corrosion," *Electrochimica Acta*, vol. 56, no. 4, pp. 1799–1805, 2011.
- [87] C. Dong, Z. Liu, X. Li, and Y. Cheng, "Effects of hydrogen-charging on the susceptibility of x100 pipeline steel to hydrogen-induced cracking," *International journal of hydrogen energy*, vol. 34, no. 24, pp. 9879–9884, 2009.
- [88] Q. Yang and J. Luo, "Effects of hydrogen and tensile stress on the breakdown of passive films on type 304 stainless steel," *Electrochimica Acta*, vol. 46, no. 6, pp. 851–859, 2001.
- [89] A. Trautmann, G. Mori, M. Oberndorfer, S. Bauer, C. Holzer, and C. Dittmann, "Hydrogen uptake and embrittlement of carbon steels in various environments," *Materials*, vol. 13, no. 16, p. 3604, 2020.
- [90] R. Oriani, "The physical and metallurgical aspects of hydrogen in metals," *Fusion Technology*, vol. 26, no. 4, pp. 235–266, 1994.
- [91] L. Liu, K. Tanaka, A. Hirose, and K. Kobayashi, "Effects of precipitation phases on the hydrogen embrittlement sensitivity of inconel 718," *Science and Technology of Advanced Materials*, vol. 3, no. 4, pp. 335–344, 2002.
- [92] M. Au, "High temperature electrochemical charging of hydrogen and its application in hydrogen embrittlement research," *Materials Science and Engineering: A*, vol. 454, pp. 564–569, 2007.
- [93] L. Liu, C. Zhai, C. Lu, W. Ding, A. Hirose, and K. F. Kobayashi, "Study of the effect of δ phase on hydrogen embrittlement of inconel 718 by notch tensile tests," *Corrosion science*, vol. 47, no. 2, pp. 355–367, 2005.
- [94] L. Fournier, D. Delafosse, and T. Magnin, "Cathodic hydrogen embrittlement in alloy 718," *Materials Science and Engineering: A*, vol. 269, no. 1-2, pp. 111–119, 1999.
- [95] T. Depover, T. Hajilou, D. Wan, D. Wang, A. Barnoush, and K. Verbeken, "Assessment of the potential of hydrogen plasma charging as compared to conventional electrochemical hydrogen charging on dual phase steel," *Materials Science and Engineering: A*, vol. 754, pp. 613–621, 2019.
- [96] T. Depover, E. Wallaert, and K. Verbeken, "Fractographic analysis of the role of hydrogen diffusion on the hydrogen embrittlement susceptibility of dp steel," *Materials Science and Engineering: A*, vol. 649, pp. 201–208, 2016.

- [97] P. Fassina, F. Bolzoni, G. Fumagalli, L. Lazzari, L. Vergani, and A. Sciuccati, "Influence of hydrogen and low temperature on mechanical behaviour of two pipeline steels," *Engineering Fracture Mechanics*, vol. 81, pp. 43–55, 2012.
- [98] M. Yan and Y. Weng, "Study on hydrogen absorption of pipeline steel under cathodic charging," *Corrosion Science*, vol. 48, no. 2, pp. 432–444, 2006.
- [99] T. Omura, J. Nakamura, H. Hirata, K. Jotoku, M. Ueyama, T. Osuki, and M. Terunuma, "Effect of surface hydrogen concentration on hydrogen embrittlement properties of stainless steels and ni based alloys," *ISIJ International*, pp. ISIJINT-2015, 2016.
- [100] O. Takakuwa and H. Soyama, "Suppression of hydrogen-assisted fatigue crack growth in austenitic stainless steel by cavitation peening," *International journal of hydrogen energy*, vol. 37, no. 6, pp. 5268–5276, 2012.
- [101] M. Devanathan and Z. Stachurski, "The adsorption and diffusion of electrolytic hydrogen in palladium," *Proceedings of the Royal Society of London. Series A. Mathematical and Physical Sciences*, vol. 270, no. 1340, pp. 90–102, 1962.
- [102] B. Ozdirik, K. Baert, T. Depover, J. Vereecken, K. Verbeken, H. Terryn, and I. De Graeve, "Development of an electrochemical procedure for monitoring hydrogen sorption/desorption in steel," *Journal of The Electrochemical Society*, vol. 164, no. 13, p. C747, 2017.
- [103] A. V. Uluc, "Hydrogen sorption and desorption properties of pd-alloys and steels investigated by electrochemical methods and mass spectrometry," *TU Delft, Netherlands*, 2015.
- [104] S. Modiano, J. Carreño, C. S. Fugivara, A. V. Benedetti, and O. Mattos, "Effect of hydrogen charging on the stability of sae 10b22 steel surface in alkaline solutions," *Electrochimica Acta*, vol. 51, no. 4, pp. 641–648, 2005.
- [105] C. Zheng and G. Yi, "Investigating the influence of hydrogen on stress corrosion cracking of 2205 duplex stainless steel in sulfuric acid by electrochemical impedance spectroscopy," *Corrosion Reviews*, vol. 35, no. 1, pp. 23–33, 2017.
- [106] T. Dan, T. Shoji, Z. Lu, K. Sakaguchi, J. Wang, E.-H. Han, and W. Ke, "Effects of hydrogen on the anodic behavior of alloy 690 at 60 c," *Corrosion Science*, vol. 52, no. 4, pp. 1228–1236, 2010.
- [107] S. Ningshen and U. K. Mudali, "Hydrogen effects on pitting corrosion and semiconducting properties of nitrogen-containing type 316l stainless steel," *Electrochimica acta*, vol. 54, no. 26, pp. 6374–6382, 2009.
- [108] N. Miyauchi, K. Hirata, Y. Murase, H. A. Sakaue, T. Yakabe, A. N. Itakura, T. Gotoh, and S. Takagi, "2d mapping of hydrogen permeation from a stainless steel membrane," *Scripta Materialia*, vol. 144, pp. 69–73, 2018.
- [109] S. Evers, C. Senöz, and M. Rohwerder, "Hydrogen detection in metals: a review and introduction of a kelvin probe approach," *Science and technology of advanced materials*, 2013.
- [110] G. Williams, H. McMurray, and R. Newman, "Surface oxide reduction by hydrogen permeation through iron foil detected using a scanning kelvin probe," *Electrochemistry communications*, vol. 27, pp. 144–147, 2013.
- [111] R. Schaller and J. Scully, "Measurement of effective hydrogen diffusivity using the scanning kelvin probe," *Electrochemistry communications*, vol. 40, pp. 42–44, 2014.

- [112] F. Vucko, S. Ootsuka, S. Rioual, E. Diler, A. Nazarov, and D. Thierry, "Hydrogen detection in high strength dual phase steel using scanning kelvin probe technique and xps analyses," *Corrosion Science*, vol. 197, p. 110072, 2022.
- [113] K. P. Technology, "Leaders in kelvin probe technology."
- [114] M. Stratmann and H. Streckel, "On the atmospheric corrosion of metals which are covered with thin electrolyte layers—i. verification of the experimental technique," *Corrosion Science*, vol. 30, no. 6-7, pp. 681–696, 1990.
- [115] S. Kar, "Microstructure-Corrosion Property Correlation: Elucidating the influence of microstructure on the active corrosion behavior of Pure Iron." <http://resolver.tudelft.nl/uuid:06bad22f-4b26-4284-ab02-6d2d09ce20bf>, 2020. [Online; accessed 20-July-2022].
- [116] C. Ozkan, "The Role of Phase Combinations on the Corrosion and Passivity Behaviour of High Strength Steels." <http://resolver.tudelft.nl/uuid:6901f2ac-118b-4ea2-a846-f51c563f8a87>, 2020. [Online; accessed 20-July-2022].
- [117] A. Knaislová, D. Rudomilova, P. Novák, T. Prošek, A. Michalcová, and P. Beran, "Critical assessment of techniques for the description of the phase composition of advanced high-strength steels," *Materials*, vol. 12, no. 24, p. 4033, 2019.
- [118] L. Crousén, "The effect of phase fractions and manganese content on the corrosion properties of Quenched and Partitioned Martensitic Stainless Steel." <http://resolver.tudelft.nl/uuid:4206838a-eda5-4372-80d8-1a04ed24f810>, 2021. [Online; accessed 20-July-2022].
- [119] F. Julke, J. Rodríguez Yáñez, and M. Saborío-González, "Evaluation of various steel types for the evolution of hydrogen in koh," *Tecnología en Marcha*, vol. 27, pp. 14–21, 2014.
- [120] S. T. Amaral and I. L. Müller, "Electrochemical behaviour of iron in naoh 0.01 mol/l solutions containing variable amounts of silicate," *Journal of the Brazilian Chemical Society*, vol. 10, pp. 214–221, 1999.
- [121] S. Kavunga, G. Luckeneder, E. D. Schachinger, J. Faderl, and G. Fafilek, "In situ characterization of galvanized low-alloyed steels with high-temperature cyclic voltammetry during annealing," *Electrochimica Acta*, p. 140653, 2022.
- [122] J. A. Ronevich, *Hydrogen Embrittlement in Advanced High Strength Steels*. PhD thesis, Colorado School of Mines, 2009.
- [123] A. C. Rovani, R. Breganon, G. S. de Souza, S. F. Brunatto, and G. Pintaúde, "Scratch resistance of low-temperature plasma nitrided and carburized martensitic stainless steel," *Wear*, vol. 376, pp. 70–76, 2017.
- [124] J. Rios, J. Calderón, and R. Nogueira, "Electrochemical behavior of metals used in drinking water distribution systems: a rotating cylinder electrode's study," *Corrosion*, vol. 69, no. 9, pp. 875–885, 2013.
- [125] C. Abreu, M. Cristóbal, R. Losada, X. Nóvoa, G. Pena, and M. Pérez, "High frequency impedance spectroscopy study of passive films formed on aisi 316 stainless steel in alkaline medium," *Journal of electroanalytical chemistry*, vol. 572, no. 2, pp. 335–345, 2004.
- [126] S.-Y. Lu, K.-F. Yao, Y.-B. Chen, M.-H. Wang, N. Chen, and X.-Y. Ge, "Effect of quenching and partitioning on the microstructure evolution and electrochemical properties of a martensitic stainless steel," *Corrosion Science*, vol. 103, pp. 95–104, 2016.

- [127] K. Encalada Flores, "Study of Hydrogen Sorption/Desorption Effect on Austenitic Iron-Based Alloys: Surface Interaction Studied by Cyclic Voltammetry on 304L Stainless Steel and Invar." <http://resolver.tudelft.nl/uuid:32242c29-753c-412f-ae6a-d08c673f9920>, 2019. [Online; accessed 20-July-2022].
- [128] E. Galindo-Nava, B. Basha, and P. Rivera-Díaz-del Castillo, "Hydrogen transport in metals: Integration of permeation, thermal desorption and degassing," *Journal of Materials Science & Technology*, vol. 33, no. 12, pp. 1433–1447, 2017.
- [129] G. Hinds, J. Zhao, A. Turnbull, *et al.*, "Hydrogen diffusion in super 13% chromium martensitic stainless steel," *Corrosion*, vol. 61, no. 04, 2005.
- [130] T. Schaffner, A. Hartmaier, V. Kokotin, and M. Pohl, "Analysis of hydrogen diffusion and trapping in ultra-high strength steel grades," *Journal of Alloys and Compounds*, vol. 746, pp. 557–566, 2018.
- [131] H. Kuo and J. Wu, "Passivation treatment for inhibition of hydrogen absorption in chromium-plated steel," *Journal of materials science*, vol. 31, no. 22, pp. 6095–6098, 1996.
- [132] Y. Park, I. Maroef, A. Landau, and D. Olson, "Retained austenite as a hydrogen trap in steel welds," *Welding Journal-New York-*, vol. 81, no. 2, pp. 27–S, 2002.
- [133] D. P. Escobar, K. Verbeken, L. Duprez, and M. Verhaege, "Evaluation of hydrogen trapping in high strength steels by thermal desorption spectroscopy," *Materials Science and Engineering: A*, vol. 551, pp. 50–58, 2012.
- [134] S. S., "Combined Ab-initio and Experimental Study of Hydrogen Sorption in Dual-Phase Steels." <http://resolver.tudelft.nl/uuid:20e81133-c326-4fc1-920e-74d313bd8ce5>, 2019. [Online; accessed 20-July-2022].
- [135] M. Nieuwoudt, J. Comins, and I. Cukrowski, "The growth of the passive film on iron in 0.05 m naoh studied in situ by raman micro-spectroscopy and electrochemical polarisation. part i: near-resonance enhancement of the raman spectra of iron oxide and oxyhydroxide compounds," *Journal of Raman Spectroscopy*, vol. 42, no. 6, pp. 1335–1339, 2011.
- [136] P. Bruzzoni and E. Riecke, "On the mechanism of hydrogen transport through the passive oxide film on iron," *Corrosion science*, vol. 36, no. 9, pp. 1597–1614, 1994.
- [137] W. Swansiger and R. Bastasz, "Tritium and deuterium permeation in stainless steels: influence of thin oxide films," *Journal of Nuclear Materials*, vol. 85, pp. 335–339, 1979.
- [138] S. Yen, "A retarding mechanism of thermally grown oxide films on hydrogen embrittlement of aisi 430 stainless steel," *Materials chemistry and physics*, vol. 59, no. 3, pp. 210–219, 1999.
- [139] S. Joiret, M. Keddou, X. Nóvoa, M. Pérez, C. Rangel, and H. Takenouti, "Use of eis, ring-disk electrode, eqcm and raman spectroscopy to study the film of oxides formed on iron in 1 m naoh," *Cement and Concrete Composites*, vol. 24, no. 1, pp. 7–15, 2002.
- [140] P. Schmuki, M. Büchler, S. Virtanen, H. Böhni, R. Müller, and L. Gauckler, "Bulk metal oxides as a model for the electronic properties of passive films," *Journal of the electrochemical society*, vol. 142, no. 10, p. 3336, 1995.

- [141] S. Virtanen, P. Schmuki, A. J. Davenport, and C. M. Vitus, "Dissolution of thin iron oxide films used as models for iron passive films studied by in situ x-ray absorption near-edge spectroscopy," *Journal of the Electrochemical Society*, vol. 144, no. 1, p. 198, 1997.
- [142] L. Guo, S. Qin, B. Yang, D. Liang, and L. Qiao, "Effect of hydrogen on semiconductive properties of passive film on ferrite and austenite phases in a duplex stainless steel," *Scientific reports*, vol. 7, no. 1, pp. 1–6, 2017.
- [143] S. Thomas, G. Sundararajan, P. White, and N. Birbilis, "The effect of absorbed hydrogen on the corrosion of steels: review, discussion, and implications," *Corrosion*, vol. 73, no. 4, pp. 426–436, 2017.

A

APPENDIX

The table A.1 shows the peak values relating to the CV's of DP1000 - Pre-Conditioning A. The general peak positions of all the peaks are indicated.

Table A.1: Peak potentials of the CV voltammograms for DP1000 - Pre-Conditioning A, the peaks a3 and c2 are not included in the table as it is beyond the scope of this study. E_o' is the formal standard potential and it equals half of the total sum of potentials of a redox couple.

Material	Electrolyte	CV Stage	E_{a1}' (V vs SSC _{sat})	E_{a1} (V vs SSC _{sat})	E_{a2} (V vs SSC _{sat})	E_{c1} (V vs SSC _{sat})	E_o' (V vs SSC _{sat})
DP1000	1 M NaOH + 8 g/L Thiourea	Before H Charging	No Peak	-0.871 ± 0.001	-0.704 ± 0.002	-1.057 ± 0.001	-0.881 ± 0.001
		After H Charging	-0.907 ± 0.001	-0.844 ± 0.002	-0.706 ± 0.000	-1.061 ± 0.000	-0.884 ± 0.001
		After H Discharging	No Peak	No Peak	-0.699 ± 0.001	-1.065 ± 0.002	-0.882 ± 0.001

The table A.2 shows the peak values relating to the CV's of the Pure Iron - Pre-Conditioning A. The general peak positions of all the peaks are indicated.

Table A.2: Peak potentials of the CV voltammograms for Pure Iron - Pre-Conditioning A. E_o' is the formal standard potential and it equals half of the total sum of potentials of a redox couple.

Material	Electrolyte	CV Stage	E_{a1}' (V vs SSC _{sat})	E_{a1} (V vs SSC _{sat})	E_{a2} (V vs SSC _{sat})	E_{c1} (V vs SSC _{sat})	E_o' (V vs SSC _{sat})
Pure Iron	1 M NaOH + 8 g/L Thiourea	Before H Charging	No Peak	-0.870 ± 0.003	-0.705 ± 0.001	-1.047 ± 0.001	-0.876 ± 0.001
		After H Charging	-0.894 ± 0.001	-0.857 ± 0.001	-0.699 ± 0.000	-1.057 ± 0.000	-0.878 ± 0.000
		After H Discharging	No Peak	No Peak	-0.692 ± 0.001	-1.062 ± 0.002	-0.877 ± 0.001

The table A.3 shows the peak values relating to the CV's of the AISI 420 - Pre-conditioning A. The general peak positions of all the peaks are indicated.

Table A.3: Peak potentials of the CV voltammograms for AISI 420. E_o' is the formal standard potential and it equals half of the total sum of potentials of a redox couple.

Material	Electrolyte	CV Stage	E_{a1}' (V vs SSC _{sat})	E_{a2} (V vs SSC _{sat})	E_{c1} (V vs SSC _{sat})	E_{c2} (V vs SSC _{sat})	E_o' (V vs SSC _{sat})
AISI 420	1 M NaOH + 8 g/L Thiourea	Before H Charging	No Peak	-0.716 ± 0.001	-1.004 ± 0.001	No Peak	-0.860 ± 0.001
		After H Charging	-0.870 ± 0.002	-0.737 ± 0.001	-0.993 ± 0.008	-0.838 ± 0.004	-0.865 ± 0.005
		After H Discharging	No Peak	-0.728 ± 0.003	-1.008 ± 0.007	0.845 ± 0.003	-0.868 ± 0.005

The table A.4 shows the peak values relating to the CV's of the DP1000 - Pre-conditioning B. The general peak positions of all the peaks are indicated. The values of peak potentials are more or less similar for both active and passive behaviour.

Table A.4: Peak potentials of the CV voltammograms for DP1000 - Pre-conditioning B. E_0' is the formal standard potential and it equals half of the total sum of potentials of a redox couple.

Material	Electrolyte	CV Stage	E_{a1}' (V vs SSC _{s,at})	E_{a1} (V vs SSC _{s,at})	E_{a2} (V vs SSC _{s,at})	E_{c1} (V vs SSC _{s,at})	E_0' (V vs SSC _{s,at})
DP1000	1 M NaOH + 8 g/L Thiourea	Before H Charging	No Peak	-0.857± 0.008	-0.690± 0.009	-1.033± 0.007	-0.861± 0.008
		After H Charging	-0.897± 0.004	-0.839± 0.007	-0.686± 0.009	-1.043± 0.007	-0.865± 0.008
		After H Discharging	No Peak	No Peak	-0.684± 0.007	-1.045± 0.002	-0.865± 0.008

The table A.4 shows the peak values relating to the CV's of the Pure Iron - Pre-conditioning B. The general peak positions of all the peaks are indicated. The values of peak potentials are more or less similar for both active and passive behaviour.

Table A.5: Peak potentials of the CV voltammograms for Pure Iron - Pre-conditioning B. E_0' is the formal standard potential and it equals half of the total sum of potentials of a redox couple.

Material	Electrolyte	CV Stage	E_{a1}' (V vs SSC _{s,at})	E_{a1} (V vs SSC _{s,at})	E_{a2} (V vs SSC _{s,at})	E_{c1} (V vs SSC _{s,at})	E_0' (V vs SSC _{s,at})
Pure Iron	1 M NaOH + 8 g/L Thiourea	Before H Charging	No Peak	-0.869± 0.001	-0.702± 0.004	-1.052± 0.001	-0.877± 0.002
		After H Charging	-0.897± 0.001	-0.847± 0.004	-0.697± 0.003	-1.058± 0.001	-0.878± 0.002
		After H Discharging	No Peak	No Peak	-0.694± 0.003	-1.061± 0.001	-0.877± 0.002

The table A.4 shows the peak values relating to the CV's of the AISI420 - Pre-conditioning B. The general peak positions of all the peaks are indicated. The values of peak potentials are more or less similar for both active and passive behaviour.

Table A.6: Peak potentials of the CV voltammograms for AISI 420 - Pre-conditioning B. E_0' is the formal standard potential and it equals half of the total sum of potentials of a redox couple.

Material	Electrolyte	CV Stage	E_{a1}' (V vs SSC _{s,at})	E_{a1} (V vs SSC _{s,at})	E_{c1} (V vs SSC _{s,at})	E_{c2} (V vs SSC _{s,at})	E_0' (V vs SSC _{s,at})
AISI 420	1 M NaOH + 8 g/L Thiourea	Before H Charging	No Peak	-0.730± 0.001	-0.987± 0.011	No Peak	-0.858± 0.006
		After H Charging	-0.853± 0.003	-0.743± 0.003	-0.989± 0.002	-0.865± 0.002	-0.866± 0.002
		After H Discharging	No Peak	-0.751± 0.004	-0.984± 0.003	-0.850± 0.002	-0.868± 0.003

